1964

Model study of a buried arch subjected to dynamic loading

Robert Kinley Tener
Iowa State University

MODEL STUDY OF A BURIED ARCH SUBJECTED TO DYNAMIC LOADING

by

Robert Kinley Tener

A Dissertation Submitted to the

Graduate Faculty in Partial Fulfillment of

The Requirements for the Degree of

DOCTOR OF PHILOSOPHY

Major Subject: Structural Engineering

Approved:

Signature was redacted for privacy.

In Charge of Major Work

Signature was redacted for privacy.

Head of Major Department

Signature was redacted for privacy.

Dean of Graduate College

Iowa State University
Of Science and Technology
Ames, Iowa

1964

TABLE OF CONTENTS

ACKNOWLEDGMENTS

The cooperation and assistance of a number of personnel of the U. S. Army Engineer Waterways Experiment Station, without whose contributions the work reported herein would not have been possible, is acknowledged. Particular appreciation is expressed to the following persons: Mr. W. J. Flathau, Chief, Structural Dynamics Section, for his cooperation in the technical and administrative planning of the laboratory tests; members of the Shops Branch, especially Mr. J. J. Loviza, Machine Shop Foreman, for their work in procuring and fabricating the test structures and appurtenances; members of the Dynamics Section, Instrumentation Branch, especially Mr. K. Daymond, for their cooperative support in instrumentation and data recording for the laboratory tests; personnel of the Soil Dynamics Branch for providing the soil test data; the staff of the Reproduction and Reports Branch for their assistance in the preparation of the manuscript; and the many engineers and technicians of the Nuclear Weapons Effects Division whose cooperation and support were essential to the experimental program.

Acknowledgment is made to Capt. J. W. McNulty and 1st Lt. A. J. Hendron, Jr., for their comments and encouragement, and to Col. Alex G. Sutton, Jr., Director, U. S. Army Engineer Waterways Experiment Station, for his interest and for having made the Station facilities available. The advice and encouragement of Dr. C. E. Ekberg, Jr., Professor and Head of the Department of Civil Engineering, Iowa State University, is appreciated.

Above all, the author is indebted to the Office of the Chief of Engineers, U. S. Army, for furnishing the opportunity for this research by providing the author's assignment to the Waterways Experiment Station.

I. INTRODUCTION

A. Background

One of the most challenging problems facing the structural engineer today is the demand for a rational approach to the design of underground structures subject to nuclear blast loading. The necessity for a reliable design procedure for such protective structures need hardly be emphasized. Current research in this field is being conducted along a broad front, and investigators are treating the problem by a wide variety of approaches. Of great importance to the realization of a reliable design procedure is a knowledge of the behavior of a given buried structure when the ground surface is subjected to a dynamic overpressure.

One of the most promising and expedient methods for predicting this behavior is by the use of models. Previous papers have pointed out many advantages of the modeling approach in comparison with other experimental and analytical methods (18, 23, 27).* It has been concluded by several investigators that the use of small models to simulate dynamically loaded underground structures is feasible (2, 18, 19).

B. Purpose and Scope of Investigation

The objective of this thesis is to investigate a modeling procedure for predicting the elastic behavior of a laboratory-size prototype buried arch structure subjected to a dynamic surface overpressure.

The requirement for this objective is based upon the assumption that

*Numbers in parentheses refer to similarly numbered references in the literature cited.

an ultimate goal of protective construction research is the capability of predicting, by means of a model, the behavior of a prototype buried structure in a field installation. To date, this goal has not been realized. In order to formulate a reliable modeling procedure for predicting field prototype behavior, it is necessary to first develop a capability for predicting the response of a laboratory-size prototype. If it should prove prohibitively difficult to model the behavior of the laboratory prototype, then the extension of this procedure to modeling field prototype behavior may well be impossible, or at best, impractical. However, if the behavior of a laboratory prototype can be successfully predicted, the results of such a study would provide information of great value to the ultimate goal of modeling field prototype response.

This investigation is limited to consideration of the laboratory modeling problem, without direct reference to its application to field prototype conditions. In order that the test structures could be reused under repeated loadings, structural response was confined to the elastic range.

C. Summary of Investigation

The investigation was carried out in the Nuclear Weapons Effects Division of the U. S. Army Engineer Waterways Experiment Station (WES) at Vicksburg, Mississippi.

Following development of design conditions and prediction equations utilizing similitude theory, a pilot model arch was designed, analyzed and constructed. Pilot tests on this structure were conducted prior to arriving at a final arch model design. Five geometrically similar

aluminum arches with diameters of 8 to 24 inches were fabricated and instrumented to record selected deflections and strains. These structures were installed in dense dry sand in the Large Blast Load Generator test facility (LBLG) at WES and subjected to approximately plane wave loading from dynamic surface overpressures in the 30- to 200-psi range. Peak dynamic deflections and strains were obtained, and the reliability of the modeling procedure was determined by the ability to predict peak dynamic deflections and strains from one model to another.

Symbols used in the text are grouped for reference in Appendix A: Notation.

II. SUMMARY OF PREVIOUS WORK

The application of similitude in protective construction research has been reported by numerous investigators. One of the earliest such applications was in the Underground Explosion Test Program reported in 1952 by Engineering Research Associates, Inc. (8). For that study, scaling laws based upon dimensional analysis were formulated for stresses, displacements, velocities and accelerations in soil and rock due to the detonation of a buried charge. The effects of charge depth, charge weight, range and soil type were studied. It was concluded that the test results generally tended to support the model law, but the applicability of the results was limited strictly to the soil and rock conditions found in those tests.

A more detailed theoretical investigation of scaling blast effects on surface structures was performed by Jones in 1958 (12). His study concluded that the requirements of dynamic similarity led to difficulties in satisfying all the design conditions for surface structures, but did not consider buried structures.

Recent studies at MIT have included modeling dynamic structural response (4, 11, 20, 21), but this work has been limited to surface structures and structural elements. Valuable information was developed regarding model materials and fabrication techniques, predicting behavior of joints, and modeling dynamic plastic response. Successful modeling of dynamic failure of surface domes (21) and behavior to failure of shear walls, columns and frames (4) were reported.

A theoretical model analysis for buried structures was reported by Armour Research Foundation (now the Illinois Institute of Technology

Research Institute)(1). The modeling treatment recognized the difficulty of scaling all the parameters in the dynamic soil-structure interaction problem, and concluded that an exact model could not practically be built. This reference constitutes an excellent state-of-the-art analysis of the overall field of underground structure experimentation.

An analytical investigation of the use of models was presented by Mechanics Research Division, General American Transport Corporation (3), but their approach does not readily lend itself to the design and performance of model tests. A more directly applicable approach than the one developed is desirable.

The most significant investigation to date on the subject has been reported by Murphy and Young of Iowa State University in a study for the Air Force Weapons Laboratory (18, 19). A similitude treatment of the dynamically loaded buried structure problem was presented (18), and a series of tests was conducted which generally verified the model theory developed (19). The test structures were aluminum cylinders with diameters of 1, 2, 4 and 8 inches, and 1-inch and 2-inch square tubes, buried in dry Ottawa sand. The cylinders were relatively stiff, with a diameter-to-thickness ratio of 15.9. The program utilized three different dynamic loading devices, producing peak overpressures of up to 460 psi. The results of the tests clearly demonstrated, within the range of parameters investigated, the feasibility of predicting the behavior of buried structures by means of models. Three general areas for further consideration were proposed: (1) investigation of increased length scales, on the order of 10 or greater, (2) further study of strain-rate effects on cohesive soil behavior, and (3) the need for a more specific determination of soil

properties, especially in regard to the prospect of utilizing different soil types in model and prototype.

The present study is intended to extend the range of parameters investigated beyond those of the work by Murphy and Young. There are three primary areas of divergence: (1) structural size, configuration and flexibility, (2) input loading characteristics, including level of peak overpressure and overpressure-time history, and (3) entirely different laboratory facilities. The significance of the last point should not be overlooked, and was emphasized by Murphy and Young (19). In addition, although the soil type employed herein is basically a dry sand, the fact that its physical characteristics differ from those of Ottawa sand is noteworthy.

A model analysis of a buried arch was reported recently by the U. S. Naval Civil Engineering Laboratory (2). A comparison was made between four residual deflections of a prototype structure in one full-scale nuclear field test and comparable deflections observed in one laboratory test on a small flexible arch. Although the four scaled-up deflections from the laboratory test structure were of the same order of magnitude as those observed in the field test, very limited scaling relations between the systems were established and a number of highly questionable assumptions were required. No firm conclusions regarding the validity of the modeling procedure were offered.

Valuable information has been gathered from two projects in field tests on model structures, and is presented in classified reports (10, 22). Useful lists of references on modeling dynamic structural response are available (1, 11, 20, 23).

In summary, it appears that work to date has resulted in a recognition of the advantages of model studies in this field. A valuable amount of similitude theory has been developed, and certain scaling difficulties have been recognized. However, there is a distinct need for extensive experimental study to verify the proposed model theories, clarify the extent of difficulties anticipated, and eventually establish a procedure for predicting with confidence field prototype response.

III. SIMILITUDE TREATMENT OF THE PROBLEM

A. Introduction

The application of model theory to the dynamically loaded buried structure problem is particularly appropriate. This is a case in which the great degree of complexity of the phenomena involved and the lack of a ready analytical procedure indicate that a model study may produce desirable information at a considerable saving of time and effort.

Model theory based upon dimensional analysis follows from the Buckingham Pi theorem (5), which states as follows: If a functional relationship exists between n variables which involve b basic dimensions,

$$f(x_1 , x_2 , x_3 , \ldots x_n) = 0 ,$$

then this relationship can be expressed in terms of s dimensionless, independent quantities called Pi terms:

$$F(\pi_1 , \pi_2 , \pi_3 , \ldots \pi_s) = 0 ,$$

where

$$s = n - b .$$

Two assumptions are inherent in this theorem: (1) that the function f above exists, and (2) that it is unique.

The method used herein to formulate the model design follows the procedure described by Murphy (17). The procedure involves (a) identification of those variables pertinent to the phenomenon being studied, (b) formulation of a set of dimensionless quantities (Pi terms) composed of the pertinent variables, and (c) determining the design conditions and prediction equations.

B. Identification of Pertinent Variables

1. General

The most important, and in general the most difficult, step in assuring a valid model design is the determination of every variable which is significant to the behavior of the system. For the present problem, the variables are associated with the structure, the soil medium and the loading.

2. Structure

The dependent variables selected for this study are the peak dynamic deflection of the structure at a point and the peak dynamic strain in the structure at a point. The independent variables associated with the structure include those which define its geometry, and the engineering properties of the structural material. These properties are taken as the elastic modulus and the mass density of the structural material. Yield strength need not be considered since consideration is limited to elastic behavior. The natural period of vibration of a given structure in a particular mode in air is uniquely defined by its geometry and the density and elastic modulus of the material (Appendix D), and is therefore not an independent variable.

3. Soil

To determine the variables associated with the soil medium which are significant to the soil-structure interaction problem is one of the most difficult steps in the model design. Soil properties may be categorized

as index properties and engineering properties. Index properties are those characteristics which describe the physical distinctions between different soils, such as particle shape, grain size distribution, uniformity coefficient, void ratio, water content, the Atterberg limits and others. Engineering properties are those hydraulic and mechanical properties which influence the manner in which the soil will behave in a physical system, and include permeability, compressibility, shearing resistance and stress-deformation relationships under various states of stress. Index properties are important only as they influence the nature of the engineering properties, and as long as the important engineering properties can be defined in a given case, there is no need for index properties to be considered significant to the behavior of the physical system. An analogy can be found in concrete. Water-cement ratio and aggregate gradation are important only as they influence the compressive strength and other engineering properties, and as long as these engineering properties can be defined for a given concrete, the water-cement ratio and aggregate gradation are not significant.

It is necessary then to isolate those engineering properties of the soil medium which are pertinent in dynamic wave propagation and soil-structure interaction. Figure 1 is a representative schematic of the soil-structure interaction situation with a dynamic plane wave surface loading. The shock wave is propagated down through the soil medium toward the structure. For some distance h it is assumed that the soil is in dynamic one-dimensional compression, uninfluenced by the structure or other boundary conditions. It is required to determine the variables associated with the soil medium which influence the behavior of the

system in Region I. Experience relates that the mass density of the soil and the form of the stress-strain curve in one-dimensional compression influence the propagation of the shock wave, and thus these must be included as pertinent variables.

In Region II, the behavior of the system is no longer one-dimensional. Here the deformations of the structure will impose complex confining and boundary conditions on the soil in its vicinity. It is required to identify the definable engineering properties associated with the soil medium which will influence the behavior of the system under these conditions. The shearing forces mobilized in the soil will be relatively large compared with the volumetric forces, and the engineering properties governing the behavior of soil subjected to this condition are the angle of internal friction and cohesion of the soil, as determined under loading rates relevant to the problem. The stress-strain curve for the soil which is of importance in this region is one which represents the influence of lateral confinement and deformation. Conducting triaxial-compression tests at various confining pressures is the common procedure, and the parameters defining the family of stress-strain curves from triaxial tests may be taken as pertinent variables.

In addition to the engineering properties of the soil, an important parameter is the level of stress in the medium. Due to the nonlinear stress-strain relations in soils, the soil stiffness is dependent upon its state of stress, which is related to the surface overpressure. The pertinent variables associated with the soil medium, in summary, are its mass density, its shearing resistance, the stress-strain relations in one-dimensional compression and from triaxial tests and the level of surface

overpressure. In general, the engineering properties listed are dependent upon time rate of loading, so it must be assured in the model design that the dependence of these properties on loading times is accounted for. Fortunately, it has been observed that the dependence of soil strength upon rates of loading within the dynamic range is probably very slight for dry dense sands (29) and a clay classified as CH in the Unified Soil Classification System (6). Since these soil types represent the extremes in characteristics of real soils, it may be conjectured that variation of strength properties with rate of loading, within times termed dynamic, may be relatively insignificant for all soils.*

4. Loading

The response of a buried structure is related to the forces which act on it and around its boundary. These forces have their origin in the dead load of the structure and soil, and in the live load due to the overpressure on the surface of the soil. If dead load forces are to be considered, a pertinent variable in addition to structure density and geometry is the acceleration due to gravity.

The applied live load forces acting directly upon the buried structure cannot be directly evaluated in a prototype nor caused in a model with any degree of completeness or accuracy. However, these forces are dependent upon the surface overpressure. Therefore, the live load is represented by the time-dependent overpressure on the surface of the soil medium, and the pertinent variables are overpressure and time.

*Hendron, A. J., Vicksburg, Miss. Private communication. 1964.

The variables selected are summarized in Table 1 and depicted in Figure 2.

C. Development of Design Conditions

The general relationships among the variables may be expressed as

$$\epsilon = f_1 (D , H , \lambda , E , \rho , \rho_s , c , \phi , M_s , E_s , p_o , g , t) \quad (1)$$

and

$$\Delta = f_2 (D , H , \lambda , E , \rho , \rho_s , c , \phi , M_s , E_s , p_o , g , t) \quad (2)$$

Fourteen variables appear in each relationship, involving three basic dimensions F , L and T . According to the Buckingham Pi theorem, the number of dimensionless, independent Pi terms required to express a relationship among the variables involved is equal to the number of variables minus the number of basic dimensions in which the variables are measured. Thus 11 Pi terms are required. One possible set of Pi terms yields the following relationships:

$$\epsilon = F_1 \left(\frac{H}{D} , \frac{\lambda}{D} , \frac{p_o}{E} , \frac{c}{E} , \phi , \frac{M_s}{E} , \frac{E_s}{E} , \frac{\rho_s}{\rho} , \frac{gt^2}{D} , \frac{D}{t}\sqrt{\frac{\rho}{E}} \right) \quad (3)$$

and

$$\frac{\Delta}{D} = F_2 \left(\frac{H}{D} , \frac{\lambda}{D} , \frac{p_o}{E} , \frac{c}{E} , \phi , \frac{M_s}{E} , \frac{E_s}{E} , \frac{\rho_s}{\rho} , \frac{gt^2}{D} , \frac{D}{t}\sqrt{\frac{\rho}{E}} \right) \quad (4)$$

Equations 3 and 4 are equally valid for both the prototype and model systems. In order to faithfully reproduce the prototype system by a model, each Pi term for the prototype must be set equal to that Pi term in the model. Doing so results in the following design conditions (DC) which must be satisfied in order to obtain an adequate model. The subscript m denotes the model system; terms without subscripts represent the prototype system. The length scale n is defined by $n \equiv \frac{D}{D_m}$.

1.	$(H/D)_m = H/D$	$H_m = H/n$
2.	$(\lambda/D)_m = \lambda/D$	$\lambda_m = \lambda/n$
3.	$(p_o/E)_m = p_o/E$	$(p_o)_m = (E_m/E)\, p_o$
4.	$(c/E)_m = c/E$	$(c)_m = (E_m/E)\, c$
5.	$\phi_m = \phi$	
6.	$(M_s/E)_m = M_s/E$	$(M_s)_m = (E_m/E)\, M_s$
7.	$(E_s/E)_m = E_s/E$	$(E_s)_m = (E_m/E)\, E_s$
8.	$(\rho_s/\rho)_m = \rho_s/\rho$	$(\rho_s)_m = (\rho_m/\rho)\, \rho_s$
9.	$(gt^2/D)_m = gt^2/D$	$(t)_m = \sqrt{\frac{g}{g_m} \cdot \frac{1}{n}}\, t$
10.	$\left(\frac{D}{t}\sqrt{\frac{\rho}{E}} \right)_m = \frac{D}{t}\sqrt{\frac{\rho}{E}}$	$(t)_m = \left[\frac{1}{n}\sqrt{\frac{\rho_m}{\rho} \cdot \frac{E}{E_m}} \right] t$

Design conditions (DC) 1 and 2 require geometric similarity between model and prototype in all significant respects.

DC 3 specifies the surface overpressure scale for given elastic moduli in prototype and model. In this investigation the same structural material (aluminum) was selected for prototype and model. Therefore, $E_m = E$ and $\rho_m = \rho$. DC 3 then becomes $(p_o)_m = p_o$, which requires that the surface overpressure in the model system equal that in the prototype at corresponding points and times.

Noting that $E_m = E$ and $\rho_m = \rho$, DC 4 through 8 require that the cohesion, angle of internal friction, stress-strain curves in one-dimensional compression and triaxial compression, and mass density of the soil be the same in model and prototype. These design conditions can be satisfied by using the same soil type in model and prototype.

DC 9 relates the time scale to the gravitational field scale. In this

study it was impractical to scale gravity, so that $g_m = g$ and DC 6 becomes $(t)_m = t/\sqrt{n}$.

DC 10 establishes the time scale as determined by the structural material properties. Since $\rho_m = \rho$ and $E_m = E$, this design condition becomes $t_m = t/n$. It is noted that a conflict exists between the time scales required by DC 9 and DC 10, which is discussed below.

D. Analysis of Design Conditions

Satisfying DC 1 and 2 was done by scaling structural dimensions and installation geometry as closely as possible. Appendix B indicates structural dimensions, which were accurately scaled, and describes the actual installation.

To satisfy DC 3, which required equal magnitude of surface overpressure in model and prototype, all five structures were placed in the LBLG in one installation and subjected to the same blast loading. Although it was known that the LBLG blast loading was not a perfectly plane wave, it was felt that locations in the medium which experienced the same peak overpressure could be selected for the five structures, as discussed in Appendix B.

To satisfy DC 4 through 8, the same soil was used in model and prototype. For the present investigation, a dry, uniform, medium sand was selected. The use of dense dry sand in this project was primarily dictated by convenience in the laboratory. The use of other soil types was not feasible at the time of this study, since the LBLG test facility at WES was adapted for use only with sand at that time. In a given dry sand, the shearing resistance and the stress-strain relations in one-dimensional

compression and in a triaxial test are dependent only on the density of the sand. Therefore, if the in-place density of the sand is the same in model and prototype, and if p_o is equal in the two systems, then DC 4 through 8 will be satisfied. Equal soil densities in model and prototype systems were achieved by striving for uniform density throughout the LBLG installation as discussed in Appendix B.

The remaining design conditions 9 and 10 deal with the time scale. DC 9 is based upon gravitational scaling, or scaling body forces. If dead loads may be neglected, DC 9 need not be satisfied. It seems reasonable to assume that dynamic structural response to surface overpressures in the 30- to 300-psi range would not noticeably be affected by dead loads. This assumption is supported by other tests (19) and design theory (9). DC 9 will be neglected in this experiment.

The design condition on time then requires that the time scale equal the length scale, based upon DC 10. However, it was decided to place all five scaled structures in a single LBLG installation and subject them to the same blast loading. There were several reasons for this.

1. For the sake of economy, all five structures could be tested with one LBLG installation.

2. It was felt that there was a better chance of subjecting each structure to the same magnitude of overpressure by this means than by making five separate installations and conducting five separate dynamic shots designed for the same peak overpressure.

3. It was felt that a fairly uniform soil density throughout the medium could be obtained in a single installation and that this uniformity would improve after several repeated shots on the same specimen. This was contrasted with the problem of duplicating the soil density between several specimens installed and tested separately.

4. Even though scaling the time characteristics of the overpressure is desirable, at present there is no capability for widely varying or accurately controlling the rise and decay times of the LBLG overpressure. Therefore, even separate shots on separate installations would not enable proper time scaling under existing capabilities.

By subjecting all five scaled structures to the same overpressure-time history, the time scale is unity and DC 10 must be considered to be distorted. It is possible to analyze to what degree this distortion may influence the structural response. For purposes of this analysis, the physical meaning of the Pi term $\frac{D}{t}\sqrt{\frac{\rho}{E}}$ must be interpreted. It is necessary to assume a typical prototype loading function, and the function shown at the bottom of Figure 2 is assumed. The distortion of the time scale exists because t_r and t_e will be equal in model and prototype.

The factor $D\sqrt{\frac{\rho}{E}}$ in DC 10 is proportional to the natural period of vibration of the structure τ, as shown in Appendix D. The Pi term $\frac{D}{t}\sqrt{\frac{\rho}{E}}$ may then be replaced by τ/t, or with equal validity by its reciprocal t/τ. In order to attach physical significance to this

term, the variable t may be represented, first by the effective duration of the overpressure t_e (Figure 2), and then, by the rise time t_r .

Consider first the dynamic effect associated with t_e/τ . Treating the dynamically loaded buried structure as an undamped, single-degree-of-freedom system subjected to an initially peaked triangular pulse, it has been theoretically shown (15) that for values of t_e/τ greater than about 5, the structural response is virtually independent of the value of t_e/τ . The assumption of an undamped, single-degree-of-freedom system is a highly simplified approximation of the actual system studied herein, but the assumption is considered reasonable for purposes of the present analysis. For the structures used in this study, the natural period of the buried pilot model arch (8-inch diameter) was observed to be 1.8 milliseconds (msec). The predicted value of τ for the largest (24-inch diameter) arch is then 5.4 msec (Appendix D). The effective duration in the LBLG under existing capabilities is on the order of several hundred msec. Thus t_e/τ should exceed 40 or so for all the scaled structures, and any dynamic effects attributable to t_e/τ may reasonably be neglected. It was expected that distortion of scaling duration time would have negligible effect on the prediction equations.

Regarding t_r/τ , it has likewise been stated theoretically (15) that the influence of rise time on the response of a single-degree-of-freedom elastic structure subjected to a long-duration force pulse may be represented by an amplification factor A, where

$$A \equiv \frac{\Delta_{max}}{\Delta_{static}} = 1 + \frac{\tau}{\pi t_r} \sin \frac{\pi t_r}{\tau} \qquad (5)$$

Based on previous tests, rise time for the LBLG surface overpressure was observed to be on the order of 3 msec. Assuming that this rise time is not altered as the stress wave propagates down through the medium, this is the value for t_r which would be used in Equation 5. Using the predicted values of τ for the five scaled structures of 1.8, 2.7, 3.6, 4.5 and 5.4 msec, Equation 5 yields amplification factors of 0.83, 0.90, 1.19, 1.41 and 1.56, respectively. These factors represent the ratio of the peak dynamic response of the undamped, single-degree-of-freedom system to the response of the system if the peak overpressure is applied statically. The magnitudes of the amplification factors indicate that distortion of DC 10 for rise time may noticeably influence the prediction equation, based on the stated assumption that rise time at the level of the structure is the same as that of the surface. Therefore, DC 10 is restated as

$$\left(\frac{t_r}{\tau}\right)_m = \alpha \frac{t_r}{\tau}$$

or

$$(t_r)_m = \alpha \left(\frac{\tau_m}{\tau}\right) t_r = \frac{\alpha}{n} t_r \qquad (6)$$

where α is the distortion factor. Since $(t_r)_m = t_r$ for this study, Equation 6 yields

$$\alpha = n \ , \qquad (7)$$

or the distortion factor equals the length scale.

However, for the particular medium selected for this investigation, a dense, dry, uniform sand, recent tests have shown that the rise time of the incident overpressure is in fact altered as the shock propagates down through the sand. During a series of free-field firings in the LBLG, a phenomenon known as "shocking-up" occurred. This term applies to the condition in which the rise time of the shock wave decreases with depth as the shock wave travels downward, as indicated schematically in Figure 3. For this medium there is a depth at which the rise time decreases to a very small value ($\ll$ 1 msec) compared to the surface rise time t_r , and the peak overpressure arrives practically instantaneously at a point. This phenomenon is readily explainable by energy considerations for a material with an upward-turning stress-strain curve in one-dimensional compression such as dense, dry sand, as shown by Kennedy and Hendron (13). In the LBLG, the depth of dense, dry sand at which the rise time becomes approximately zero is on the order of 6 inches.

Thus, for the conditions in this study, in which the shallowest structure was buried 8 inches, it was anticipated that the actual rise times for the shock wave impinging on the structures would be near zero compared with τ . In this case, the effect of distortion of DC 10 was expected to be negligible.

It is noted that the investigation reported by Murphy, Young, and Martin (19) utilized a similar design condition on time; that is, the time scale in that study was required to equal the length scale. However, it was not possible to vary the time characteristics of the overpressure in the shock tube device which was used. Distortion of the design

condition on time apparently did not greatly influence the prediction of peak strains between the 1-, 2- and 4-inch cylinders used. However, the report did not present data regarding the influence of t_r/τ due to the very short rise times generated in the shock tube.

E. Prediction Equations

Based upon Equations 3 and 4, the prediction equations for strain and deflection for a true model are

$$\epsilon = \epsilon_m \tag{8}$$

and

$$\frac{\Delta}{D} = \left(\frac{\Delta}{D}\right)_m ,$$

or

$$\Delta = n\Delta_m \tag{9}$$

However, it was found in the previous section that distortion of DC 8 could possibly affect the prediction of the dependent variables. Therefore, if a distorted model is assumed, Equations 6 and 7 must be modified according to

$$\epsilon = \delta_1 \epsilon_m \tag{10}$$

and

$$\frac{\Delta}{D} = \delta_2 \left(\frac{\Delta}{D}\right)_m$$

or

$$\Delta = \delta_2 \, n\Delta_m \tag{11}$$

where δ_1 and δ_2 are prediction factors for strain and deflection. The values of the prediction factors are determined from the results of tests conducted on the models. If no distortion of the design conditions exists, or if the distorted design conditions do not significantly affect the phenomena measured by strain and deflection, then δ_1 and δ_2 will be unity as determined from the test results. If δ_1 and δ_2 are not unity, a plot of prediction factor versus distortion factor α may indicate a relationship between the two which will be valuable in conducting further studies with the model system.

IV. PRELIMINARY TESTS

A. Introduction

This section describes the preliminary tests which were necessary prior to initiating the principal test program. The structures used throughout the investigation were five semicircular aluminum arches with integral floor plates. The arch diameters were 8, 12, 16, 20 and 24 inches. The length of each was twice the diameter, and the ratio of arch diameter to roof thickness $\left(\frac{D}{t}\right)$ was 80. Geometric similarity between arches was maintained in every significant aspect. Details of dimensions, fabrication and instrumentation of the arch structures are presented in Appendix B. A pilot test program was conducted prior to undertaking the extensive principal model testing and is reported in Appendix C. Appendix D presents derivations which were required to support this section and Appendix C.

It was necessary to conduct preliminary static bench tests on the five principal models to ascertain that the static response could be predicted accurately. If it could not be shown that the response of the structures scaled properly under simple static loading, then the results of the dynamically loaded buried arch tests could not be evaluated. The objectives of the preliminary tests were: (1) to ascertain that the structures constituted static scale models, and (2) to check out the structural instrumentation.

B. Static Bench Tests

1. Initial tests

After installation of the strain gages and deflection gages (LVDT's)

on the models (Appendix B), each structure was subjected to a loading as shown in Figure 4. The support under the floor was provided under the middle one-third rather than under the entire width because it was not practical, with the apparatus used, to provide a support as wide as the 24 inches required for the floor of the largest arch. Figure 5 shows the loading apparatus used.

The floor support for each structure was of 2-inch lumber cut to a width of exactly one-third the arch diameter. The uniform line load along the arch crown was applied through a bar by hydraulic jacks. The number of jacks selected for loading each arch allowed complete coverage of the length of the arch roof, thus minimizing longitudinal bending.

The total load on the arch was monitored during loading by controlling the hydraulic pressure to the jacks. The load was recorded by means of the two load cells under the floor support, which served as the sole load-bearing support for the structure. For each of the five structures, three repetitive sequences of load were applied, and the strain gage, Collins gage (LVDT) and load cell outputs were recorded on a galvanometer oscillograph. Strain and deflection were plotted against load from composite data from all three runs.

Two undesirable facts were apparent from these strain versus load curves. First, the variation of strain with load in gages a and b (at $\theta = 75^{\circ}$) was significantly nonlinear. Second, the response of the arches as measured by strain and deflection did not properly scale between the five arches. In only two cases, those being the 16-inch- and 24-inch-diameter arches, were the strain-load curves comparable. However, it turned out that the response of these two arches was quite close to that

predicted by the theoretical fixed-end arch. It was deduced that the nonlinear strain response was due to slight rotations which occurred in the joint between the roof and floor pieces as the load increased, and that this rotation ceased at some time when the joint finally bound up. This sequence, and the subsequent load-strain curve are shown schematically in Figure 6. The rotations were permitted by the imperfect fit of the roof piece in the floor groove. The tolerances between the two pieces varied from 0 to about 0.005 inch on each side of the roof piece, and the tolerance varied between structures as well as along each structure. It was essential that this problem of joint rotation be resolved prior to attempting the dynamic model tests.

2. Modification of springing line joint

The problem of establishing scaled static response became one of creating similar conditions of fixity in the springing line joints of all five structures. The approach taken was to strive for 100% fixity between the roof and floor pieces, or as close thereto as possible. For the purpose of establishing similitude between the structures, it was not essential that the degree of fixity be exactly 100%, but only that the degree of fixity be the same in all five structures. It was believed, however, that with the given physical joint condition, the end condition which would most readily yield similar response would be as near perfect fixity as possible.

The means taken to reach full fixity in the joint was to provide a material which could be injected into the void spaces in the joint to completely fill these spaces, and which could then be cured, with

negligible shrinkage, to a highly incompressible state. After such a material had cured in place, rotation of the roof piece in the groove would be prevented and the structure would respond as if the joint were homogeneous.

An investigation of possible materials to suit these requirements led to a study of the characteristics of epoxy resins. The specifications for a suitable epoxy were:

(1) low viscosity when mixed, so that the epoxy would flow readily into a very thin crack,

(2) very low shrinkage during curing,

(3) high modulus of compressibility when cured.

Five commercially available epoxy resins were investigated, and suitable tests were conducted on each to determine their characteristics of viscosity, shrinkage and compressibility, as well as their general adaptability to the immediate requirement. The epoxy selected as most suitable for the particular specifications was EPON® Resin 815, with n - aminoethylpiperazine (AEP) hardener, produced by the Shell Chemical Company.

This epoxy was used to treat the joints of all five structures. For the two smaller arches (8-inch and 12-inch diameter), the roof pieces were removed from the floor, the epoxy was placed in the groove and the roof was replaced. This procedure forced the fluid epoxy up into the space between the two pieces and assured complete filling of the joint. On the three larger arches, the roof pieces could not be removed due to their tighter fit. In these cases the structure was first loaded as shown in Figure 5, causing the joint to open on the inside of the roof (Figure 6,

load P_3). The epoxy was placed along the inside of the joint by means of a needle syringe, and it flowed readily into the crack as had been expected as a result of earlier investigation. Before the epoxy had begun to set, the load was removed and epoxy was placed along the outside of the joint where it flowed in. As well as could be determined, it appeared that this method of placing epoxy resulted in complete filling of the joint.

3. Subsequent bench tests

The static bench test previously described was repeated on each structure after the joints had been filled and the epoxy completely cured. The results of these subsequent tests are shown in Figures 7 through 10. These are dimensionless plots, and each plot represents a composite of the data from three consecutive tests of strain and deflection versus load on each arch. The extent of similitude between the five statically loaded structures is determined by comparing the slopes of the load-strain and load-deflection curves plotted in dimensionless coordinates. Slopes were used for purposes of comparison because in general the intercepts of these curves may vary. When this occurred, it was attributable to slack in the equipment prior to initial loading, which varied from test to test.

In Figure 7 the load-deflection curves are compared, and the nearly identical dimensionless slopes for all five structures indicate that they represent very good static scale models under the loading used. The theoretical dimensionless load-deflection curve for a fixed-end arch was calculated from Equation D10 and is shown as a dashed line for comparison. Even though the floor was supported over its middle third only, the high stiffness of the floor piece resulted in

deflections approximating those of a fixed-end arch.

Figure 8 presents the strain in gage c versus dimensionless load. Again the very nearly identical slopes indicate similitude of the five structures under the crown load as measured by strain at c. The zero offset of the load-strain curves was due to the lack of resolution in the instrumentation and reduction of records at very low loads. The theoretical strain at c for a fixed-end arch is shown by the dashed line.

Some bending did occur in the floor, as shown by the tensile strain at d in Figure 9. These strains were relatively low, but the values of the slopes of the dimensionless load-strain curves in Figure 9 were reasonably close, varying at the most between the 8-inch and 20-inch arches by 30%.

The strains at gages a and b were very small. This was to be expected, because a point of contraflexure occurs near $\theta = 75^{\circ}$ for a fixed-end arch under a line load along the crown (see Figure C10). Thus, small absolute differences in the strains at a and b resulted in large relative or percentage variations between structures. Load-strain curves for strains at a and b were plotted, similar to Figures 8 and 9. Then the dimensionless slopes of these plots for the five arches were compared on the scale shown in Figure 10. The vertical scale on the left is the ratio of unit strain per dimensionless unit load. The upper and lower limits of +0.13 and -1.00 were the dimensionless ratios calculated for a fully fixed-end and fully hinged-end arch, respectively, as shown at the right. The points plotted are the dimensionless strain-load ratios from gages a and b on each of the five structures. It was realized that the

experimental configuration did not constitute a perfect fixed-end condition, because of both the imperfect joints and the bending of the floor in the bench loading. Therefore, it was not intended to interpret the quantitative degree of end fixity in the structures from the relative fixity scale on Figure 10. The relative fixity served only as a frame of reference within which to compare the dimensionless strain-load ratios. It may be seen that although the values of these ratios were near zero and both plus and minus, the rather close grouping within the fixity scale indicates that the structures did respond in a similar manner as measured by strain at a and b.

One additional point may be mentioned in regard to Figure 10. In the case of the four smaller arches, gage a responded consistently lower (in tension) than did gage b, which indicates that some lack of symmetry existed. Although the consistent trend of asymmetry in these four arches may have been coincidental, there was a possibility that the loading apparatus was characterized by an inherent unobserved lack of symmetry. There was no measurable geometric distortion of symmetry in structural dimensions or strain gage placement.

C. Scaling of Natural Period of Vibration and Unit Weight of Structures

Prior to dynamic testing of the five structures, their natural periods of vibration were compared. These were determined by simply striking the center of the crown of each arch with a rubber-headed mallet and recording the response of strain gages a, b and c and the LVDT measuring crown

deflection. Although it was not precisely determined which mode of vibration was thus excited, it was apparent that the same mode was observed in each structure since in each case the dynamic strains at a and b were very much lower than that at c. It is probable that the mode excited was the first symmetric flexural mode, corresponding to the deflected structure under the crown load used in the static bench tests. For each structure the same frequency was observed in strain gage c and the LVDT.

The natural periods of vibration of the arches calculated from the recorded frequencies are plotted in Figure 11 versus arch diameter. It is seen that the natural period is directly proportional to the size of the arch, which agrees with the theoretical relation shown in Appendix D.

The structures were weighed just prior to installation in the LBLG test chamber. The weights are compared in Figure 12, which indicates that the structural weight was approximately proportional to the volume (cube of the linear dimensions). The greatest discrepancy is for the smallest structure, since the components of weight due to gages and appurtenances, which were not precisely scaled geometrically, comprised a relatively larger proportion of the total weight. For practical purposes the structures had the same unit weight of 35 pcf.

D. Summary and Conclusions

The original structures as fabricated did not constitute scale models under the static bench loading. Filling the springing line joint with a high-strength epoxy provided a high degree of end fixity without which the scaled response could not have been attained in the structures used. For the crown load, the springing line was subjected to relatively high strains

(see Figure C10), and for this reason this loading was a rather severe test of the filled joint. There was no apparent change in the epoxy-filled joint condition due to loading and unloading, since the structural response was the same for three repetitive loads in all cases. The preliminary tests satisfied the objectives of establishing similitude of static response for the test conditions and verifying the reliability of the gages used. The natural period of vibration was found to be proportional to the length scale as predicted from theory.

V. PRINCIPAL TESTS

A. Test Procedure

The test program which was conducted to verify the model relations developed in Section III consisted of two series of dynamic loadings in the LBLG. Series I consisted of eight shots at peak air overpressures of 30 to 165 psi, with the five structures buried at $H/D = 1.0$. Series II consisted of eight shots at peak overpressures of 31 to 221 psi and $H/D = 2.0$. A detailed description of the test facilities and procedures used is presented in Appendix B.

For each test series the five structures were installed in the LBLG test chamber and subjected to repeated dynamic loading without being removed. The pilot tests described in Appendix C had shown that such repeated loadings were feasible, and that no highly significant change in installation conditions between shots would be expected with the possible exception of a slight densification of the sand.

The test program reported herein constituted the first series of LBLG tests conducted on buried structures. For this reason several areas of uncertainty existed in planning the tests regarding such factors as test chamber sidewall effects, effects of the test chamber motion on structural response, nonuniformity of pressure across the specimen, instrumentation, etc. In addition to the data obtained for the primary purpose of evaluating the similitude relations, valuable supplementary information was gathered during the tests, which will be discussed later.

B. Data Reduction and Evaluation

The dependent variables appearing in the prediction equations were peak dynamic strain and peak dynamic deflection. These quantities were determined from the records of each shot for each structure. The identification of the dynamic peak on each record was relatively straightforward in most cases, but for certain gages, specifically strain gages c and cℓ, the identification of the peak dynamic response required considerable judgment in the interpretation of the record. This fact is evident in Figure 13, which is a typical record for strain gages a, c and d for the five structures. For purposes of reference during the tests, the structures were designated 1 through 5 in increasing order of size, so that gage records numbered 1 referred to the 8-inch arch, 2 referred to the 12-inch arch, and so on.

The dynamic strain at a and d rose to a maximum in about 5 msec and decayed thereafter. (The "hump" at approximately 15 msec is due to inertial effects in the LBLG and will be discussed later. This peak is not pertinent to the shock wave loading and response of the structure.) However, as seen in Figure 13, the strain at c rose somewhat erratically to an indefinite peak. Due to this rather inconsistent and indistinct response, identification of the peak dynamic strain at c required individual and careful interpretation of each record. In general, the value selected was the maximum value occurring during the first 10 msec of record.

Peak dynamic deflection was recorded clearly, as shown in Figure 14. The "overshoot" recorded in the 8-inch arch at its initial peak was

evident to some degree on every shot during Series I. It was felt that this early peak was somehow due to the proximity of this structure to the surface (8 inches), since it did not occur during Series II. For purposes of comparing peak dynamic deflections this "overshoot" was considered to be atypical of the general system studied, since it did not occur for the other structures. Therefore it was neglected, and the value recorded at about 5 msec was taken for the 8-inch arch in Series I.

Buried soil pressure cells were installed in the vicinity of the structures with the objective of comparing the relative level of soil stress between the five structures. As pointed out in Appendix B, adequate dynamic calibration of such gages is not possible at present, due to the lack of capability for providing a precisely known dynamic soil stress for reference. However, it was initially felt that records from these gages could be used to provide relative values of soil pressure from gage to gage. This did not turn out to be the case. Rather, the inconsistent peak pressure readings from the buried pressure cells resulted in scatter of data which exceeded the required accuracy. This scatter was believed to be primarily due to the effect of variations in gage placement conditions in the soil as well as the lack of adequate dynamic calibration procedures. The best possible evaluation of the records from these gages resulted in the conclusion that there was no consistent or extreme variation between the peak soil pressure at the locations of the structures. A typical record from the buried soil pressure cells is shown in Figure 15.

In order to relate structural response to dynamic loading, it was necessary to rely on the measurement of p_o, the surface pressure.

Reliable records from the pressure gages mounted in the wall of the firing chamber were obtained in all cases except shot 1, Series I. The peak overpressure p_o for each shot was taken from these records, a typical example of which is shown in Figure 16. The peak dynamic overpressure selected for reference throughout this analysis was the value recorded at about 5 msec. The initial peak at about 2 msec was more difficult to accurately identify and was not as consistently repeatable as was the value selected.

A characteristic of the LBIG is the dynamic response of the entire facility, including the central firing station and the test chamber (described in Appendix B), to the explosion of the charge. There is a motion of the entire device as evidenced by records from gages and structures buried in the test medium, and also from gages on the reinforcing steel in the columns of the central firing station. These records indicate the first motion at about 18 msec after the charge is detonated, with a subsequent periodic motion at a frequency of about 45 cycles per second. The time-dependent response observed in all gages, regardless of location, is in phase, which indicates that this response is a gross motion of the device rather than a matter of incident or reflected shock waves within the test medium. Additional proof consists of the observation that more deeply buried soil pressure gages in the medium receive a relatively larger inertial load than do shallow-buried gages, due to the greater mass of soil above the deeper gages.

Due to these facts the "hump" which appeared in every record of structural strain and deflection at about 18 msec was neglected for purposes of identifying structural response to the incident shock wave.

This inertial effect in the LBLG acts as a limitation on buried structure tests where structural response to shock wave loading is to be studied for times exceeding 15 msec after zero time.

The peak overpressures, strains and deflections for each shot are listed in Tables 2-5.

C. Primary Results

Figures 17 and 18 show the peak strain at locations a and b versus peak overpressure for all five structures for the two test series. For purposes of comparison, the peak strains at a and b were averaged for each structure on each shot. This was necessary due to the fact that the structural response was not perfectly symmetrical in each case; that is, gages a and b for a given arch did not record exactly the same peak strain at a given overpressure. The asymmetry was rather slight in that these two strains agreed to within $\pm 20\%$ or better for a given structure in all cases. There was no qualitative or quantitative correlation between the asymmetry observed in these tests and that observed in the static bench tests described in Section IV. Thus, it was assumed that the average of the peak strain at a and b represented the value of peak strain at $\theta = 75^{\circ}$ for symmetrical response, and this value was used for comparison between the five structures.

Figures 19 through 24 show peak dynamic strains at c and d and peak dynamic deflections versus overpressure. Scaled deflection Δ/D versus overpressure is plotted in Figures 25 and 26. The significance of these response versus overpressure curves will be discussed in Section VI.

The time to peak deflection t_m was reduced from the Collins gage

records and these data appear in Table 6. For an undamped single-degree-of-freedom system initially at rest and subjected to a step pulse, it can be shown that t_m is equal to one-half the natural period of vibration τ. Although the actual soil-structure system observed in these tests certainly is characterized by some amount of damping, and the assumption of an undamped single-degree-of-freedom system may be an oversimplification, for purposes of estimating τ this idealization was assumed. Due to the shocking-up of the stress wave in the sand, the structures were subjected to a virtual step pulse. Under these conditions, the natural periods were calculated from $\tau = 2t_m$, Table 6. These values of τ are plotted against arch diameter D in Figure 27.

The deflection gage records on magnetic tape were played back at condensed time to observe the decay characteristics of the deflection-time curve. Figure 28 is a tracing of a typical set of these records. It was necessary to draw a smooth curve through the actual record due to the electronic noise level; consequently there may have been small oscillations in the LVDT output which do not appear in Figure 28.

D. Supplementary Information

Upon completion of Series I, the structures were removed from the test chamber. On each of the three largest arches, the tape seal covering the gap around the endwalls was very slightly torn in two or three places at about 10 or 20 degrees above the springing line, and a small amount (1 to 5 cubic inches) of sand had seeped inside these arches. For Series II this tape was reinforced with several layers and slack was left in the tape across the gap. After Series II, no damage to the tape seal was observed.

Investigation of the interior of the arches after Series I revealed that the endwall tie assembly (Figures B3 and B6) had buckled in every structure. The stainless steel tie bars were geometrically scaled in diameter, and prior to Series I these bars were perfectly straight. The tie bar assemblies had been designed to withstand without buckling a uniform pressure on the endwalls equal to one-half the vertical pressure in the soil. This design necessarily required some simplifying assumptions, and was felt to be unconservative since no safety factor was included. Therefore, it was not surprising that the endwall tie assemblies buckled. As a result of the eight loadings in Series I, the tie bars retained a buckled shape, with residual deformations at the stiffening trusses on the order of 1/4 inch to 1 inch from the initially straight configuration.

The elevations of the test structures within the LBLG test chamber were accurately determined using a surveyor's level, before and after each test series. Table 7 indicates the depths of the structures below the surface of the test medium. There was very little change in the elevations of the structures after the eight shots of Series I, with the exception of the 8-inch arch. On shot 7 the membrane near the surface of the sand above this arch ruptured slightly, allowing the dynamic air overpressure to enter the sand. As a result, after this shot the elevation of the sand surface above the 8-inch arch was about 2 inches higher than the rest of the specimen. It is certain that the dynamic pore pressure reached to the depth of the 8-inch arch, as evidenced by its orientation after recovery and the change in sand density near the structure. The structure was tilted 15° sideways and 9° longitudinally and had moved 2-7/16 inches upward. The post-Series I average density at this structure was

104.3 pcf, a decrease of 3.1 pcf which did not occur elsewhere in the specimen. During shot 5 of Series II the membrane again ruptured above the 8-inch arch. Peak strains and deflections from this structure after that shot were apparently significantly influenced by this disturbance and were thus discarded for purposes of analysis. These results illustrate the potential detrimental effects of dynamic pore pressure on small shallow-buried test structures in dry sand.

Arrival times of the stress wave in the soil were recorded at the structures and at depths of 4.83 and 9.33 feet in the test medium during Series I. These are listed in Table 8 and plotted in Figure 29. The average wave velocity over the entire depth of the specimen was computed for each shot (Table 8) and is plotted for various overpressures in Figure 30.

VI. ANALYSIS OF RESULTS

A. Design Conditions

The design conditions required for similitude as derived in Section III were in general satisfied in the test environment. Geometric similarity was faithfully achieved in all significant respects. As far as could be determined, the surface overpressure for each of the five structures was equal. The design conditions requiring that the pertinent engineering properties of the soil be equal in model and prototype led to the requirement that the density of the dry sand be the same in each of the systems. Soil density samples were taken in the vicinity of the structures prior to each test series to verify the degree of uniformity of density. There was some variation in soil density at the structures, as shown in Appendix B, and the possible significance of this variation will be discussed later. The effect of the distorted time scale will also be considered.

B. Prediction Equations

1. Peak dynamic strain

Verification of the proposed model theory is evaluated by the extent to which the prediction equations were satisfied by the test results. The prediction equation for strain stated that at corresponding points, the peak dynamic strain should be equal in all five structures when subjected to the same peak overpressure. This indicates that the data points on the strain versus overpressure plots (Figures 17 through 22) should collapse

at a given overpressure for all five structures.

Inspection of these plots reveals that the agreement with theory is quite good. A statistical evaluation of the peak dynamic strains reveals the quantitative agreement between structures. For each shot, the peak dynamic strain at each gage was averaged for the five structures. The standard deviation in peak dynamic strain was calculated from

$$\sigma_{\epsilon} = \left[\frac{\sum_{n} (\epsilon - \bar{\epsilon})^2}{n - 1} \right]^{\frac{1}{2}}$$

where n is the number of structures for which peak strain was recorded on a given shot, usually five. These standard deviations are given in Table 9. It is noted that, in general, the value of one standard deviation was on the order of 10% of the average peak strain. Better correlation was found where the strains at a and b were averaged. A relatively greater deviation was evident for peak strain at c due to the fact that these strains were of smaller magnitude, thus subject to a larger percent recording error, and because of the previously mentioned difficulty of consistently identifying the actual peak dynamic strain on the record.

The agreement of the observed peak dynamic strains with the prediction equation is considered to be good. Especially good agreement between structures was noted in the peak strains averaged between a and b. This would indicate that if the response of a prototype is expected to be symmetrical, a statistically more accurate prediction could be obtained by instrumenting both sides of the model. Then as long as the model response is only slightly asymmetric, an average of the strain measured

on the two sides may be taken as the value upon which the prediction is based.

The average peak dynamic strains for all five structures from Table 9 are plotted against peak overpressure in Figures 31 through 34. These plots show a nonlinear variation of peak strain with overpressure in the range of elastic structural response. Previous investigators have reported linear variation with overpressure of peak elastic dynamic strain up to 400 psi (19) in very stiff buried cylinders, and peak dynamic moment in a very flexible buried arch up to 23 psi (2). Recent experiments by A. F. Dorris at the University of Illinois on buried cylinders of different flexibilities have resulted in nonlinear curves relating peak dynamic elastic moment and thrust to peak overpressures up to 500 psi.*

The curves in Figures 31 through 34 are representative of the behavioral dynamic strain-overpressure relationship for these test conditions, and the nonlinearity cannot be attributed solely to experimental errors. The data points each represent the average of the readings from five different structures, and the shape of the curve is generally the same for the strain at all three locations on the structure for each test series. These facts indicate that the curves represent actual behavior rather than random scatter.

It is not possible to explain with confidence the nonlinear trend observed. It may be conjectured that the effect of repeated loading on the same installation may somehow contribute to the observed nonlinearity. However, it is believed that the most likely cause is the dependence of the shear strength and stress-strain relationships in dry sand upon the

*Dorris, A. F., Vicksburg, Mississippi. Private communication. 1964.

level of stress and the magnitude of structural deformations. For different overpressure levels and varying magnitude of structural deformations, the strength and stiffness of the soil immediately surrounding the structures will vary. Thus, it would not be expected that a perfectly linear relationship between peak dynamic strain at a point and overpressure should exist for systems in which the properties of the soil noticeably influence the structural response, which may be the case of the system studied herein.

2. Peak dynamic deflection

The prediction equation stated that scaled peak dynamic deflection Δ/D should be equal in all five structures at the same peak overpressure. The scatter in scaled peak dynamic deflection was somewhat greater than that for peak strains. In Figures 25 and 26 the best straight line through zero was fitted to the scaled peak dynamic deflections. For Series I these curves were coincident for the three smallest arches, in agreement with the prediction equation. However, it is noted that for Series I the scaled peak deflections for the two largest arches were somewhat higher than those of the smaller three. A probable cause for this was the somewhat lower sand density around these two larger arches. Figure 35 shows the slope of the scaled deflection-overpressure curves, calculated from Figure 23, related to the average sand density at each structure from soil tests made prior to Series I (Appendix B). There is an obvious trend that lower soil density resulted in higher values of scaled deflection. This is as might be expected, since the less dense sand should not resist the structural deformation as much as does the denser sand.

For Series II, Figure 26 shows that the scaled deflections of the 8-inch and 20-inch arches did not coincide with those of the other three arches. The pretest average soil densities in the vicinity of the structures for Series II (Appendix B) varied by only ± 0.6 pcf, and no correlation existed between scaled deflection and this small variation in density. The maximum variation between slopes of the scaled deflection-overpressure curves for Series II was 16%.

On the basis of the plots of scaled peak dynamic deflection versus overpressure, the agreement of the test results with the prediction equation is considered reasonable. It appears that if accurate predictions of deflection are to be made, good control of the soil density in the vicinity of the structures is very important.

C. Effect of Depth of Burial

Comparison of the results of Series I and Series II indicates the influence of depth of burial for depths of one and two diameters. This comparison was drawn by calculating the average slope (best straight-line fit) of the dynamic strain-overpressure and scaled deflection-overpressure curves. These slopes are listed in Table 10. It may be seen that the peak response at $H/D = 2.0$ was lower than that at $H/D = 1.0$ for each gage location. The greatest benefit of the deeper burial was in reducing the peak dynamic strain at locations a and b, for $\theta = 75^{\circ}$.

Since the LBLG is a one-dimensional loading device, exclusive of sidewall friction effects, the reduction in structural response with depth is due only to the increased depth of cover over the arches and is not attributable to spatial dispersion of peak soil pressure. Additionally,

since depth of burial was scaled for the five structures, and since the scaled response of all structures was in general the same, there was no indication that attenuation of peak soil pressure with depth significantly affected the structural response. This observation is limited to the definition of LBLG peak overpressure selected in this study, as discussed in Section V and shown in Figure 16. Therefore, the benefit of the increased cover from $H/D = 1.0$ to $H/D = 2.0$ can be best accounted for by attributing it to soil arching. This is in accordance with the observation that the difference in response for the two depths varied between the four parameters measured, since it would not be expected that the change in arching conditions would affect all aspects of structural response identically.

The reduction in peak response from Series I to Series II was of relatively low magnitude, which is not unusual for depths exceeding $H/D = 1.0$. It has been shown by a number of theoretical and experimental investigators that the primary reduction in structural response with increasing depth of burial, due to arching alone, occurs for H/D less than about 1.

D. Time Scaling

The prediction equations were derived for peak dynamic response, without reference to the time at which peak response occurred. However, it is of interest to compare the time-dependent response of the five scaled arches.

It is seen in Figure 27 that the natural period of the buried arches for Series I, based on the observed time to peak deflection, is a linear

function of the arch diameter. Extrapolation of this line to $\tau = 0$ yields an intercept of 4.8 inches. This nonzero intercept cannot be explained on the basis of available data. It seems unusual that the data points should plot linearly with such little scatter, yet extrapolation should yield a nonzero intercept, which is not physically meaningful in this case. Additional investigations of the natural periods of buried structures are necessary to clarify this relationship.

The observed natural periods were compared with values predicted by an equation derived from the equivalent surcharge loading method developed at WES (9). Figure 36 shows the results of this equation, which is solved in Appendix D for the present case. The natural period is a function of arch diameter and also of K, the horizontal load factor for the equivalent surcharge load. From the figure, the observed values of τ from the principal and pilot tests fall in the region of approximately $0.85 < K < 0.95$. This is a very reasonable range of values for K. For $K = 1.0$ the equivalent surcharge load becomes a hydrostatic loading on the arch. For K less than about 0.5, the arch response will be predominantly flexural. The mode of response of the arches in these tests was primarily compressive, as evidenced by compressive strains at a, b and c. This would tend to indicate an actual load on the arch more closely approximated by a hydrostatic load than by a flexural loading. Thus the high value for K calculated from the equivalent surcharge method is in qualitative accordance with the observed structural response.

Although rise time of the structural response was observed to depend upon the size of the model, the time-dependent decay of dynamic deflection was independent of arch diameter as seen in Figure 28. Comparison of

Figure 28 with Figure 15b shows that the deflection-time curve has exactly the same general shape as the pressure-time curve from a buried soil pressure cell. Thus, the decay of the dynamic deflection appears to be dependent upon the shape of the pressure decay. This is reasonable to expect, since after the first 10 msec or so the structural response is no longer dependent upon its natural period. For these conditions the structural response may be thought of as virtually static, and the structural deflection at any time should be proportional to the soil stress at that time. This is in accordance with the observation made by Murphy, Young and Martin (19) that after peak response is reached, the strain will follow the decaying pressure pulse.

E. Buckling of Endwall Tie Assembly

The initial scope of this investigation was limited to the prediction of elastic strains and deflections in the arch shell. However, after Series I it was found that the endwall tie assembly had buckled in all five structures. Since the structures were not visually inspected between shots, it is not possible to determine the surface overpressure at which this buckling occurred for each structure. However, the fact that not only one but all five structures underwent plastic deformation in the axially loaded endwall tie bars after a series of similar loadings is of significance to the use of models in predicting inelastic response.

If it is desired to extend the similitude relations developed in Section III into the range of response beyond the elastic limit, it is necessary to include the variables σ_y , yield strength of the structural material, and E_p , a plastic modulus for the structural material which

defines the shape of the stress-strain curve beyond the elastic limit. The two additional variables require the addition of two Pi terms to complete the functional relationship for inelastic response. These Pi terms may be taken as $\frac{\sigma_y}{E}$ and $\frac{E_p}{E}$. Equating these terms for model and prototype results in the design conditions $\sigma_{ym} = \sigma_y$ and $E_{pm} = E_p$, for $E_m = E$. These can be satisfied if the same material is used in model and prototype. Therefore, the structures used in these tests should constitute properly scaled models for predicting inelastic response.

The observed buckling can then be interpreted as experimental evidence that these similitude relations for inelastic response may be adequate for the conditions of the tests reported. It is not proposed that the capability for modeling plastic buckling has been proven in these tests, but that it has been at least shown to be feasible.

F. Supplementary Information

The effect of repeated loading on the characteristics of the test system was considered of little significance after the first few shots of each series. The results of tests on six soil density samples taken at various locations after Series I indicated an average increase in density of less than 0.5 pcf after the eight shots. In order for the overall specimen density to change significantly, a volume change in the specimen must occur. The changes in elevation of the membrane after Series I averaged about 1/2 inch down, and the structures averaged a total decrease in elevation of about 1/4 inch (Table 7). An average differential settlement of 1/4 inch in the upper 1-1/2 feet of sand was then estimated, which is a residual consolidation of about 1-1/2%. Although the specific influence

of an increase in soil density of this magnitude on structural response is not known, it is believed that the effect was slight.

The variation of wave velocity in the medium with overpressure, shown in Figure 30, is of interest. For comparison, the theoretical wave velocity was calculated from $c = \sqrt{M_s/\rho_s}$, where M_s is the constrained secant modulus in one-dimensional compression. This modulus was determined from the stress-strain curve given in Appendix B for the sand used in this test at a dry density of 106.0 pcf. The calculated velocity curve lies below the observed values. This is qualitatively correct in that the dynamic secant modulus should actually be somewhat higher than the static modulus within the range of overpressures considered. An upper bound curve results from $c = \sqrt{M_t/\rho_s}$, where M_t is the constrained tangent modulus in one-dimensional compression. Values for M_t were calculated from Figure B12 and represent the maximum possible static modulus.

VII. SUMMARY, CONCLUSIONS AND RECOMMENDATIONS

The objective of this study was to investigate a modeling procedure for predicting the elastic behavior of a laboratory-size prototype buried arch structure subjected to a dynamic surface overpressure.

Design conditions and prediction equations were derived from the theory of similitude based on dimensional analysis, selecting as dependent variables peak dynamic strain and deflection. The principal experimental program consisted of the initial series of tests in the Large Blast Load Generator employing buried structures. A static bench test program on the test structures revealed that modification of the springing line joint prior to the principal tests was necessary to provide properly scaled models.

Within the capabilities of existing buried soil pressure gages and soil density measuring techniques, the required design conditions were adequately satisfied in the principal tests. The effect of neglecting gravity scaling and neglecting scaling of dynamic loading times was apparently negligible concerning the prediction of peak dynamic strains and deflections, under the conditions of these tests.

Nonlinear dynamic strain-overpressure relationships were observed. It appeared that structural deflections were dependent in part upon the density of the sand in the vicinity of the structure. The natural periods of the buried arches were shown to be directly related to the size of the structures. A reasonable prediction of the natural period of vibration of the buried arch was arrived at by the use of an existing design procedure (9) and a reasonable assumption for the value of K. Observed buckling of

the endwall tie assembly in all five structures indicated the feasibility of predicting structural response beyond the elastic limit by means of scale models.

Based on the observed results from the principal tests, the primary conclusion is reached that the proposed model theory was verified with a reasonable degree of accuracy, within the range of parameters investigated. The validity of this conclusion must be limited to the conditions which existed in these tests. The established similitude relations may be summarized by stating that geometrically similar systems with the same materials in model and prototype undergo the same peak dynamic strain and geometrically scaled peak dynamic deflections when subjected to the same dynamic surface overpressure.

The applicability of the conclusions from this investigation is necessarily restricted to the conditions of the study. The study was limited to specific conditions of structural geometry, size and flexibility, soil properties and scaled and absolute depths of burial. Further investigations are necessary to extend the modeling procedure for application in other soil-structure interaction problems. The following general areas for future study are recommended:

1. Modeling of response of structures buried in soil media other than dense, dry sand should be investigated.

2. Validity of the model theory should be established for structures of different geometries and greater flexibility.

3. Prediction equations should be verified for a greater range of length scales, up to 10 or greater, to include correlation of laboratory systems with full-scale prototype systems.

4. Procedures should be developed for modeling structural response beyond the elastic limit to the point of failure.

VIII. LITERATURE CITED

1. Ahlers, E. B. Experimental methods of determining the behavior of underground structures under dynamic loads. Chicago, Armour Research Foundation. November 1961.

2. Allgood, J. R., C. R. White, R. F. Swalley and H. L. Gill. Blast loading of small buried arches. U. S. Naval Civil Engineering Laboratory Technical Report R-216. April 1963.

3. American Machine and Foundry Co. Study of the use of models to simulate dynamically loaded underground structures. Air Force Special Weapons Center Technical Documentary Report 62-3. February 1962.

4. Antebi, J., H. D. Smith, S. D. Sharma and H. G. Harris. Evaluation of techniques for constructing model structural elements. Massachusetts Institute of Technology, Department of Civil Engineering Report R62-15. May 1962.

5. Bridgman, P. W. Dimensional analysis. Rev. ed. New Haven, Yale University Press. c1931.

6. Carroll, W. F. Dynamic bearing capacity of soils; vertical displacements of spread footings on clay: static and impulsive loadings. U. S. Army Engineer Waterways Experiment Station Technical Report No. 3-599, Report 5. September 1963.

7. den Hartog, J. P. The lowest natural frequency of circular arcs. London, Edinburgh and Dublin Philosophical Magazine and Journal of Science 5: 400-408. 1928.

8. Engineering Research Associates, Inc. Underground explosion test program. Final report, Vols. I and II. St. Paul, Minnesota, Author. ca. 1953.

9. Flathau, W. F., R. A. Sager and F. A. Luzi. Design and analysis of underground reinforced-concrete arches. U. S. Army Engineer Waterways Experiment Station Technical Report No. 2-590. January 1962.

10. Hansen, R. J. and H. D. Smith. Response of buried arch and dome models (U). U. S. Atomic Energy Commission Report POIR-2222. (confidential). August 1962.

11. Harris, H. G., P. J. Pahl and S. D. Sharma. Dynamic studies of structures by means of models. Massachusetts Institute of Technology, Department of Civil Engineering Report R63-23. September 1962.

12. Jones, G. H. S. The use of models in the study of blast effects of simulated nuclear weapons. Suffield Experimental Station Technical Paper No. 132. April 1958.

13. Kennedy, T. E. and A. J. Hendron, Jr. The dynamic stress-strain relation for a sand as deduced by studying its shock wave propagation characteristics in a laboratory device. Preprint of paper presented at 1964 Army Science Conference, West Point, New York, June 1964. Vicksburg, Mississippi, U. S. Army Engineer Waterways Experiment Station. June 1964.

14. Lycan, D. L. Design of the large blast load generator. U. S. Army Engineer Waterways Experiment Station Miscellaneous Paper No. 2-426. April 1961.

15. Melin, J. W. and S. Sutcliffe. Development of procedures for rapid computation of dynamic structural response. University of Illinois Civil Engineering Studies, Structural Research Series No. 171. January 1959.

16. Merritt, J. L. and N. M. Newmark. Design of underground structures to resist nuclear blast. Vol. 2. Urbana, Illinois, Department of Civil Engineering, University of Illinois. April 1958.

17. Murphy, G. Similitude in engineering. New York, the Ronald Press. c1950.

18. Murphy, G. and D. F. Young. A study of the use of models to simulate dynamically loaded underground structures. Air Force Special Weapons Center Technical Documentary Report No. 62-2. January 1962.

19. Murphy, G., D. F. Young and C. W. Martin. Use of models to predict the dynamic response of dynamically loaded underground structures. Air Force Weapons Laboratory Technical Documentary Report No. 63-3064. November 1963.

20. Smith, H. D., J. Antebi and R. J. Hansen. Study of the applicability of small scale models for the investigation of air blast effects on structures (U). Massachusetts Institute of Technology, Department of Civil Engineering Report DASA-1195. (secret). May 1961.

21. Smith, H. D., R. W. Clark and R. P. Mayor. Evaluation of model techniques for the investigation of structural response to blast loads. Massachusetts Institute of Technology, Department of Civil Engineering Report R63-16. February 1963.

22. Swalley, R. F. Behavior of buried model arch structures (U). U. S. Atomic Energy Commission Report POR-2224. (confidential). May 1963.

23. Tener, R. K. The application of similitude to protective construction research. Preprint of paper presented at the Soil-Structure Interaction Symposium, The University of Arizona, Tucson, Arizona, June 8-11, 1964. (Proceedings to be published).

24. Urquhart, L. C., C. E. O'Rourke and G. Winter. Design of concrete structures. 6th ed. New York, McGraw-Hill. 1958.

25. U. S. Army Engineer Waterways Experiment Station. Soils laboratory tests on Cook's Bayou sand. Unpublished memorandum for record. Mimeo. Vicksburg, Mississippi, Author. 1963.

26. U. S. Army Engineer Waterways Experiment Station. Status report for blast load generator facility. Vicksburg, Mississippi, Author. July 1963.

27. VanHorn, D. A. and R. K. Tener. A study of loads on underground structures. Iowa State University of Science and Technology Engineering Experiment Station Final Report, Project 434-S. 1963.

28. Whiffin, A. C. and S. A. H. Morris. Piezoelectric gauge for measuring dynamic stresses under roads. The Engineer 213: 741-746. 1962.

29. Whitman, R. V. and K. A. Healy. Shear strength of sand during rapid loadings. American Society of Civil Engineers Transactions 128, Part I: 1553-1594. 1963.

TABLES

Table 1. List of pertinent variables

Symbol	Definition	Basic dimensions
ϵ	Peak dynamic strain in the structure at a point	--
Δ	Peak dynamic deflection of structure at a point	L
D	Arch diameter	L
H	Depth of burial	L
λ	Any significant length	L
E	Modulus of elasticity of structural material	FL^{-2}
ρ	Density of structural material	$FL^{-4}T^2$
ρ_s	Density of soil	$FL^{-4}T^2$
c	Cohesion intercept from shear-strength diagram	FL^{-2}
ϕ	Angle of internal friction	--
M_s	Constrained secant modulus of soil in one-dimensional compression	FL^{-2}
E_s	Secant modulus of soil from a triaxial test	FL^{-2}
p_o	Surface overpressure (function of time)	FL^{-2}
g	Acceleration due to gravity	LT^{-2}
t	Time	T

Table 2. Peak dynamic strains, Series I (μin./in.)

(C = compression, T = tension)

	Shot 1	Shot 2	Shot 3	Shot 4	Shot 5	Shot 6	Shot 7	Shot 8
p_o(psi)→	est. 75	51	54	73	109	130	165	30
Gage								
1a	635C	500C	460C	600C	835C	1200C	1800C[a]	194C
2a	570C	415C	406C	580C	680C	965C	1290C	274C
3a	632C	443C	420C	570C	745C	960C	1320C	300C
4a	565C	440C	429C	530C	735C	850C	1140C	259C
5a	NR[b]	530C	485C	645C	860C	1170C	1575C	131C
1b	NR	387C	362C	440C	605C	810C	1245C[a]	NR
2b	NR	483C	471C	495C	780C	890C	1440C	NR
3b	NR	512C	463C	600C	900C	965C	1365C	363C
4b	NR	492C	430C	570C	855C	915C	1270C	NR
5b	NR	390C	382C	530C	700C	830C	1260C	NR
Ave. 1a,b	NR	434C	409C	570C	723C	1005C	1523C[a]	est. 160C
Ave. 2a,b	NR	449C	438C	538C	730C	935C	1365C	est. 250C
Ave. 3a,b	NR	478C	442C	585C	822C	965C	1340C	332C
Ave. 4a,b	NR	466C	430C	550C	795C	880C	1205C	est. 280C
Ave. 5a,b	NR	460C	434C	588C	780C	1000C	1420C	est. 100C
1c	94C	73C	81C	88C	151C	155C	NR	30T
2c	100C	80C	74C	85C	151C	146C	273C	18T
3c	106C	62C	76C	101C	148C	160C	235C	43T
4c	96C	NR	80C	68C	129C	185C	256C	27T
5c	75C	60C	55C	65C	158C	173C	264C	31T
1d	NR	635T	604T	725T	1100T	1190T	NR	336T
2d	616T	510T	509T	695T	960T	1055T	1470T	407T
3d	635T	NR	540T	675T	955T	1140T	1480T	425T
4d	740T	563T	522T	640T	975T	1160T	1540T	476T
5d	805T	NR	584T	700T	1090T	1320T	1880T	NR
1cℓ	NR	NR	289T	378C	NR	490T	404T[a]	216C
2cℓ	87T	127T	90T	128C	NR	14T	144T	17C
3cℓ	128T	41T	40T	64C	NR	95T	71T	6C
4cℓ	253T	46T	55T	113T	NR	140T	98C	29C
5cℓ	NR	18T	33T	58T	NR	80C	5C	55C

[a]Records from structure 1 for shot 7 were disregarded due to disturbance of structure; see text.

[b]NR designates no record for this data channel.

Table 3. Peak dynamic strains, Series II (μin./in.)

(C = compression, T = tension)

	Shot 1	Shot 2	Shot 3	Shot 4	Shot 5	Shot 6	Shot 7	Shot 8
p_o(psi)→	31	59	78	119	117	177	159	221
Gage								
1a	195C	446C	462C	847C	548C[a]	1920C[a]	1538C[a]	1935C[a]
2a	155C	393C	484C	752C	924C	1182C	1216C	1673C
3a	140C	389C	309C	774C	821C	1090C	1062C	1455C
4a	185C	395C	537C	689C	1090C	1028C	980C	NR
5a	179C	489C	618C	1008C	1118C	1452C	1447C	1926C
1b	170C	372C	483C	767C	632C[a]	1580C[a]	1312C[a]	1825C[a]
2b	250C	395C	485C	718C	770C	1008C	960C	1227C
3b	200C	438C	690C	839C	936C	1238C	1176C	1562C
4b	230C	396C	551C	776C	818C	1212C	1184C	1626C
5b	150C	342C	544C	903C	922C	959C	894C	1501C
Ave. 1a,b	178C	409C	472C	807C	590C[a]	1750C[a]	1425C[a]	1880C[a]
Ave. 2a,b	198C	394C	484C	735C	847C	1095C	1088C	1450C
Ave. 3a,b	170C	413C	499C	806C	879C	1164C	1119C	1508C
Ave. 4a,b	207C	396C	544C	732C	954C	1120C	1082C	NR
Ave. 5a,b	165C	415C	581C	955C	1020C	1205C	1170C	1714C
1c	5C	71C	62C	147C	40C[a]	NR[b]	167C[a]	NR
2c	33C	62C	84C	174C	168C	232C	163C	267C
3c	25C	57C	74C	165C	122C	212C	175C	255C
4c	24C	55C	58C	146C	123C	203C	176C	239C
5c	48C	78C	84C	141C	145C	225C	183C	339C
1d	200T	419T	670T	1190T	695T[a]	1762T[a]	NR	2770T[a]
2d	250T	420T	651T	973T	1088T	1438T	1462T	2039T
3d	185T	NR	639T	1038T	1113T	1495T	1496T	1966T
4d	290T	434T	646T	927T	994T	1395T	1421T	2055T
5d	195T	437T	518T	852T	891T	NR	NR	NR

[a]Records from structure 1 for shot 5 and subsequent shots were disregarded due to disturbance of structure; see text.

[b]NR designates no record for this data channel.

Table 4. Peak dynamic deflections and scaled deflections, Series I

	Shot 1	Shot 2	Shot 3	Shot 4	Shot 5	Shot 6	Shot 7	Shot 8
p_o(psi)→	est. 75	51	54	73	109	130	165	30
				Peak dynamic deflection (inches)				
Gage								
1x	0.0264	0.0210	0.0225	0.0264	0.0427	0.0435	0.342[a]	NR[b]
2x	0.0318	0.0249	0.0308	0.0362	0.0615	0.0725	0.0957	NR
3x	0.0460	0.0345	0.0417	0.0550	0.0860	0.1010	0.1200	NR
4x	0.0715	0.0568	0.0609	0.0744	0.1139	0.1245	0.174	NR
5x	0.1019	0.0758	0.0817	0.0954	0.1445	0.1680	0.225	NR
				Scaled deflection Δ/D (inches/inch)				
1x	0.00330	0.00262	0.00281	0.00330	0.00533	0.00544	0.00428[a]	NR
2x	0.00265	0.00208	0.00257	0.00302	0.00512	0.00604	0.00797	NR
3x	0.00288	0.00216	0.00261	0.00344	0.00537	0.00631	0.00750	NR
4x	0.00357	0.00284	0.00304	0.00372	0.00569	0.00622	0.00870	NR
5x	0.00424	0.00316	0.00340	0.00397	0.00602	0.00700	0.00937	NR

[a]Records from structure 1 for shot 7 were disregarded due to disburbance of structure; see text.

[b]NR designates no record for this data channel.

Table 5. Peak dynamic deflections and scaled deflections, Series II

	Shot 1	Shot 2	Shot 3	Shot 4	Shot 5	Shot 6	Shot 7	Shot 8
p_o(psi)→	31	59	78	119	117	177	159	221
				Peak dynamic deflection (inches)				
Gage								
1x	0.0045	0.0194	0.0264	0.0446	0.0435	0.0803[a]	0.0767[a]	0.0963[a]
2x	0.0138	0.0280	0.0460	0.0643	0.0649	0.0992	0.0934	0.1058
3x	0.0128	0.0309	0.0525	0.0854	0.0942	0.1352	0.1182	NR[b]
4x	0.0388	0.0547	0.0712	0.1211	0.1246	0.1780	0.22	NR
5x	0.0227	0.0547	0.0757	0.1240	0.1362	0.190	0.192	NR
				Scaled deflection Δ/D (inches/inch)				
1x	0.00056	0.00242	0.00331	0.00557	0.00544	0.0100[a]	0.00959[a]	0.0120[a]
2x	0.00115	0.00234	0.00383	0.00535	0.00540	0.00827	0.00778	0.0089
3x	0.00080	0.00193	0.00328	0.00534	0.00588	0.00847	0.00739	NR
4x	0.00194	0.00273	0.00356	0.00606	0.00623	0.00890	0.011	NR
5x	0.00095	0.00228	0.00316	0.00517	0.00567	0.00793	0.00800	NR

[a]Records from structure 1 for shot 5 and subsequent shots were disregarded due to disturbance of structure; see text.

[b]NR designates no record for this data channel.

Table 6. Time to peak deflection t_m, Series I

Arch D (in.)→	8	12	16	20	24
Shot					
1	0.78	[2.40][a]	2.78	[4.30][a]	[6.20][a]
2	0.78	2.02	2.78	3.80	4.30
3	0.82	1.82	2.58	3.33	4.34
4	0.83	1.49	2.61	3.82	4.84
5	0.76	1.39	2.18	3.10	4.05
6	0.62	1.69	2.18	3.12	4.00
7	0.50	1.50	2.82	3.75	4.87
Average t_m	0.73	1.65	2.56	3.49	4.40
$\tau = 2t_m$	1.46	3.30	5.12	6.98	8.80

[a]These values discarded in averaging.

Table 7. Depths of burial

Arch D (inches)	Depth of arch crown below membrane (inches)			
	Pre-Series I	Post-Series I	Pre-Series II	Post-Series II
8	8	5-9/16[a]	16	16-3/8
12	12	12-1/4	24	24-5/16
16	16	16-1/4	32	32-3/16
20	20	20-3/8	40	40-1/8
24	24	24-7/16	48	48-3/16

[a]This arch was moved considerably on shot 7.

Table 8. Stress wave arrival times, Series I

Shot→	2	3	4	5	6	7	8
p_o(psi)→	51	54	73	109	130	165	30
Depth (feet)	Arrival time (msec)						
0.00	1.1	1.5	1.9	1.9	1.9	1.8	1.4
0.67	2.4	3.1	2.0	2.0	2.6	2.6	3.0
1.00	1.7	2.2	3.0	2.8	1.7	2.0	2.7
1.33	2.6	3.1	2.6	2.6	2.4	2.6	3.8
1.67	3.0	3.5	3.4	3.1	2.6	2.8	4.4
2.00	3.4	4.0	3.5	3.2	3.2	3.2	5.0
4.83	6.2	6.45	5.75	5.40	5.03	4.90	8.70
9.33	9.6	10.00	8.92	8.40	7.96	7.75	12.95
	Average velocity, 0-9.33' (fps)						
	1100	1100	1330	1430	1540	1570	805

Table 9. Averages and standard deviations for peak dynamic strain

Shot	$\bar{\epsilon}_{a,b}$ (μin./in.)	$\pm\sigma_{\epsilon_{a,b}}$ (μin./in.)	$\left(\frac{\sigma_\epsilon}{\bar{\epsilon}}\right)_{a,b}$ (%)	$\bar{\epsilon}_c$ (μin./in.)	$\pm\sigma_{\epsilon_c}$ (μin./in.)	$\left(\frac{\sigma_\epsilon}{\bar{\epsilon}}\right)_c$ (%)	$\bar{\epsilon}_d$ (μin./in.)	$\pm\sigma_{\epsilon_d}$ (μin./in.)	$\left(\frac{\sigma_\epsilon}{\bar{\epsilon}}\right)_d$ (%)
				Series I					
1	--	--	--	94	12	13.0	699	89	13.0
2	457	16	3.5	69	9	13.0	569	63	11.0
3	431	13	3.0	73	11	15.0	552	40	7.2
4	566	22	3.9	81	15	18.0	687	32	4.7
5	770	42	5.4	147	11	7.5	1016	72	7.1
6	957	52	5.4	164	15	9.1	1173	96	8.2
7	1332	91	6.8	257	16	6.2	1592	194	12.0
8	218	85	39.0	30T	9	30.0	411	57	14.0
				Series II					
1	184	18	9.8	27	15	55.0	224	44	20.0
2	405	10	2.5	65	10	15.0	405	39	9.6
3	516	45	8.7	72	12	17.0	625	61	9.6
4	807	90	11.0	155	14	9.0	996	128	13.0
5	925	77	8.3	140	22	16.0	1022	112	11.0
6	1146	49	3.3	218	13	6.0	1443	50	3.5
7	1090	19	1.7	174	8	4.6	1460	38	2.6
8	1557	139	8.9	275	44	16.0	2020	39	1.9

Table 10. Average slopes of dynamic response curves

Response measured	Series I (H/D = 1.0)	Series II (H/D = 2.0)	Percent reduction, H/D = 1.0 to H/D = 2.0
$\overline{\epsilon}_{a,b}$	7.6 $\frac{\mu in./in.}{psi}$	6.2 $\frac{\mu in./in.}{psi}$	18
$\overline{\epsilon}_{c}$	1.3 $\frac{\mu in./in.}{psi}$	1.2 $\frac{\mu in./in.}{psi}$	8
$\overline{\epsilon}_{d}$	9.4 $\frac{\mu in./in.}{psi}$	8.4 $\frac{\mu in./in.}{psi}$	11
$\overline{\Delta/D}$	5.0×10^{-5} $\frac{in./in.}{psi}$	4.6×10^{-5} $\frac{in./in.}{psi}$	8

FIGURES

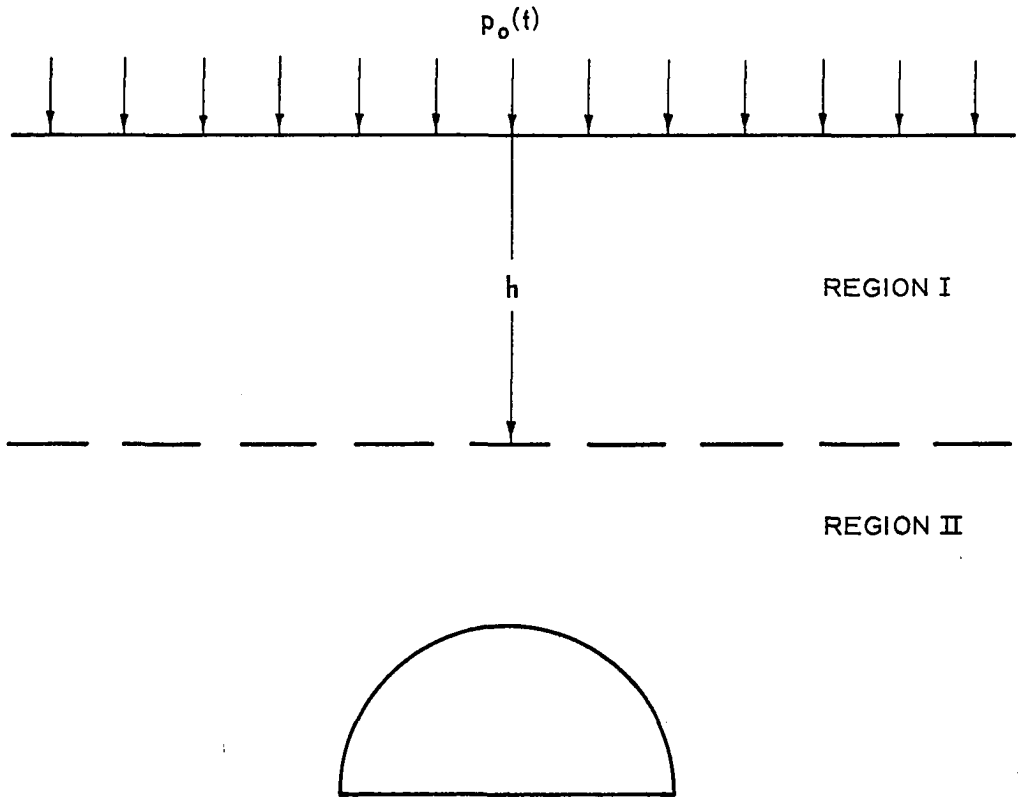

Figure 1. Representative soil-structure complex

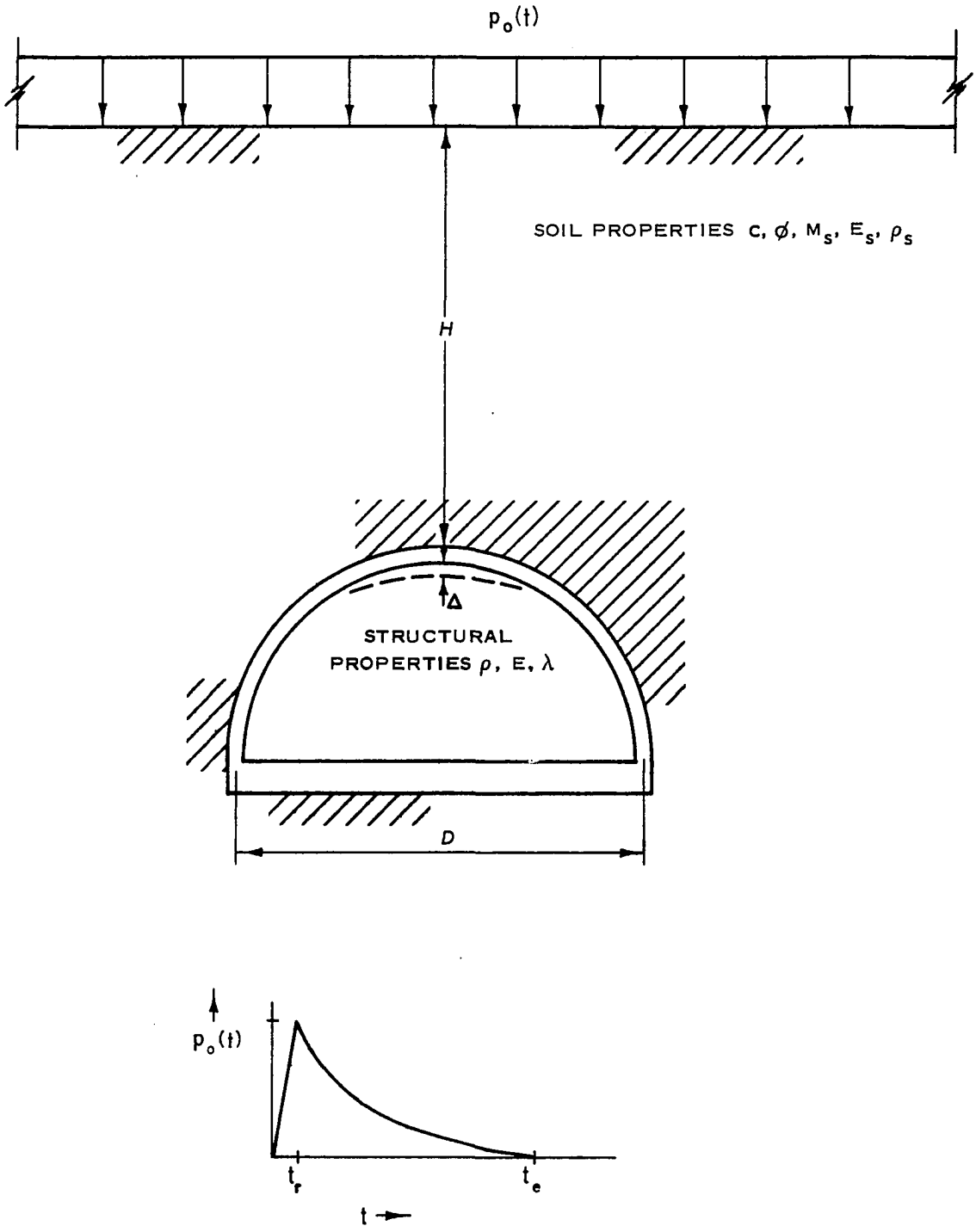

Figure 2. General sketch of system

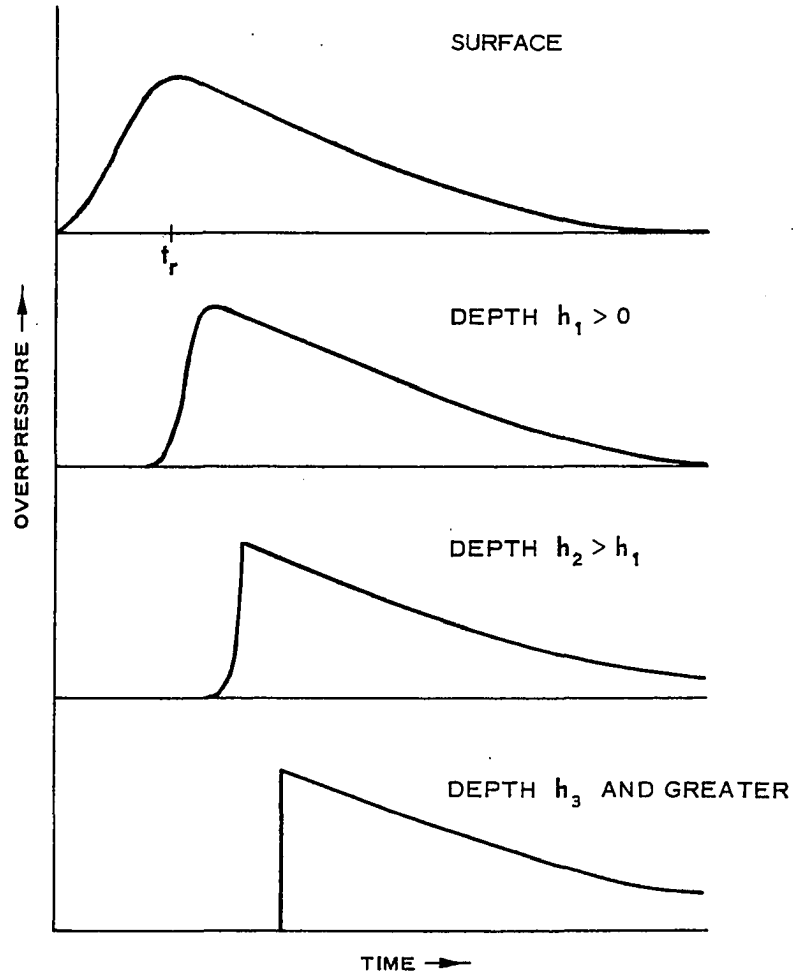

Figure 3. Schematic representation of "shocking up" in dense dry sand as evidenced by overpressure-time relation

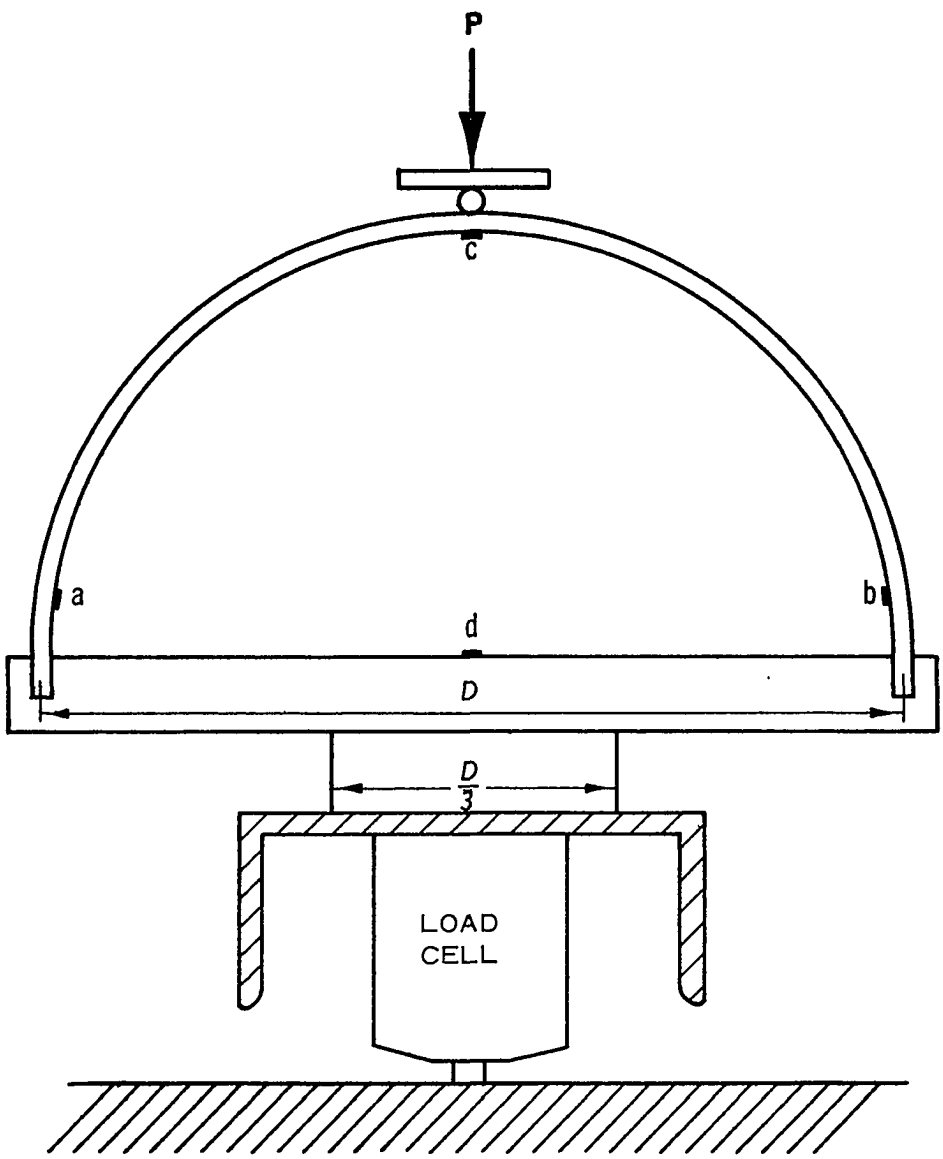

Figure 4. Preliminary bench test configuration

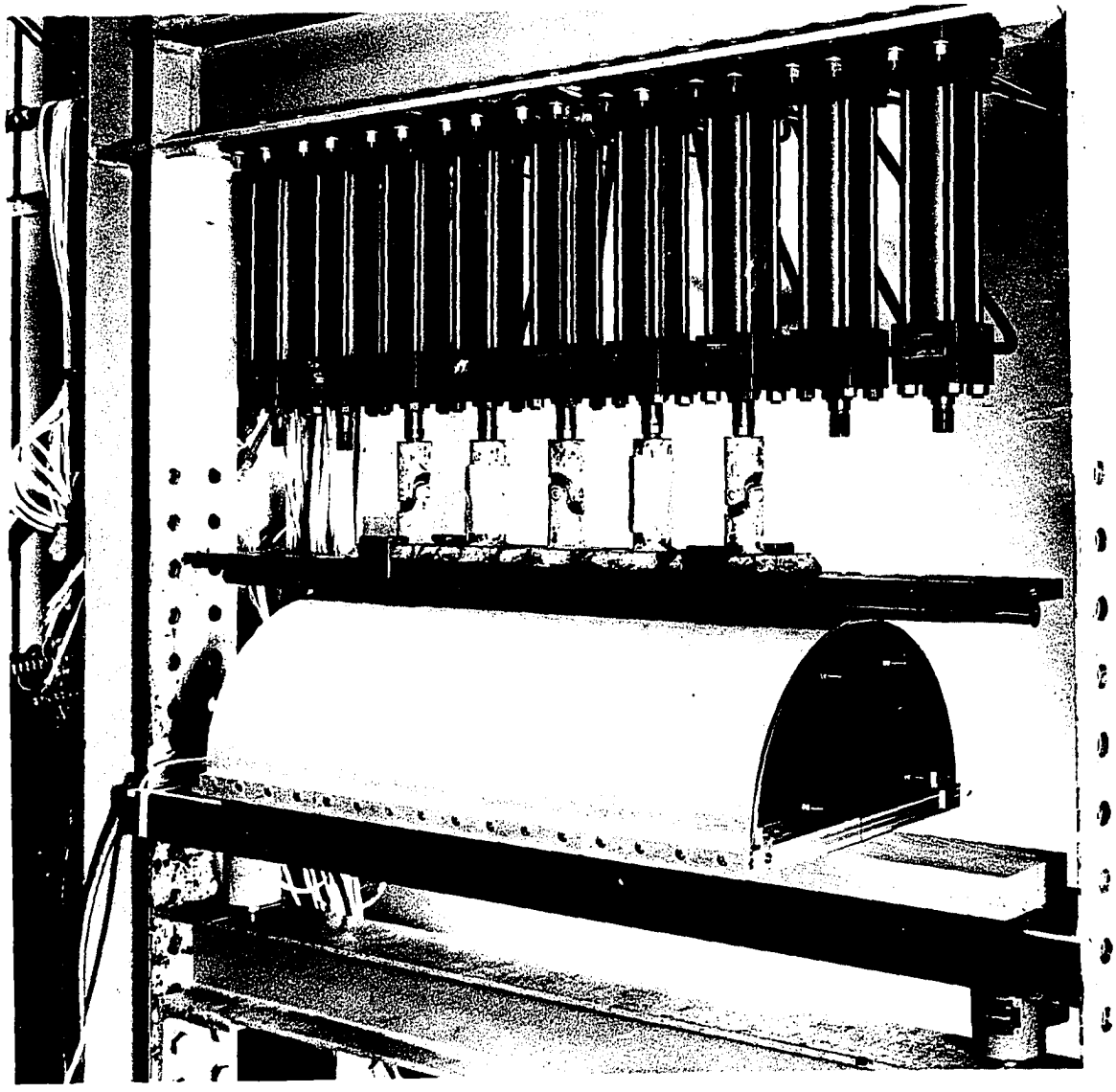

Figure 5. Preliminary bench test apparatus

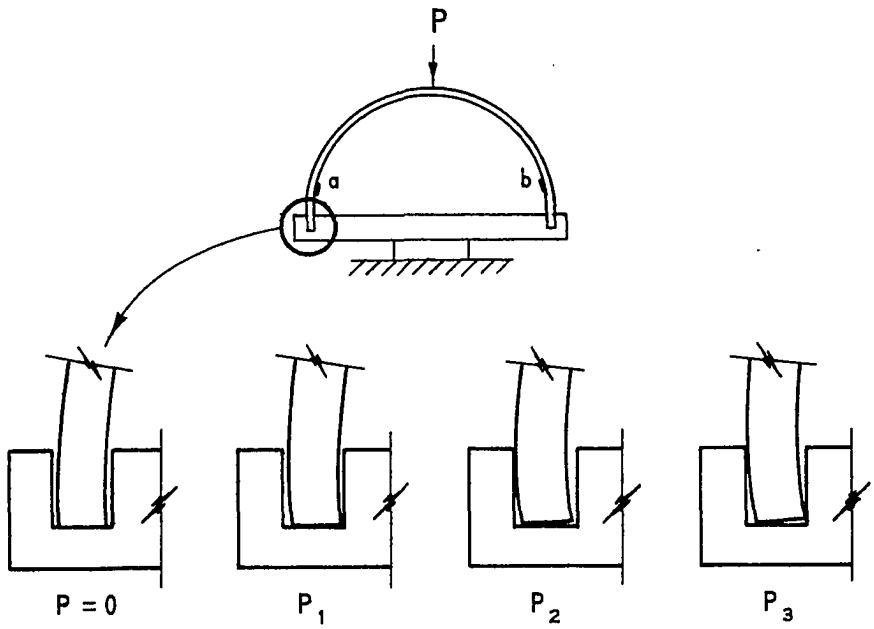

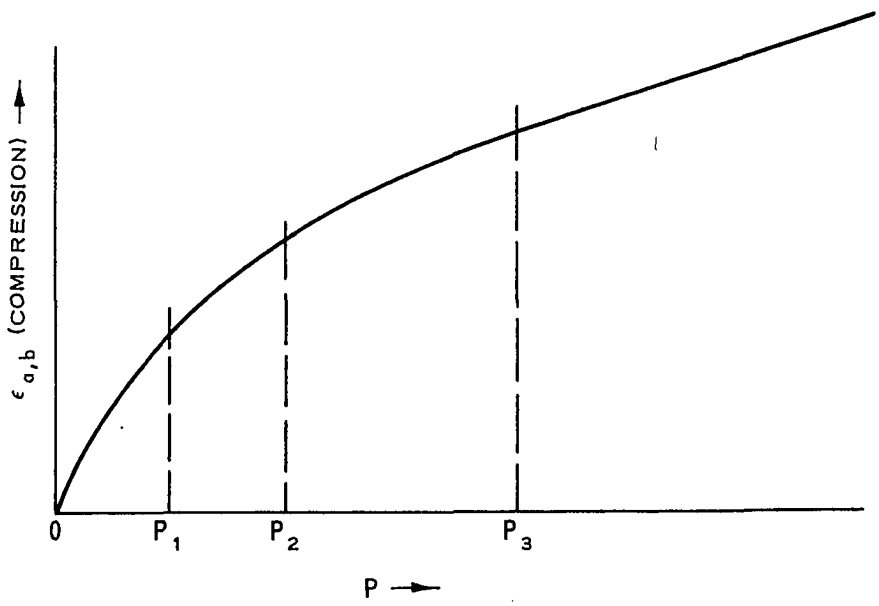

Figure 6. Effect of joint rotation under increasing load

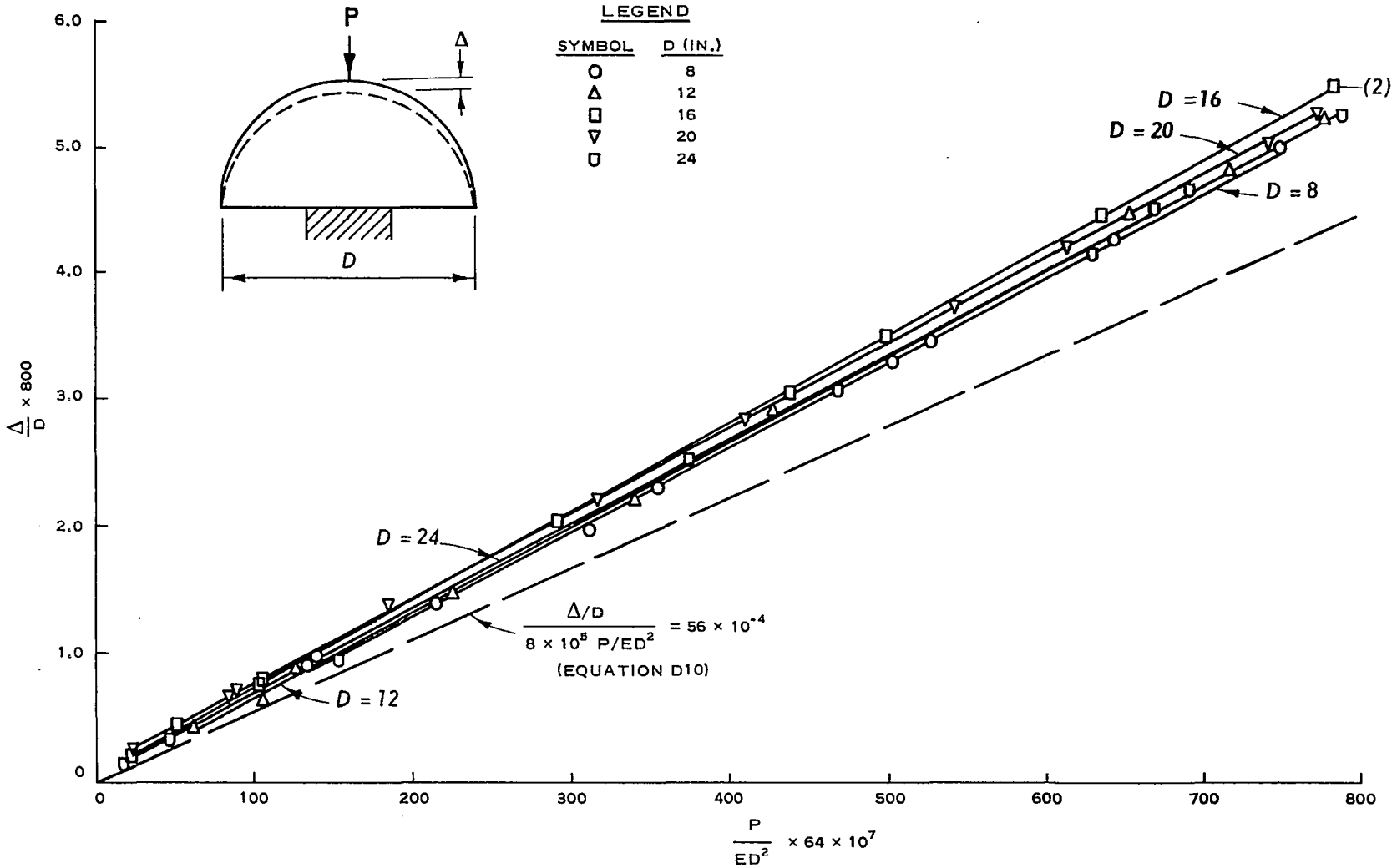

Figure 7. Dimensionless load-deflection curves for five arches

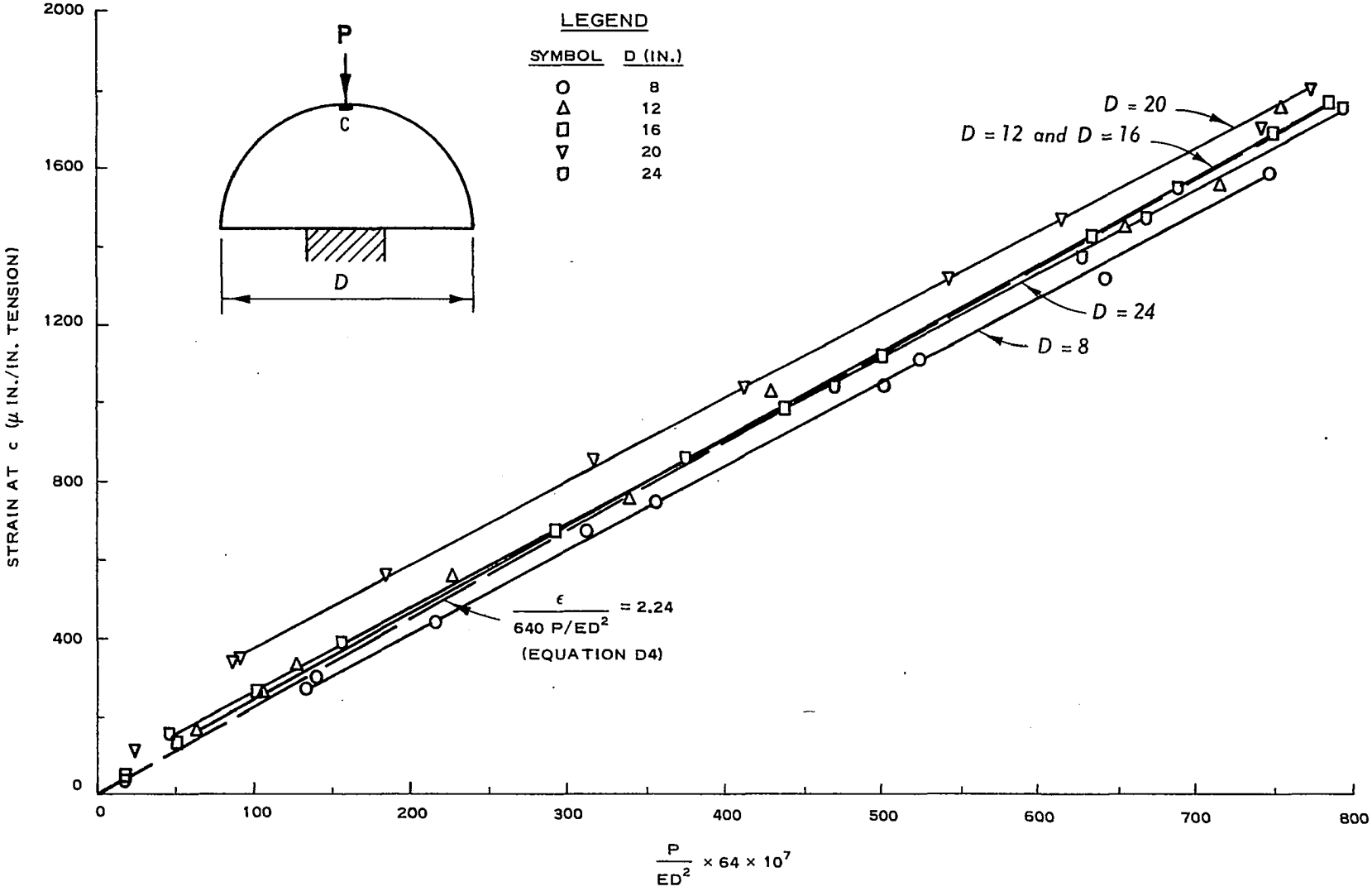

Figure 8. Strain at c versus dimensionless load for five arches

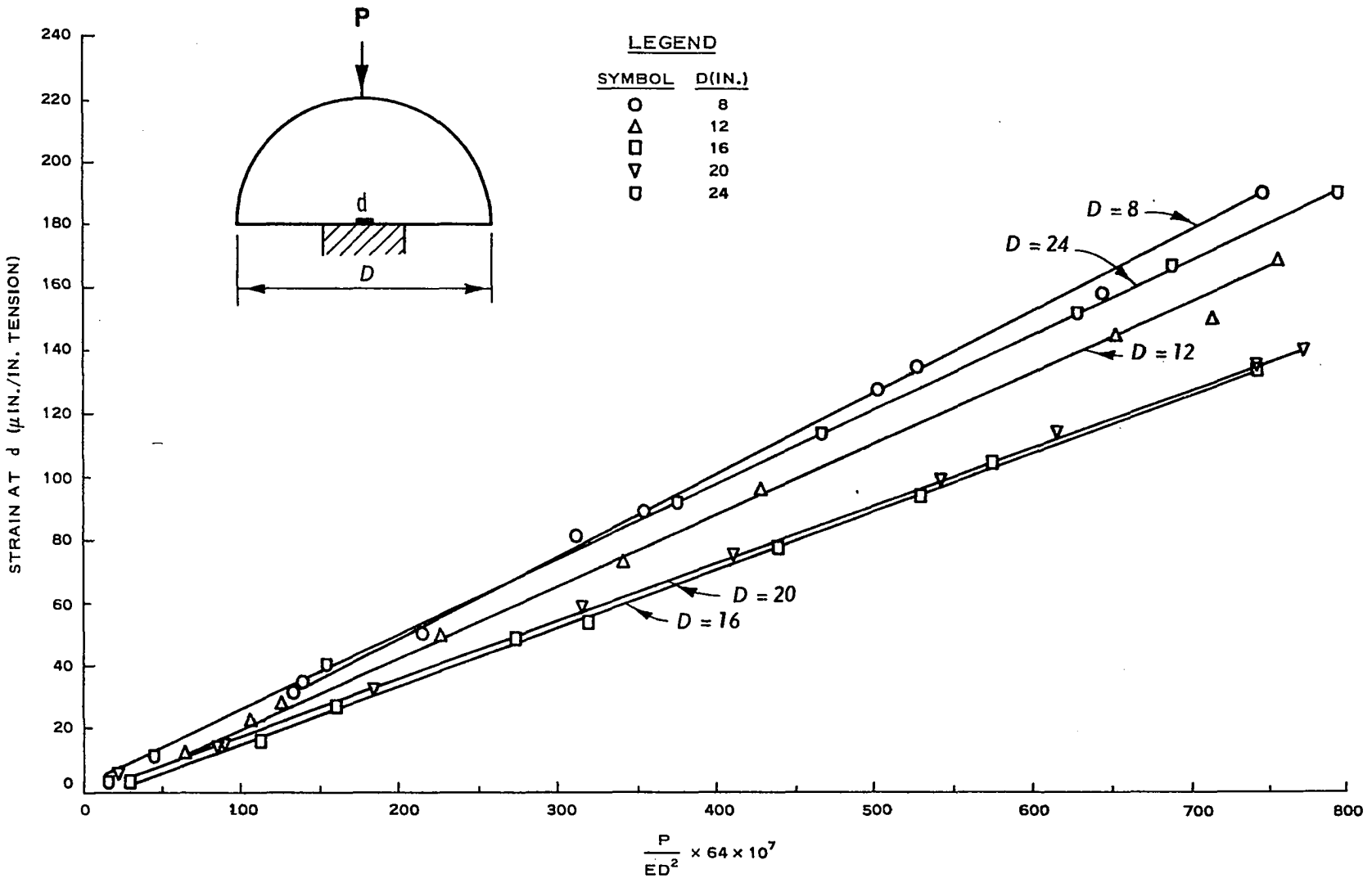

Figure 9. Strain at d versus dimensionless load for five arches

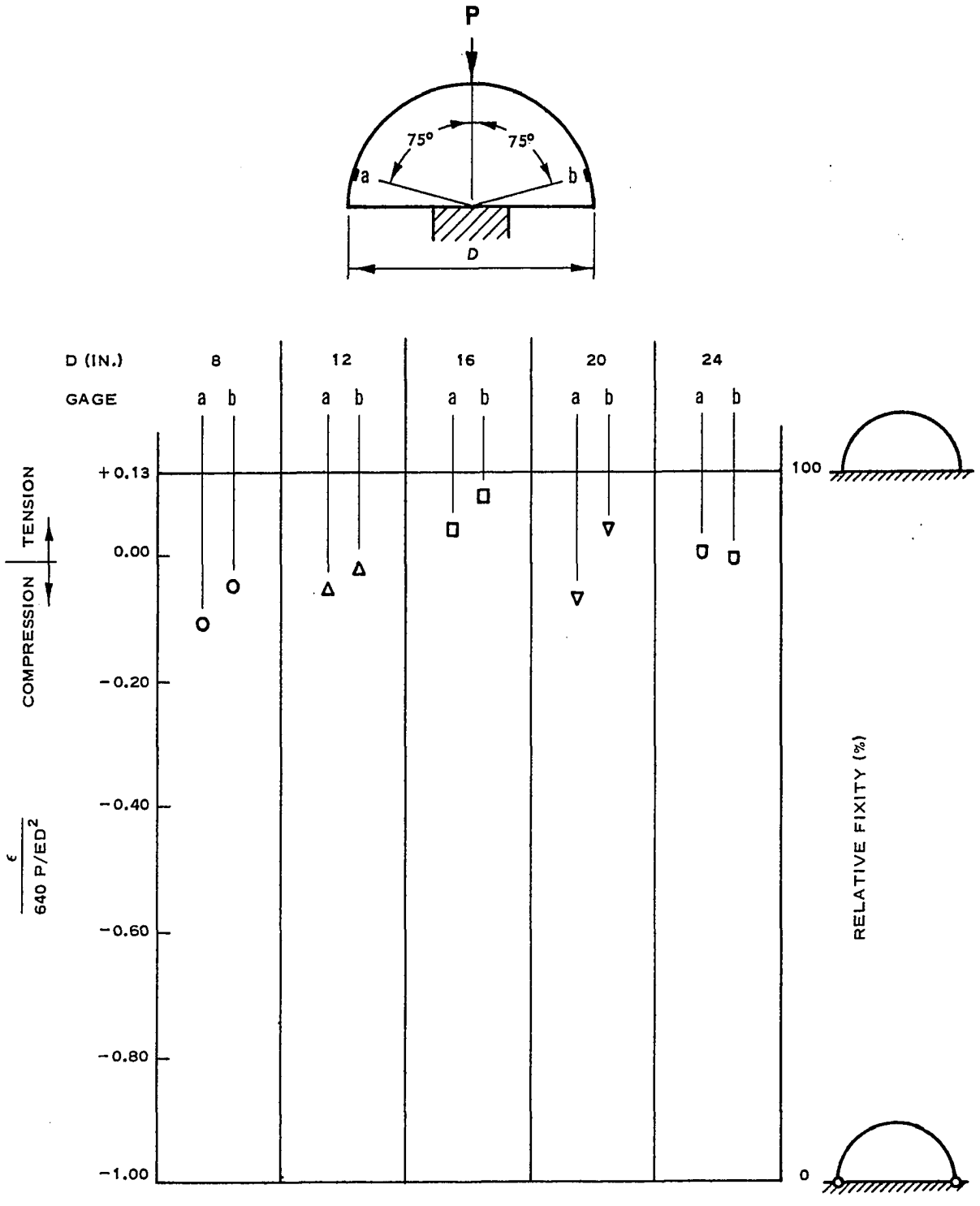

Figure 10. Strains at a and b compared with end fixity conditions

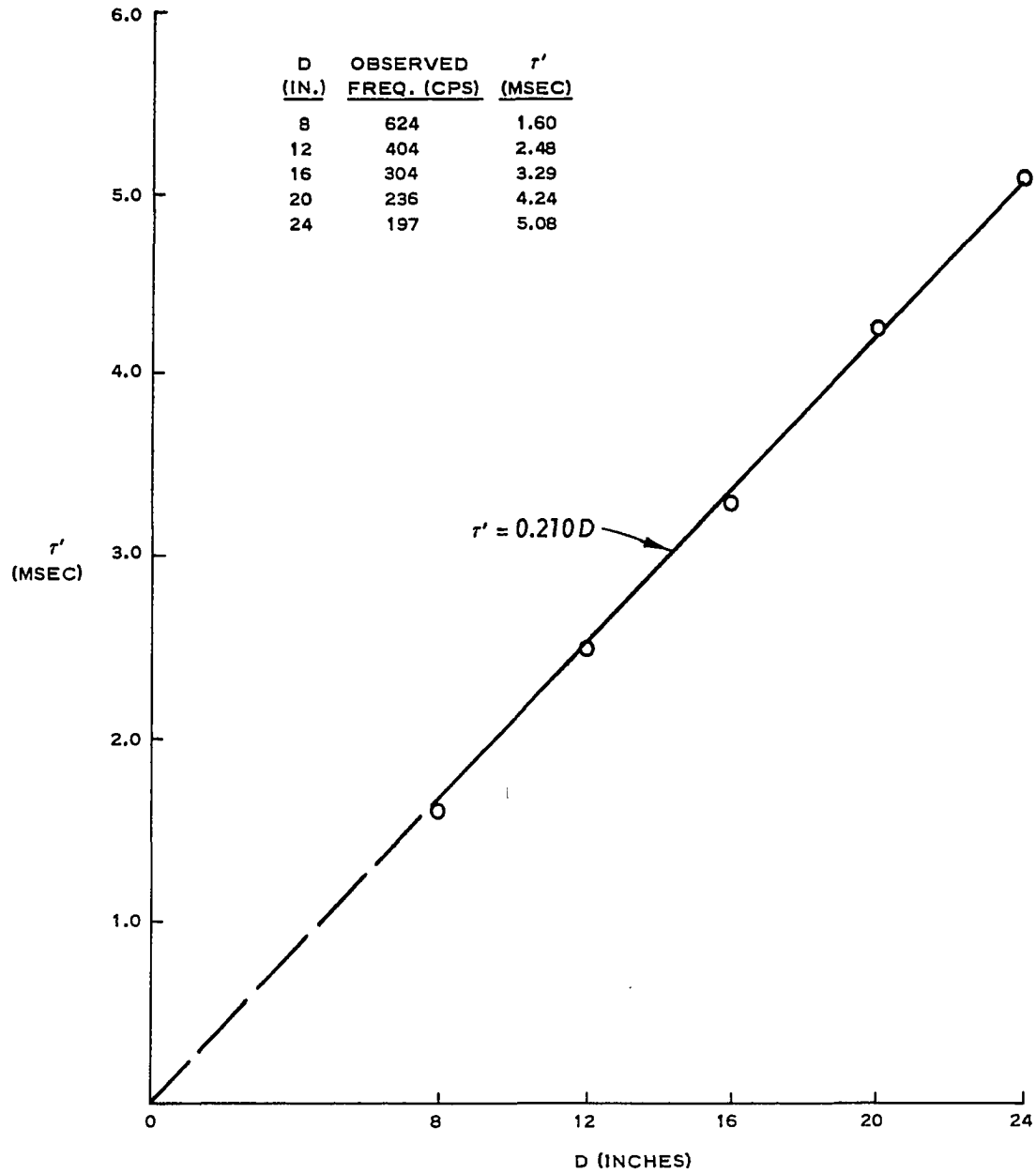

Figure 11. Natural period τ' versus arch diameter

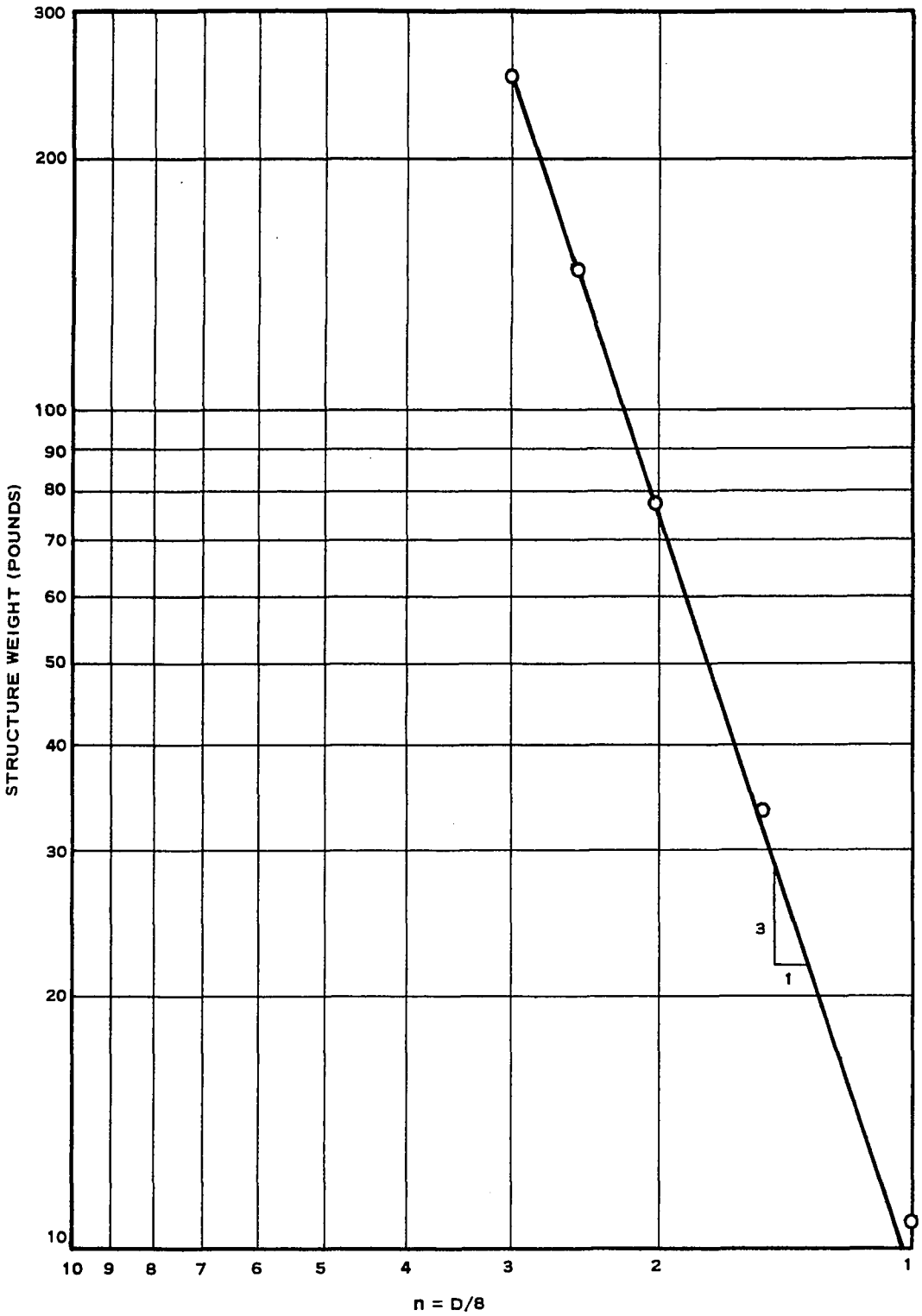

Figure 12. Weight of structure versus length scale

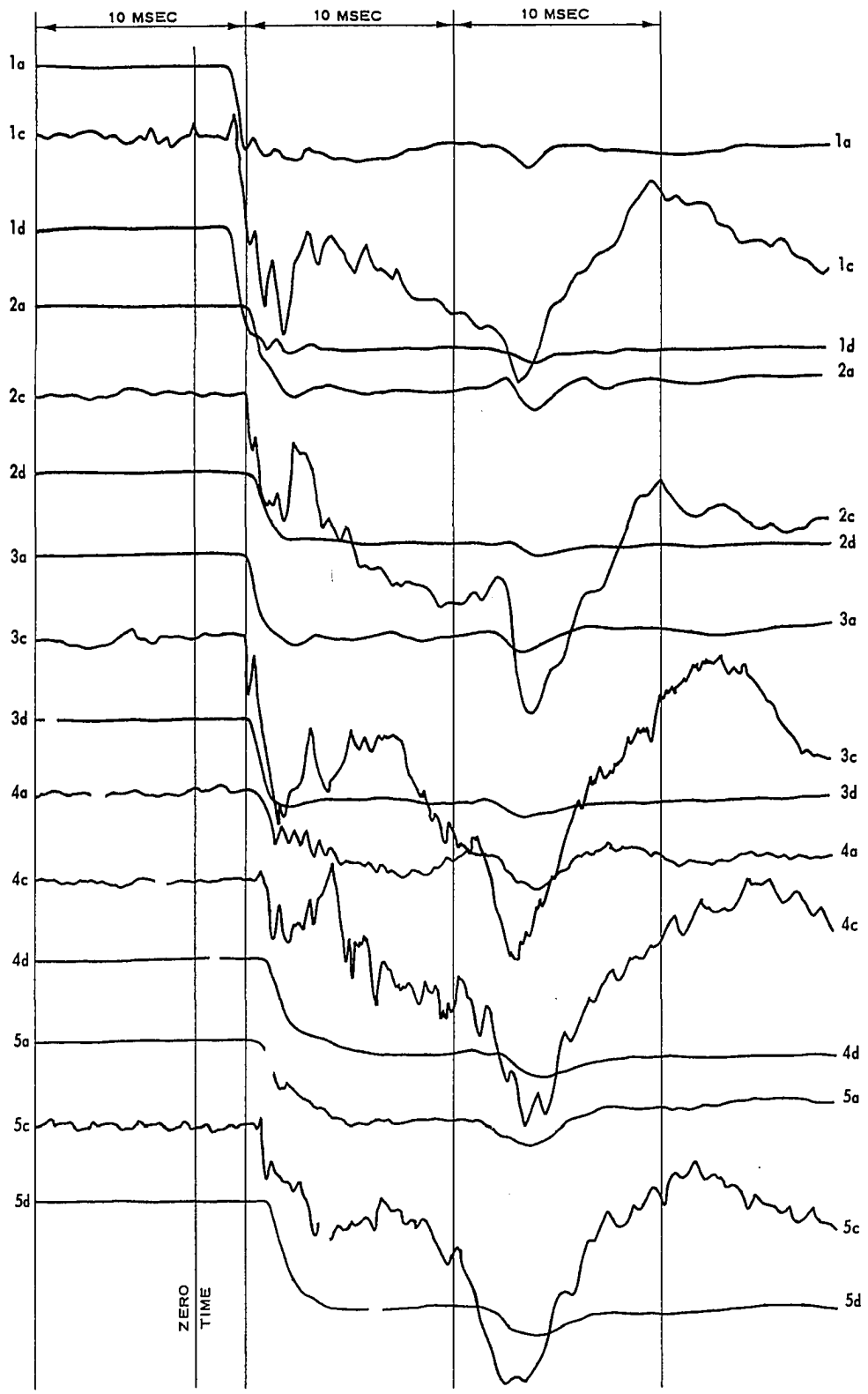

Figure 13. Record of strain gages a, c, and d for five arches; shot 4, Series I

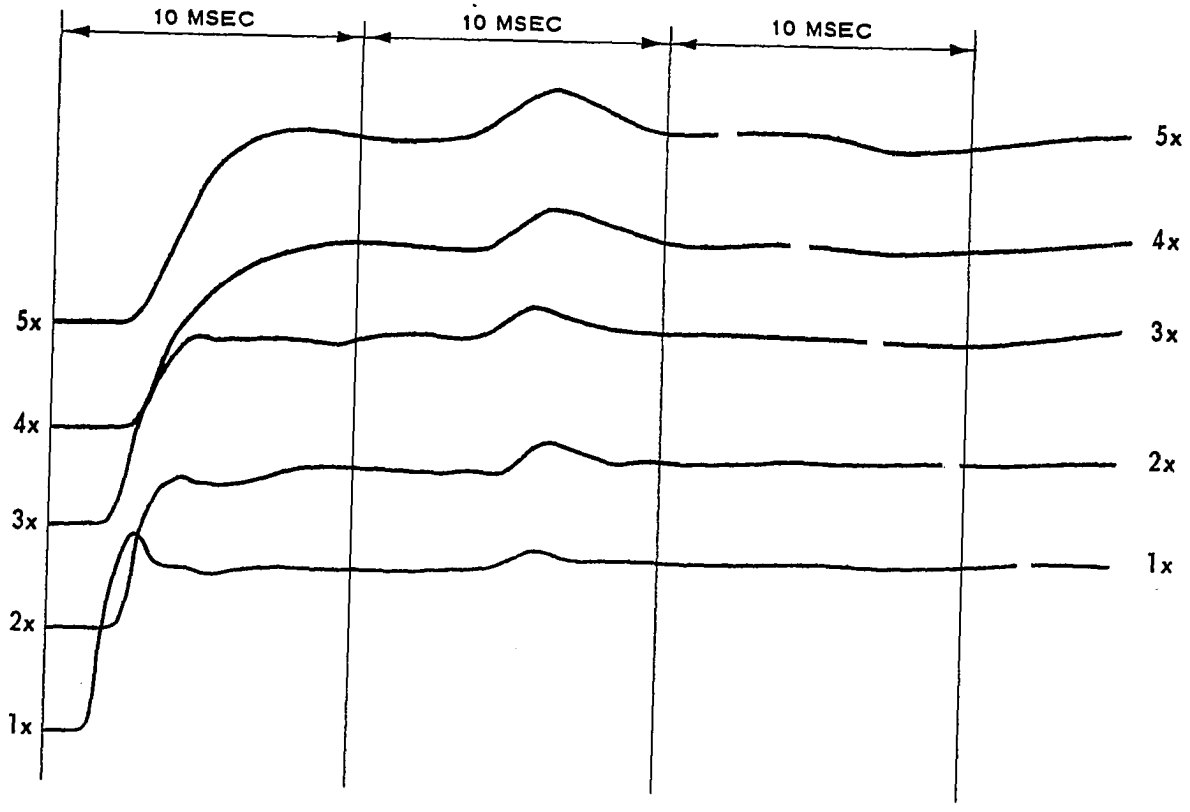

Figure 14. Record of deflection for five arches; shot 4, Series I

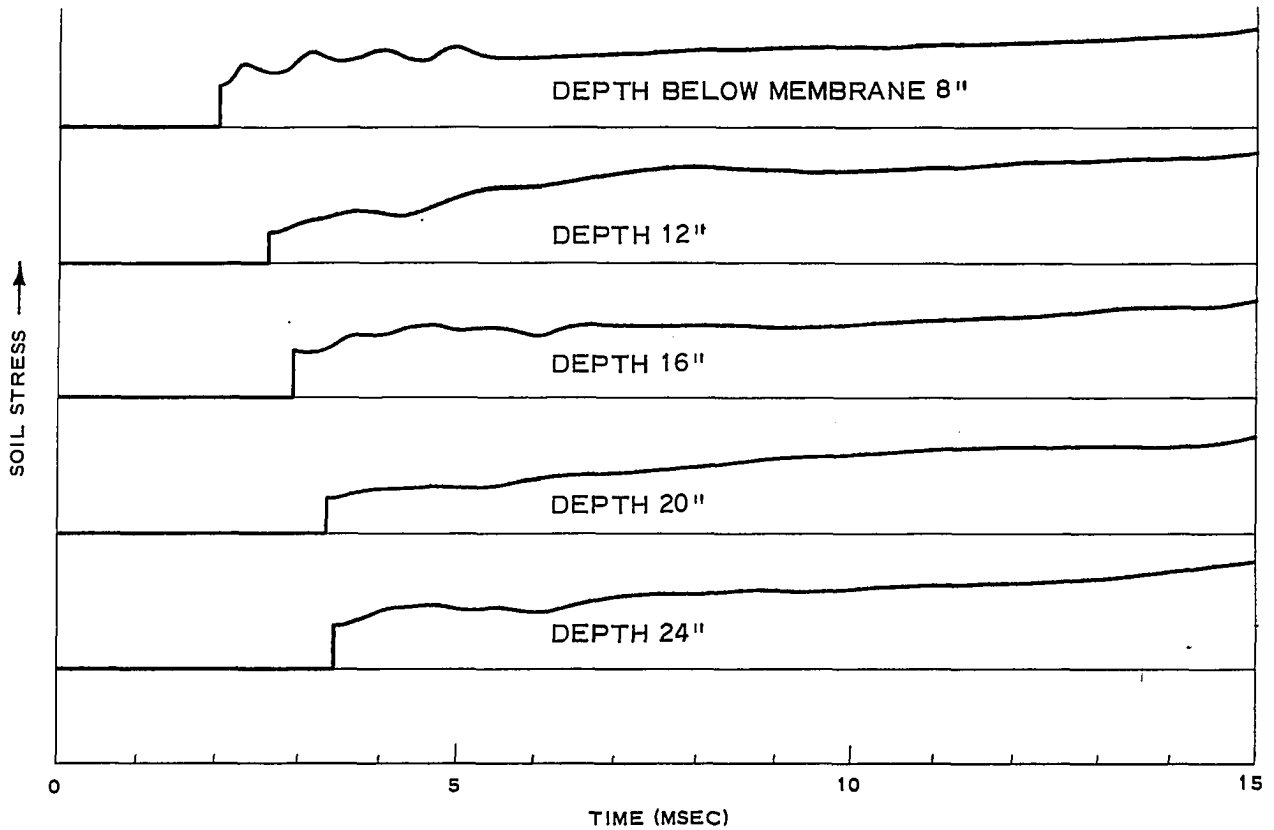

a. OSCILLOGRAPH RECORDS

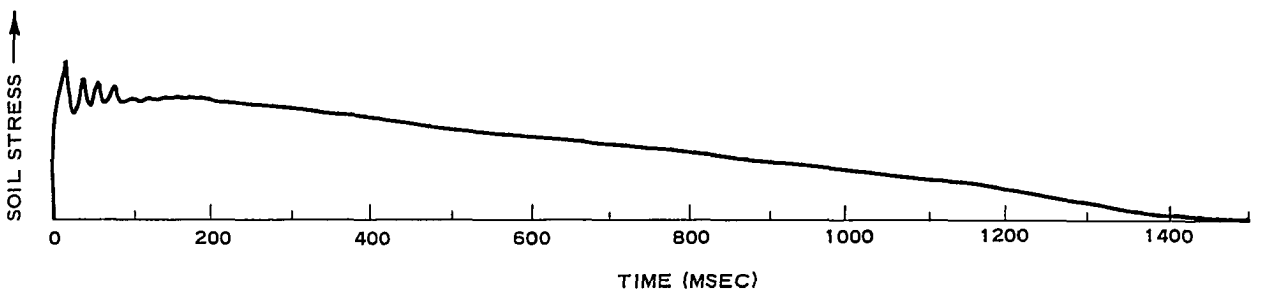

b. CONDENSED RECORD FROM MAGNETIC TAPE, DEPTH 24 IN.

Figure 15. Typical records, buried soil pressure cells (shot 4, Series I; amplitudes not to scale)

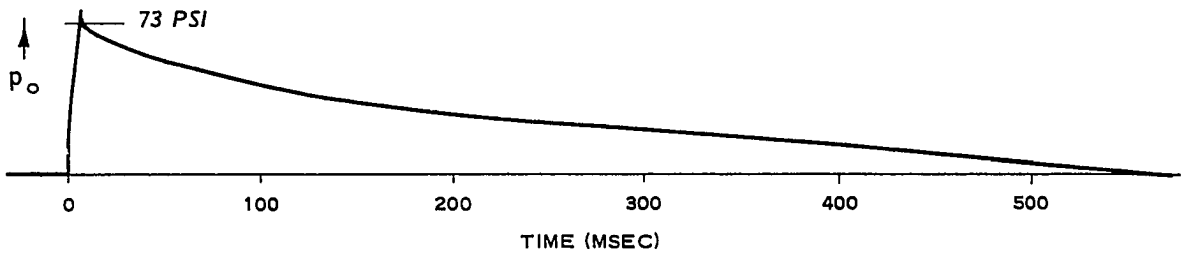

a. CONDENSED RECORD FROM TAPE

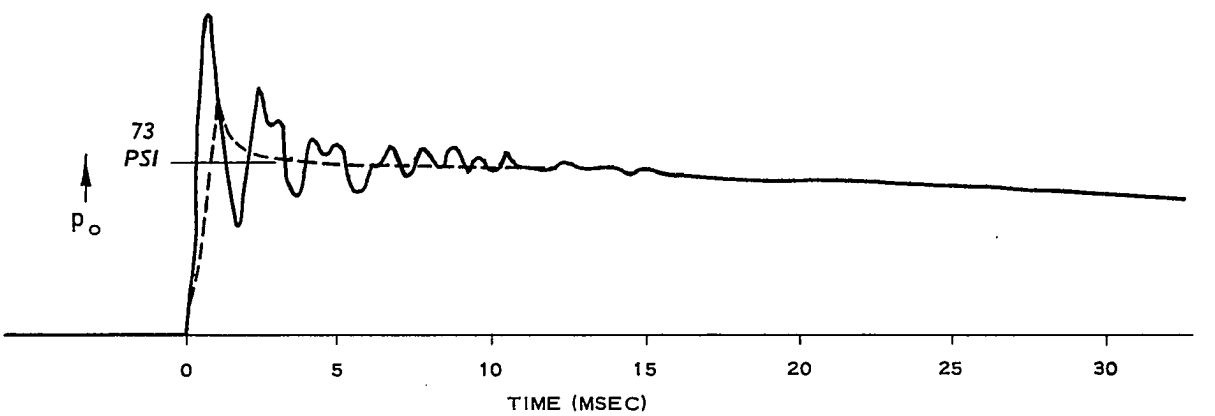

b. RECORD FROM OSCILLOGRAPH

Figure 16. Typical air overpressure records, shot 4, Series I

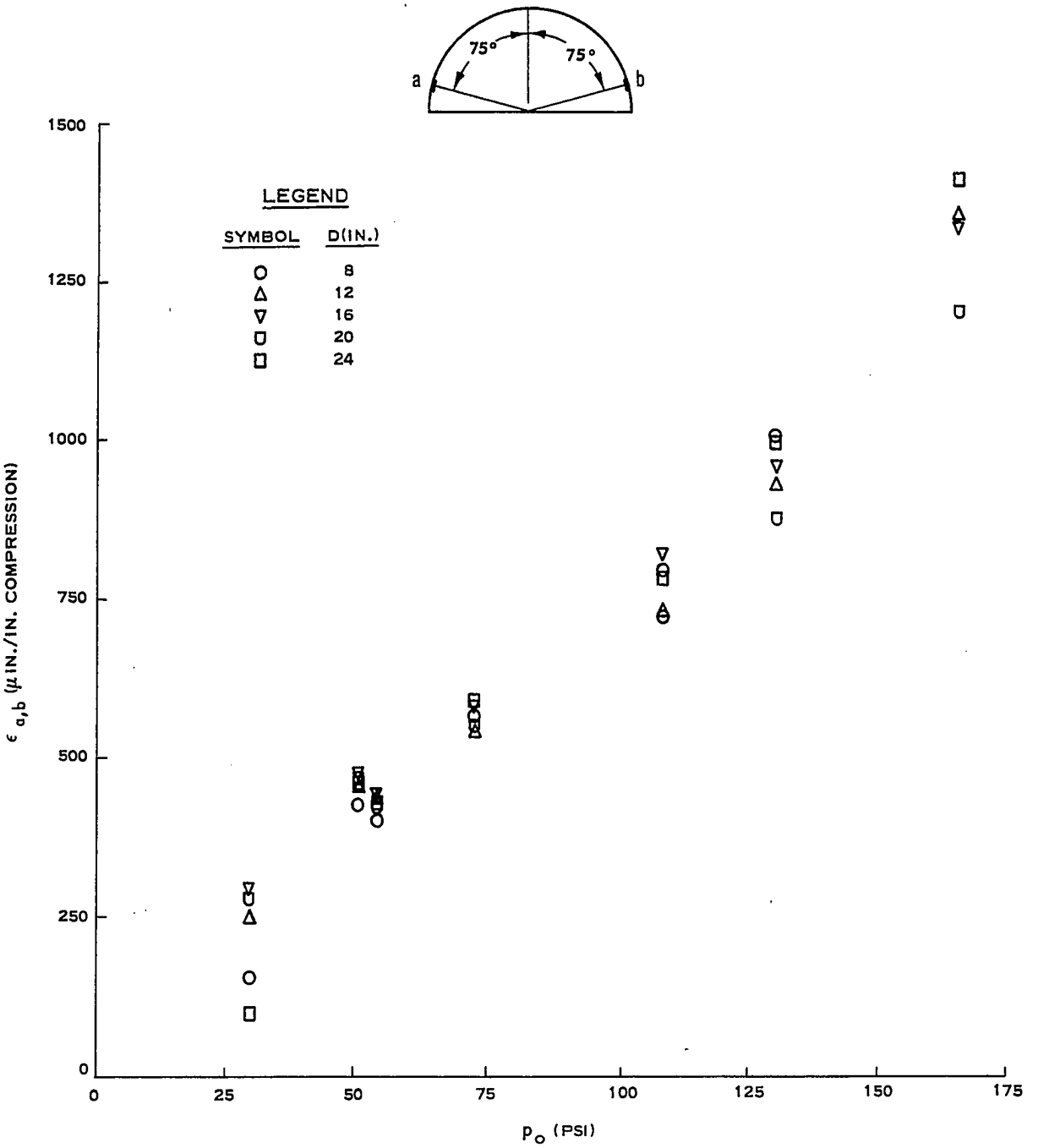

Figure 17. Average peak strain at $\theta = 75^{\circ}$ versus peak surface overpressure, Series I

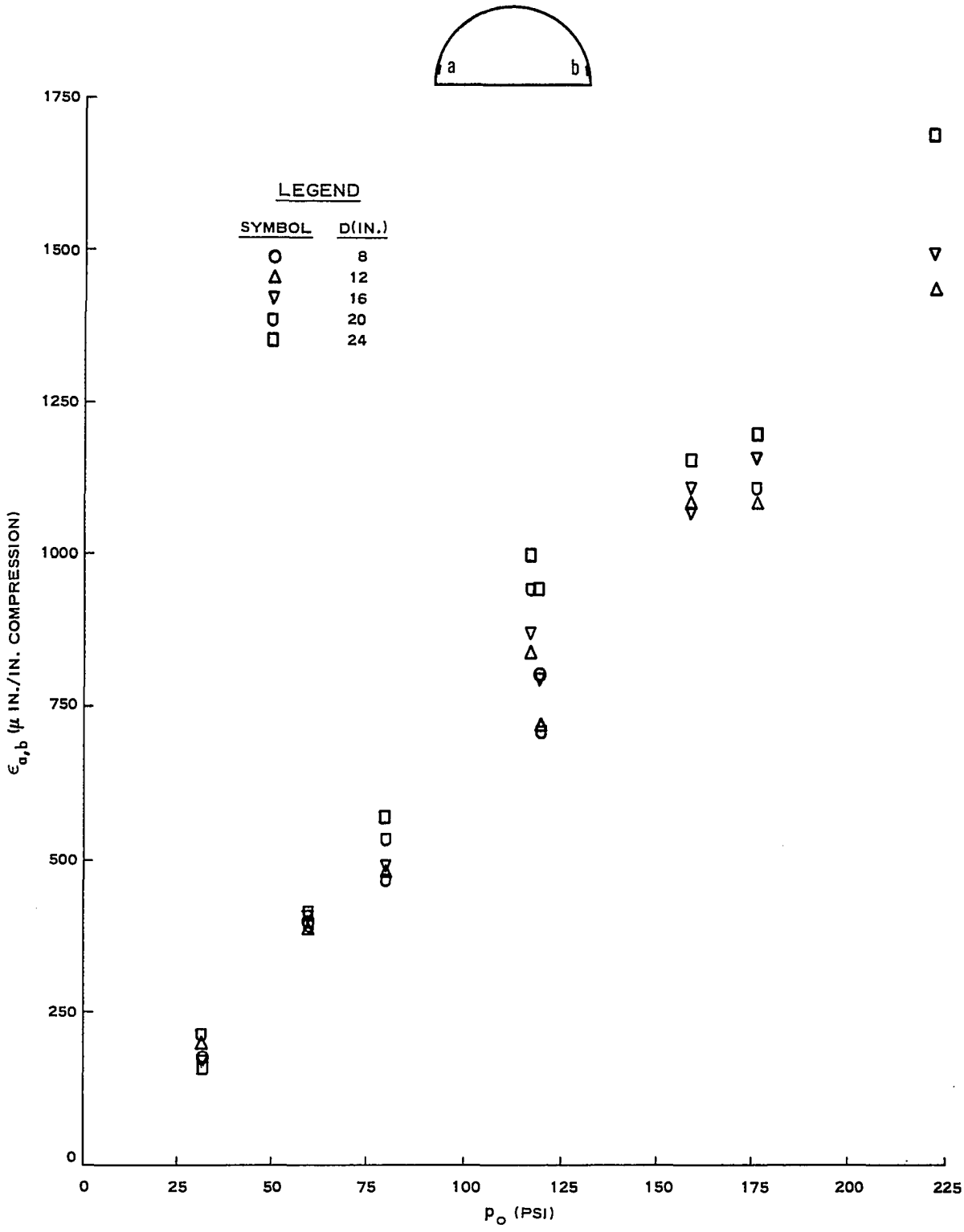

Figure 18. Average peak strain at a and b versus peak surface overpressure, Series II

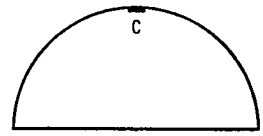

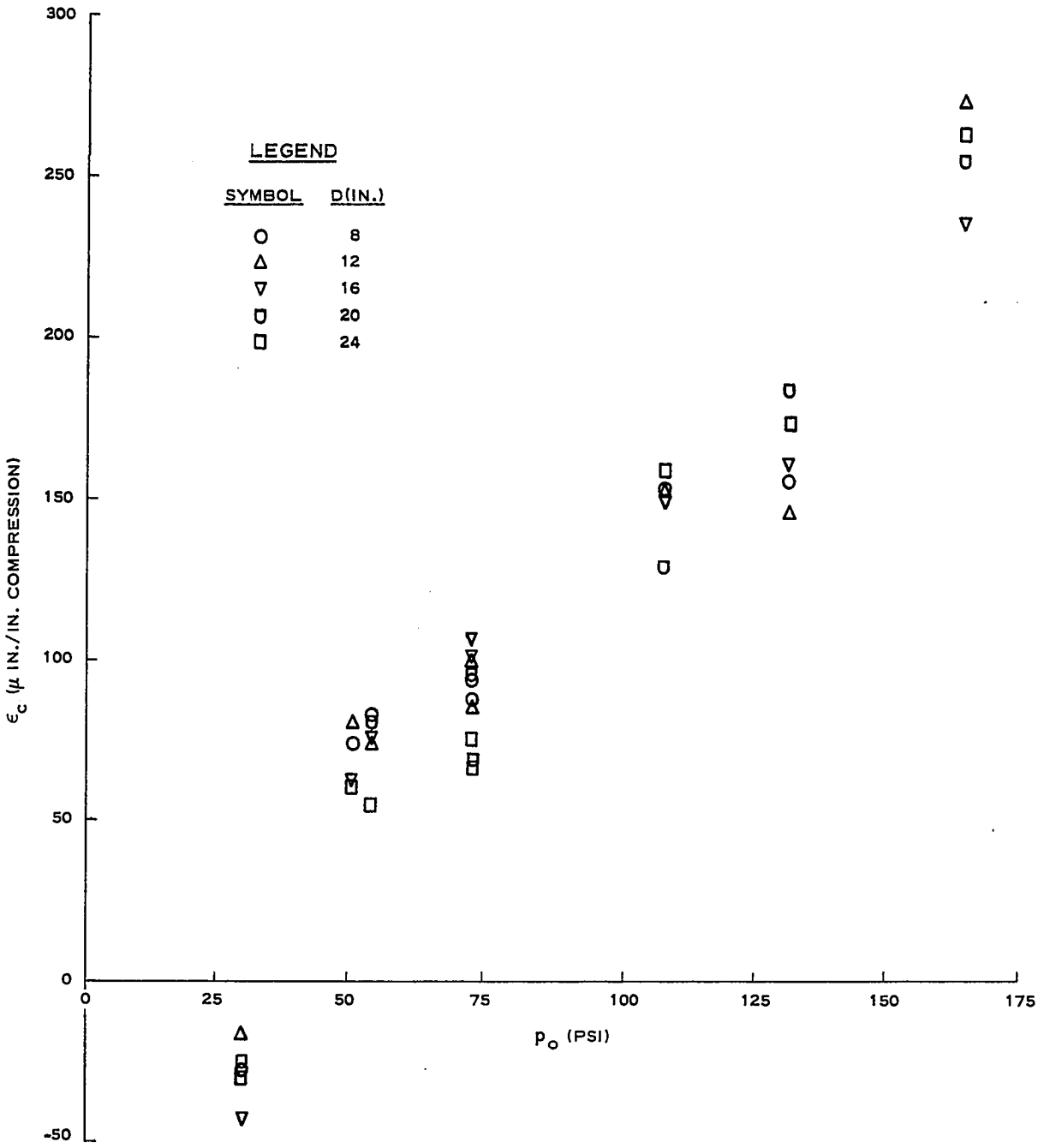

Figure 19. Peak strain at crown versus peak surface overpressure, Series I

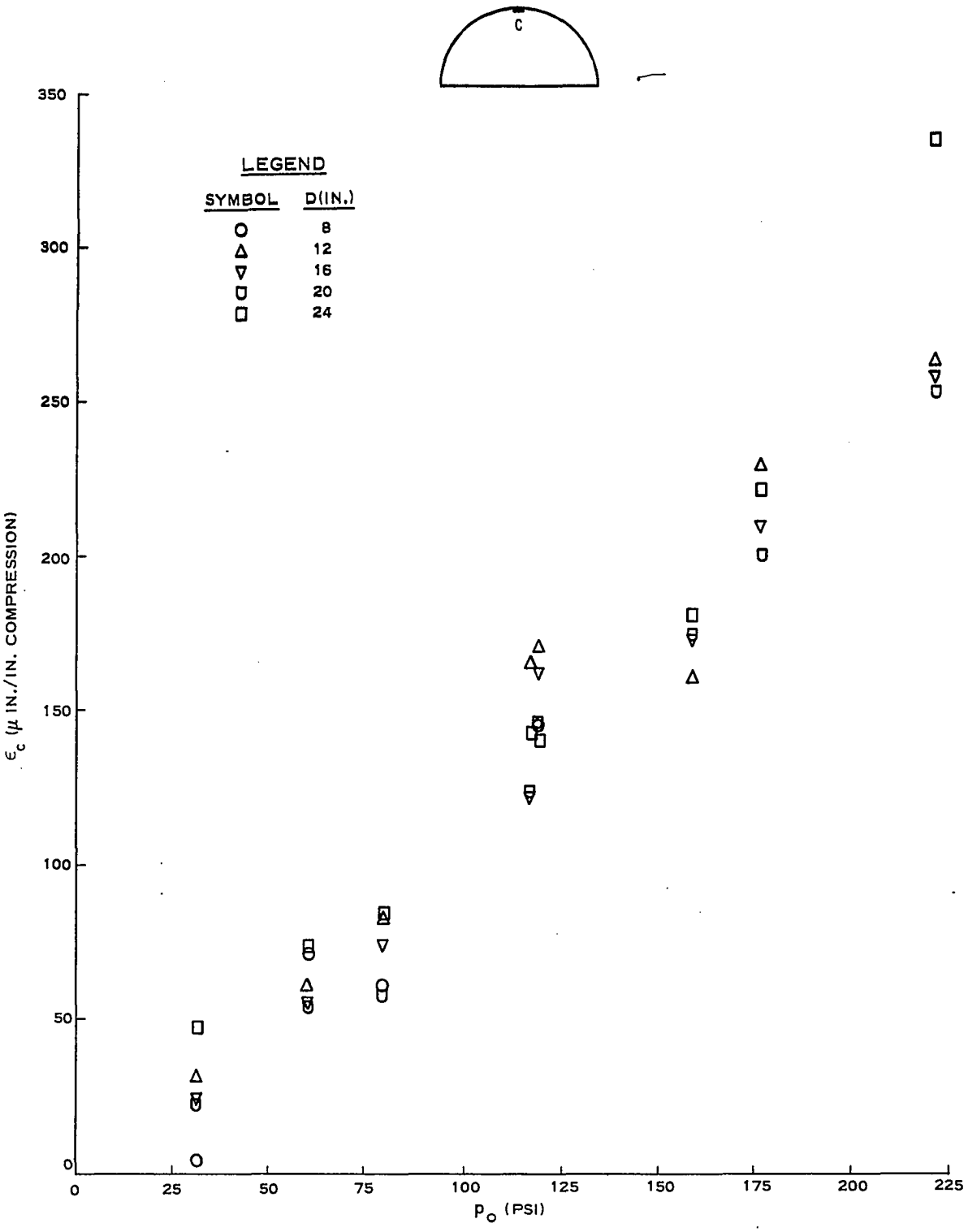

Figure 20. Peak strain at crown versus peak surface overpressure, Series II

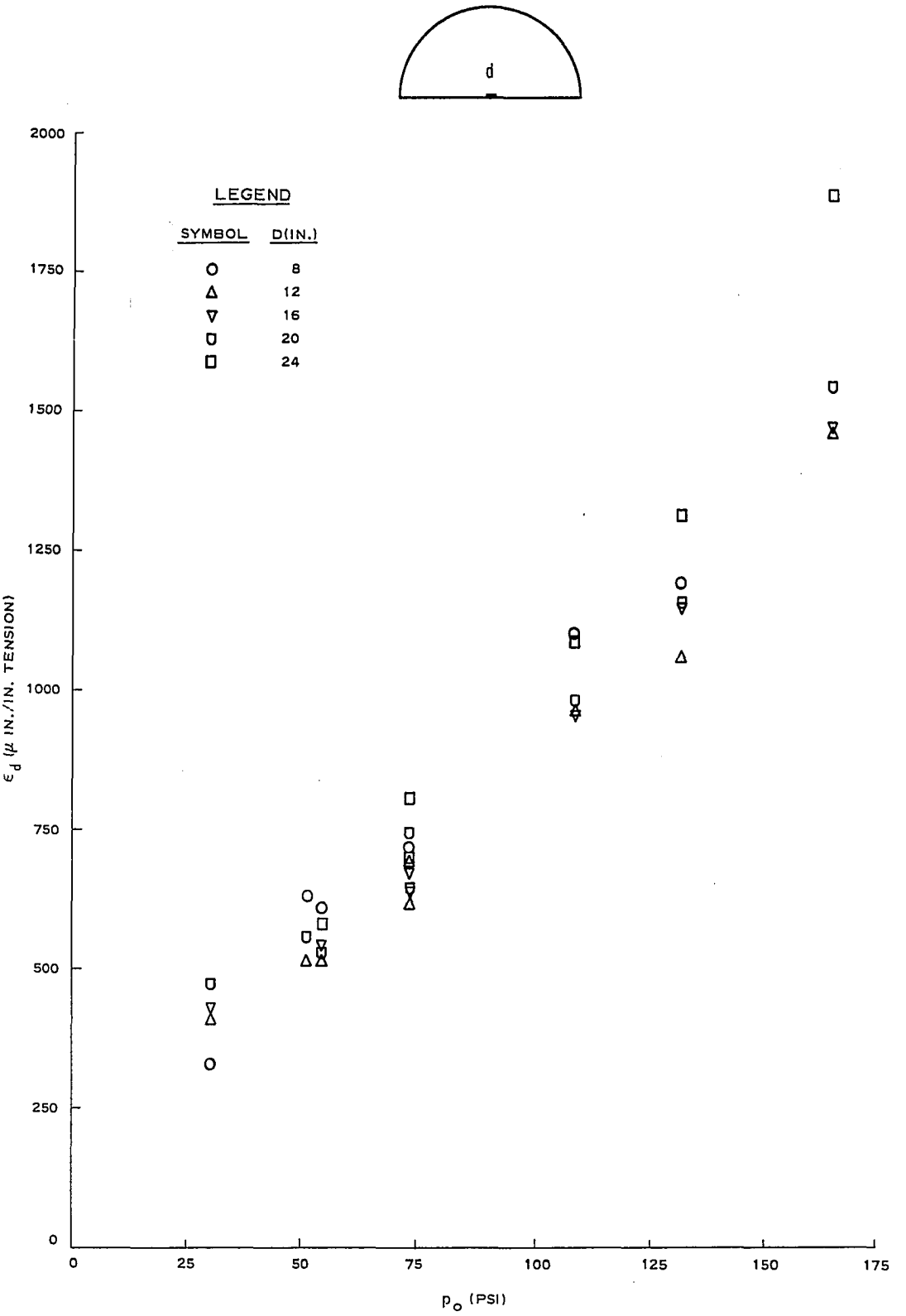

Figure 21. Peak strain in floor versus peak surface overpressure, Series I

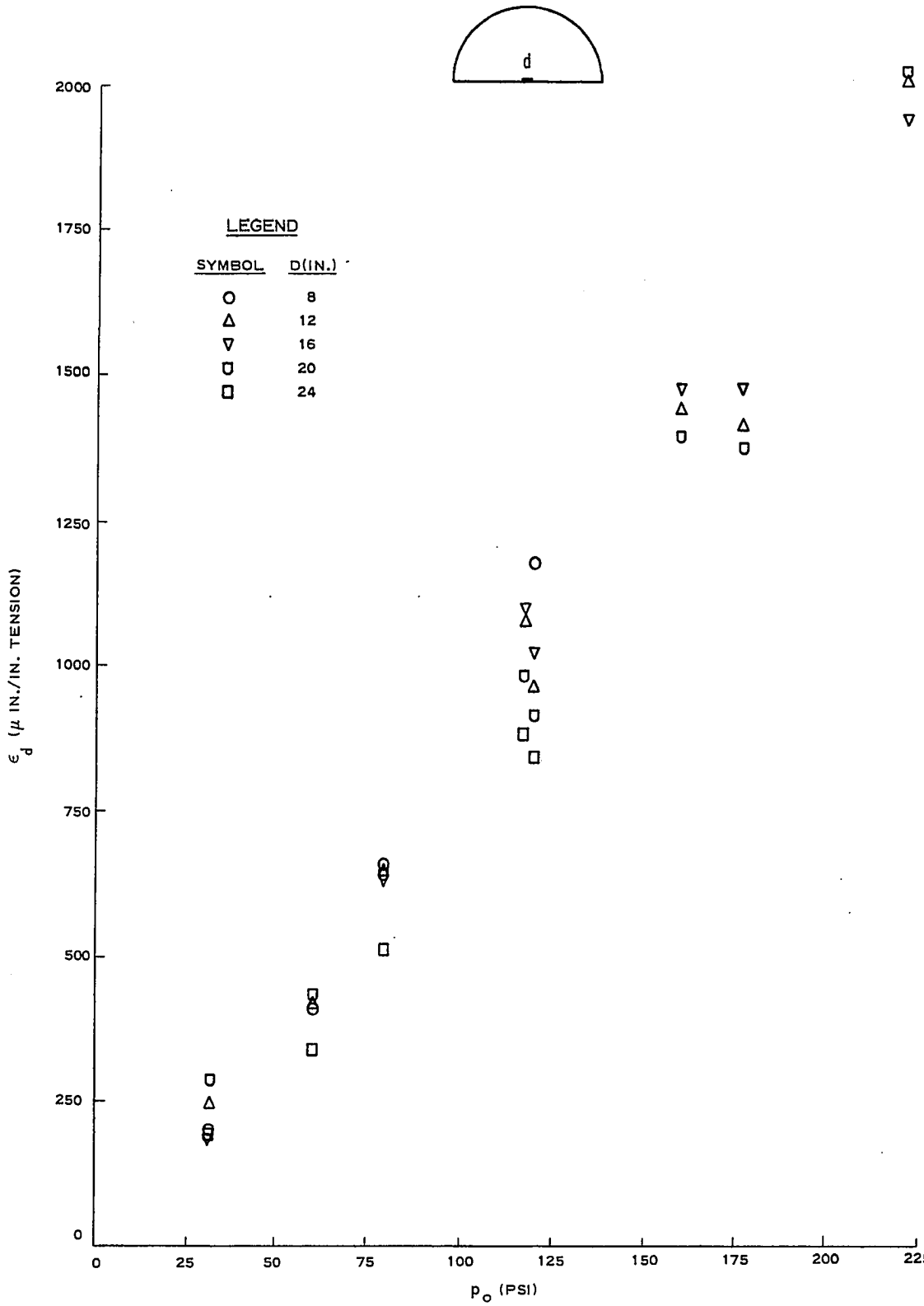

Figure 22. Peak strain in floor versus peak surface overpressure, Series II

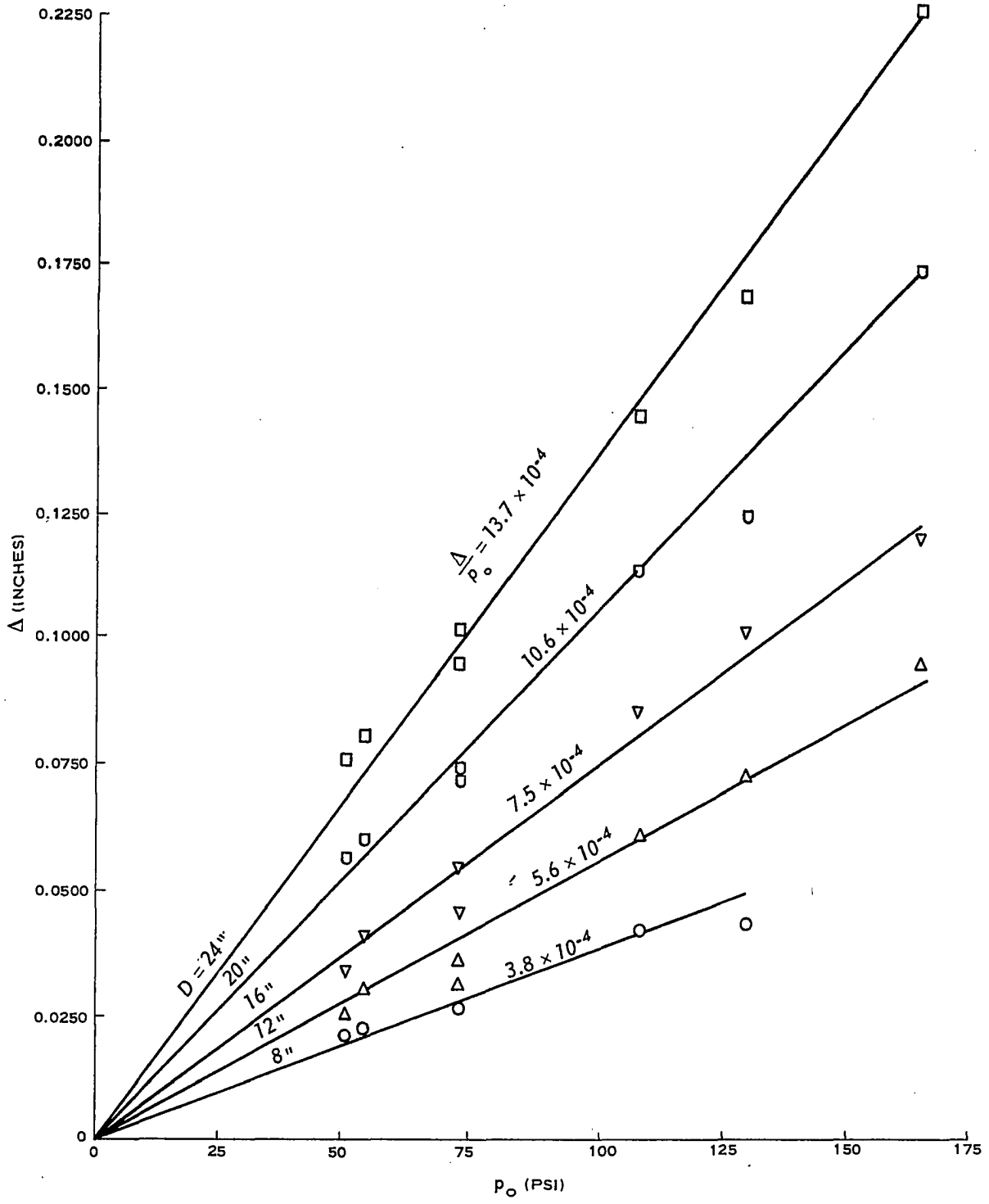

Figure 23. Peak deflection versus peak surface overpressure, Series I

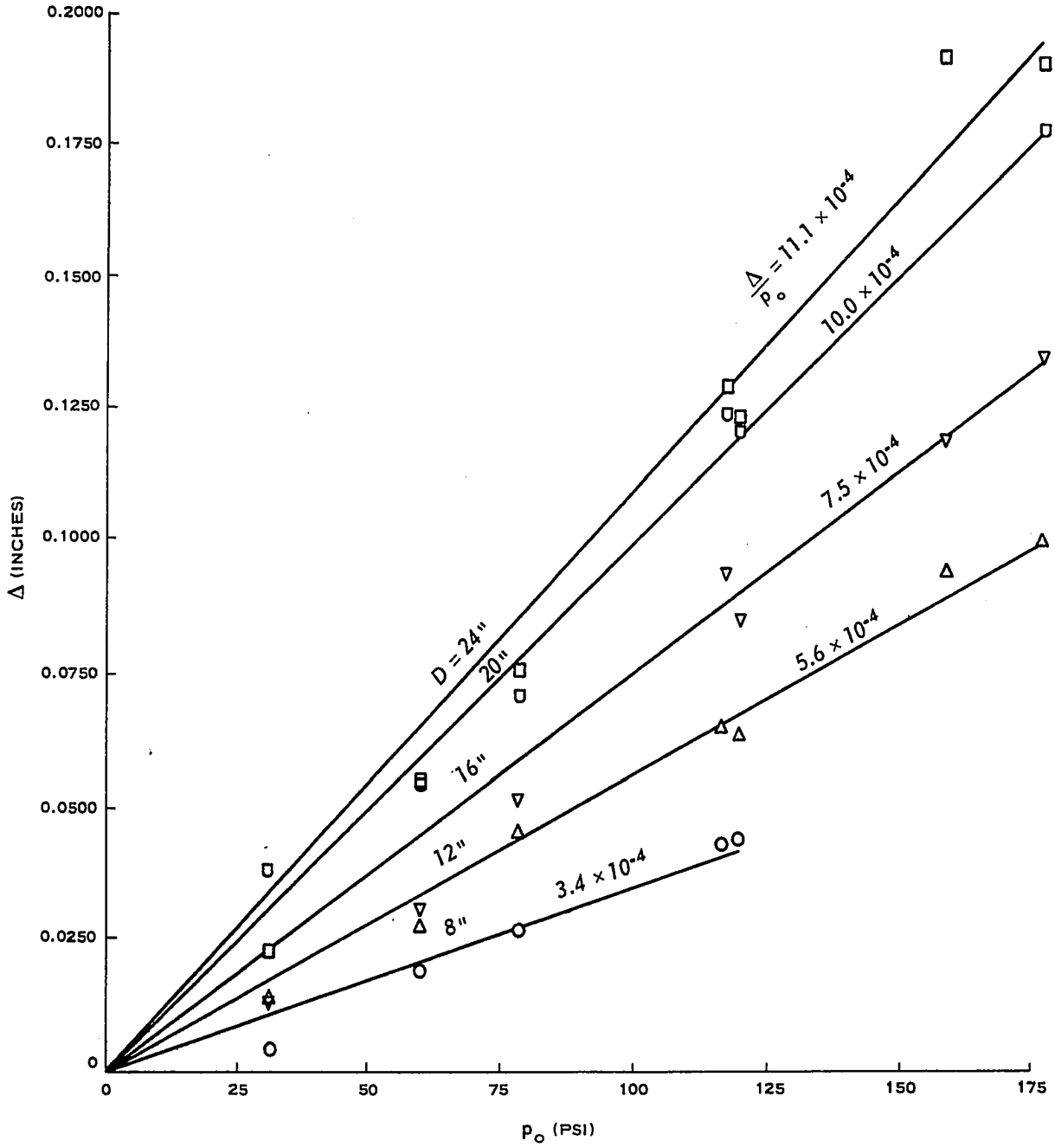

Figure 24. Peak deflection versus peak surface overpressure, Series II

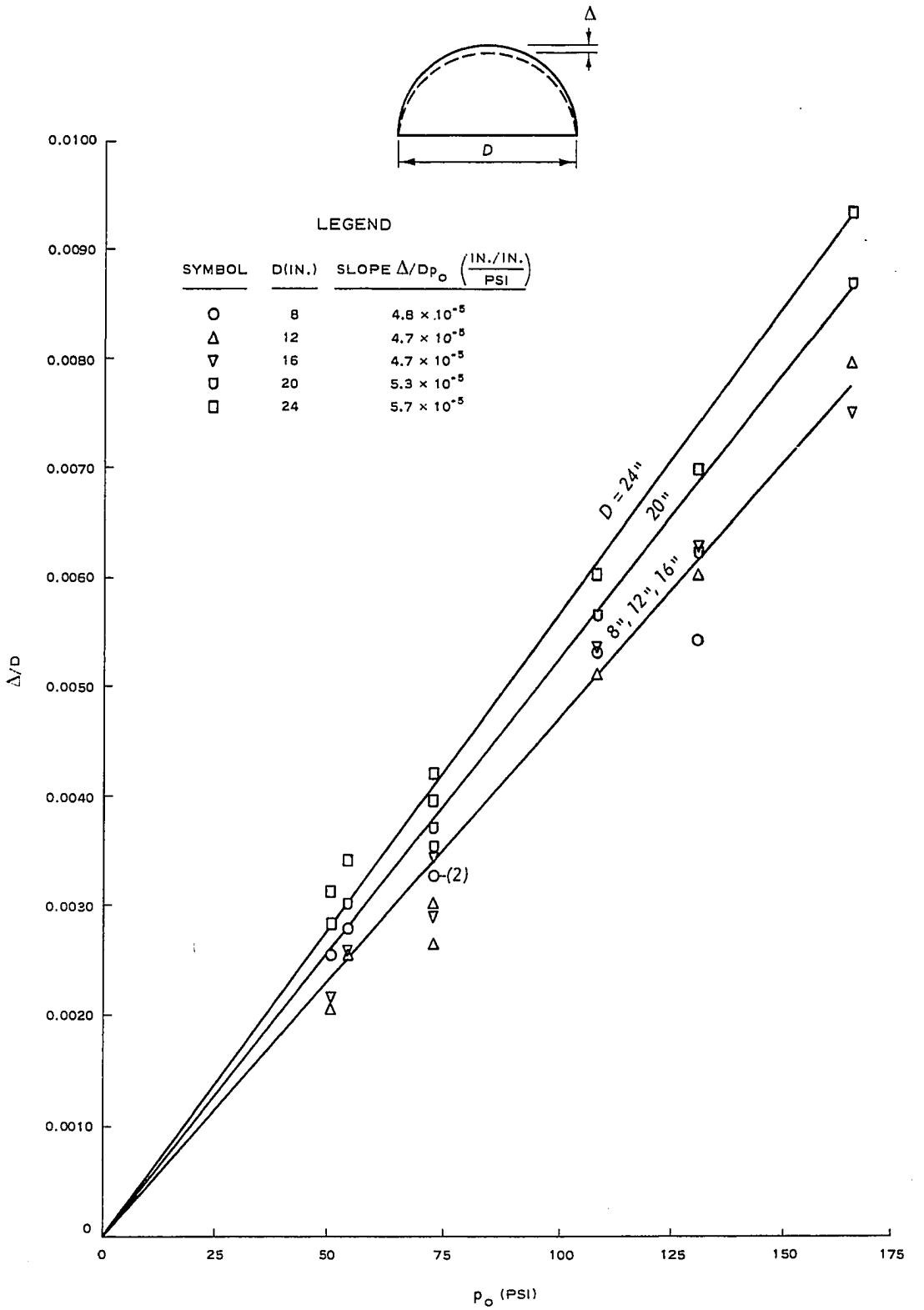

Figure 25. Dimensionless peak deflection versus peak surface overpressure, Series I

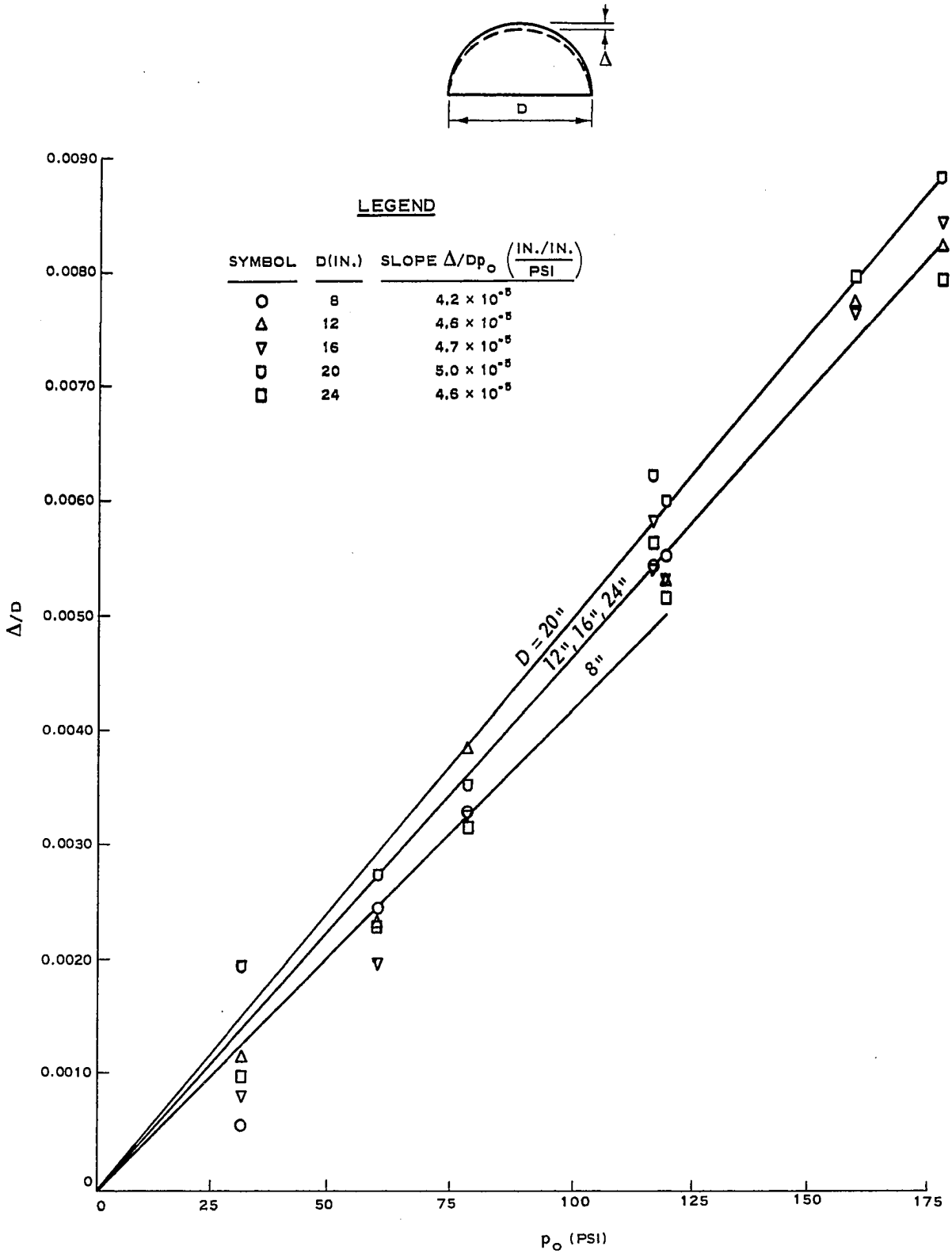

Figure 26. Dimensionless peak deflection versus peak surface overpressure, Series II

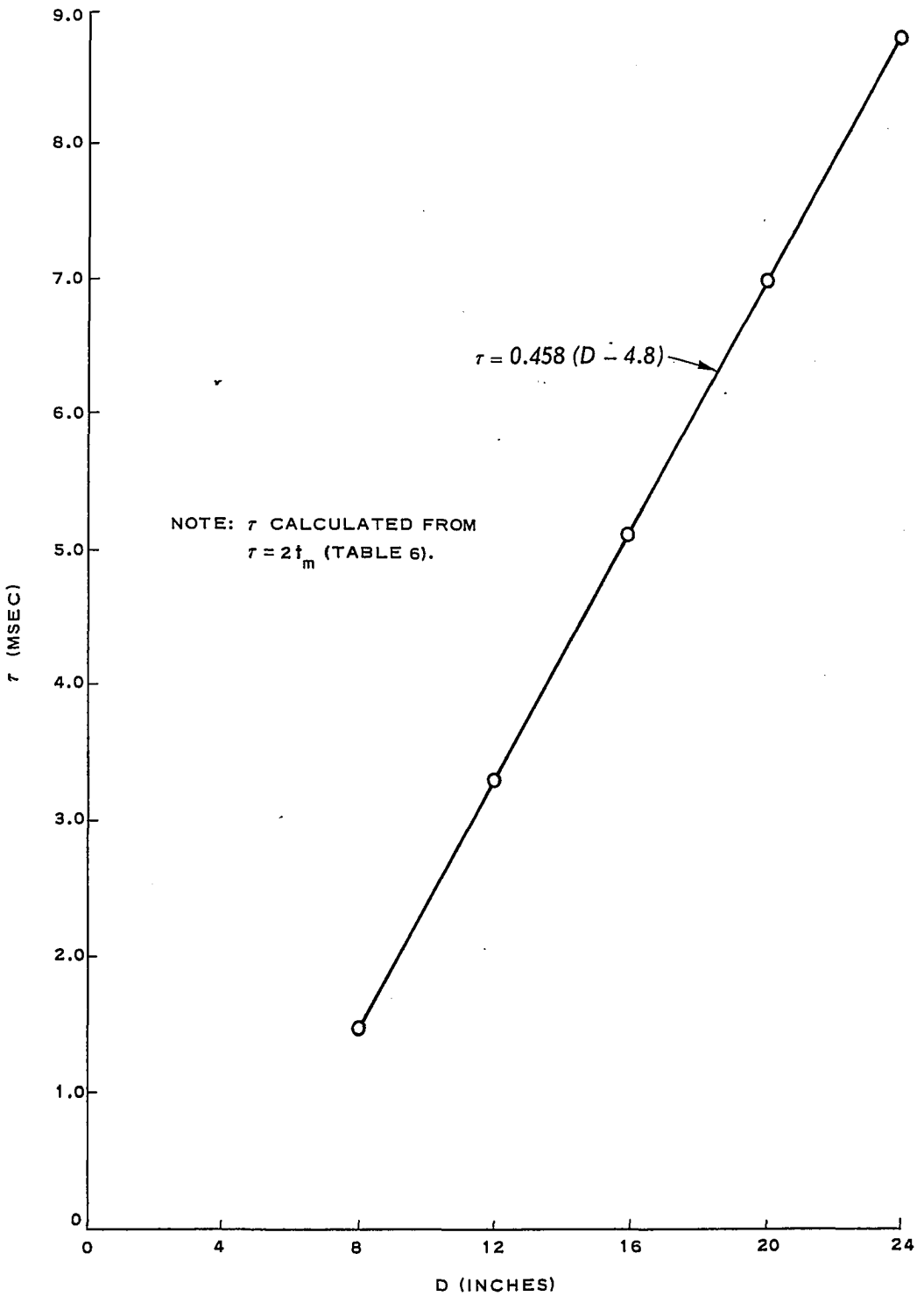

Figure 27. Natural period τ versus arch diameter D, Series I

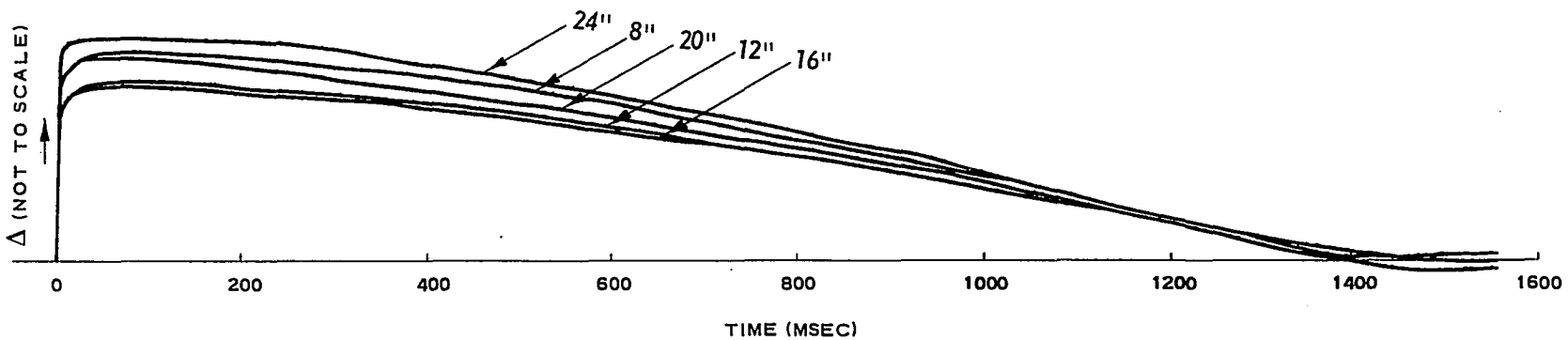

Figure 28. Deflection versus time, five arches, shot 4, Series I

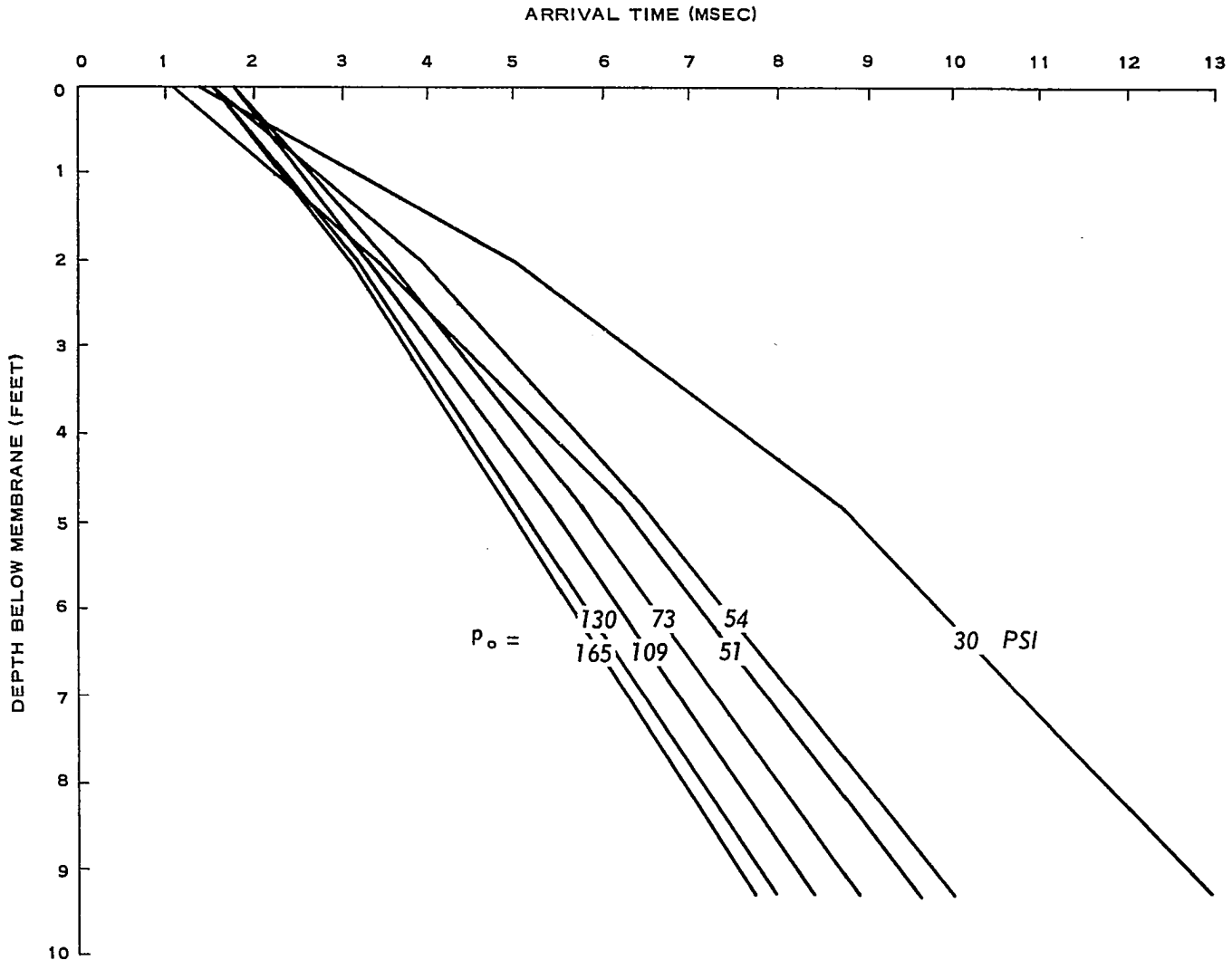

Figure 29. Arrival time versus depth, Series I

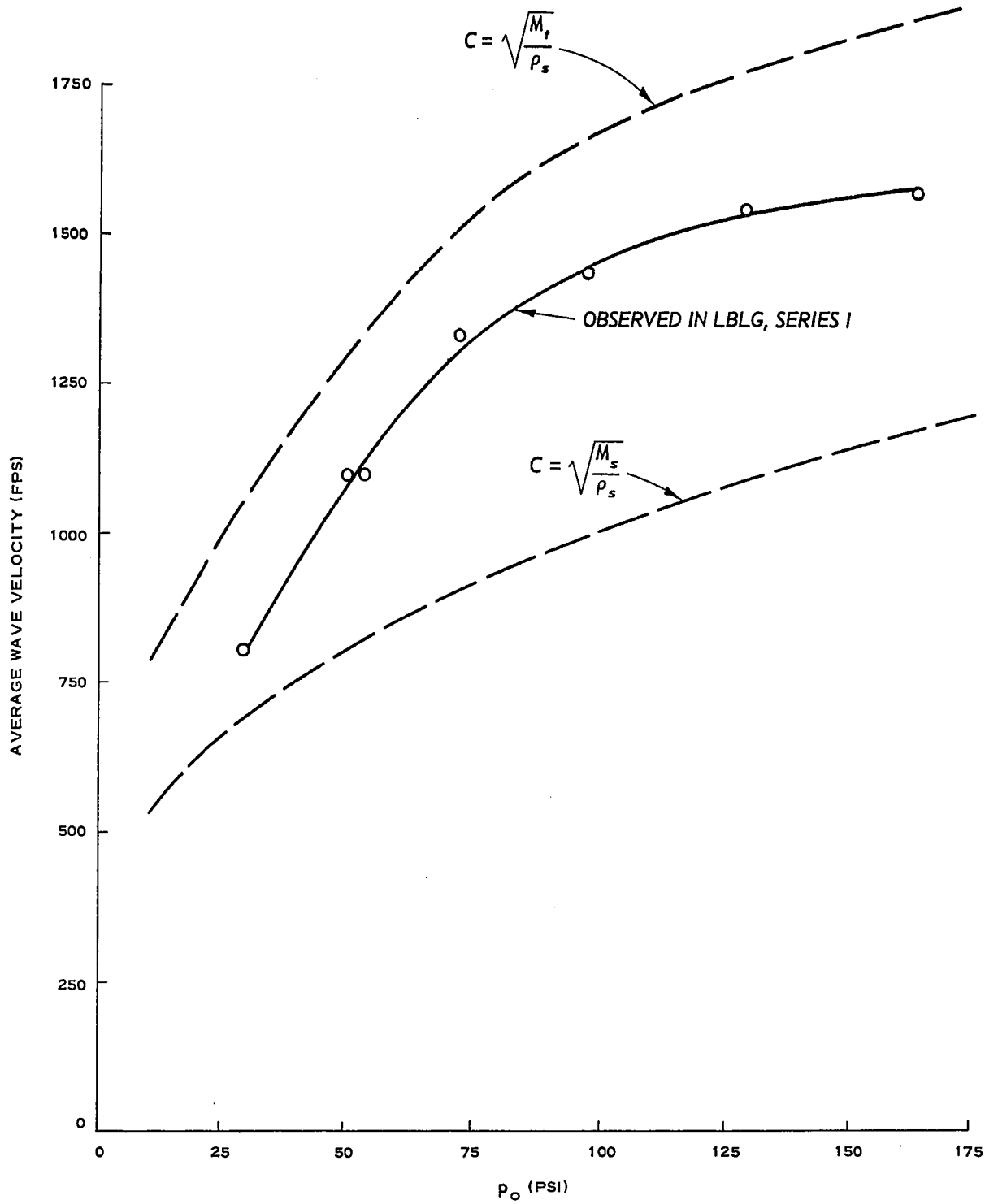

Figure 30. Average wave velocity versus peak overpressure

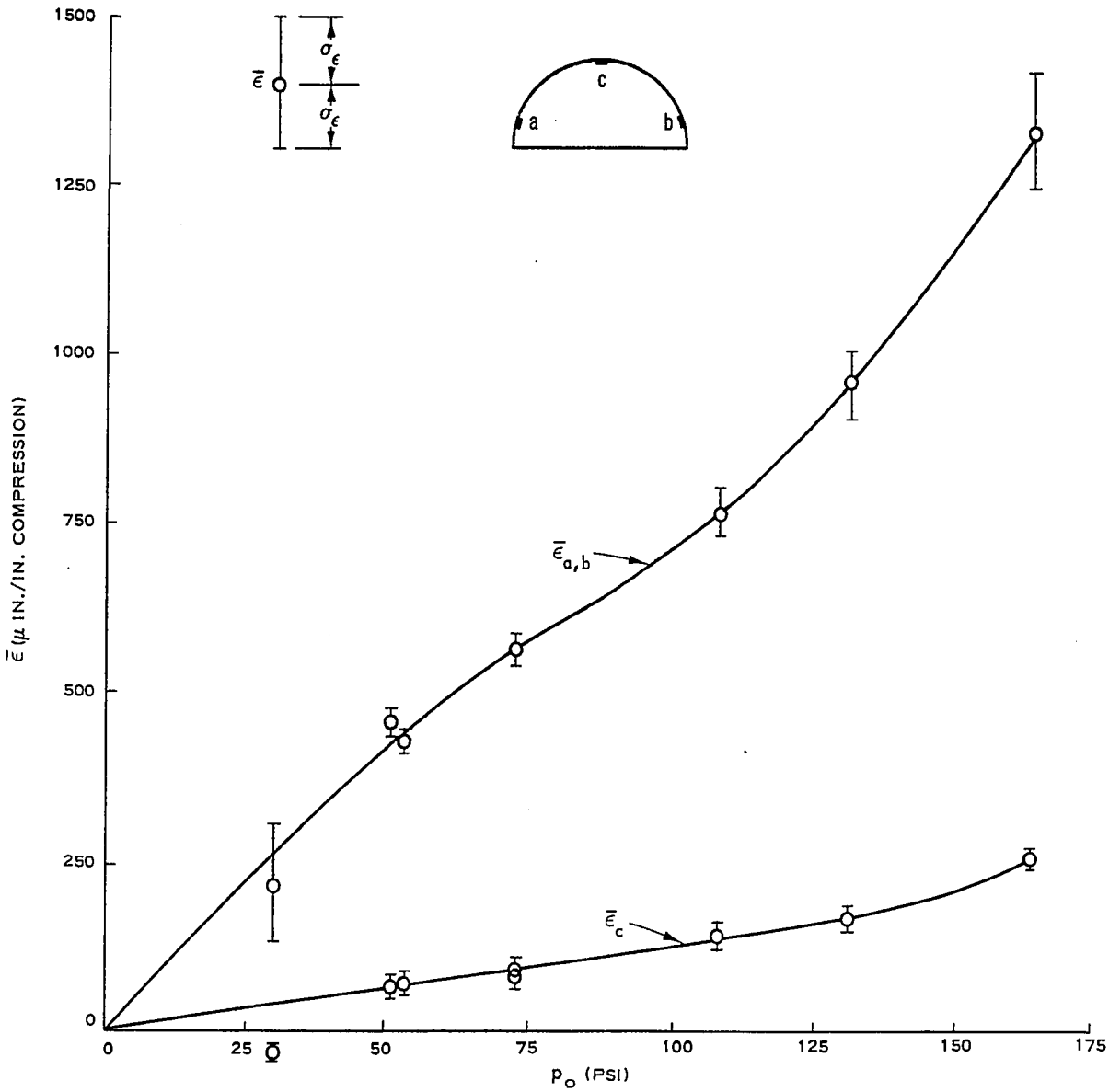

Figure 31. Average peak strain at a , b , and c versus peak surface overpressure, Series I

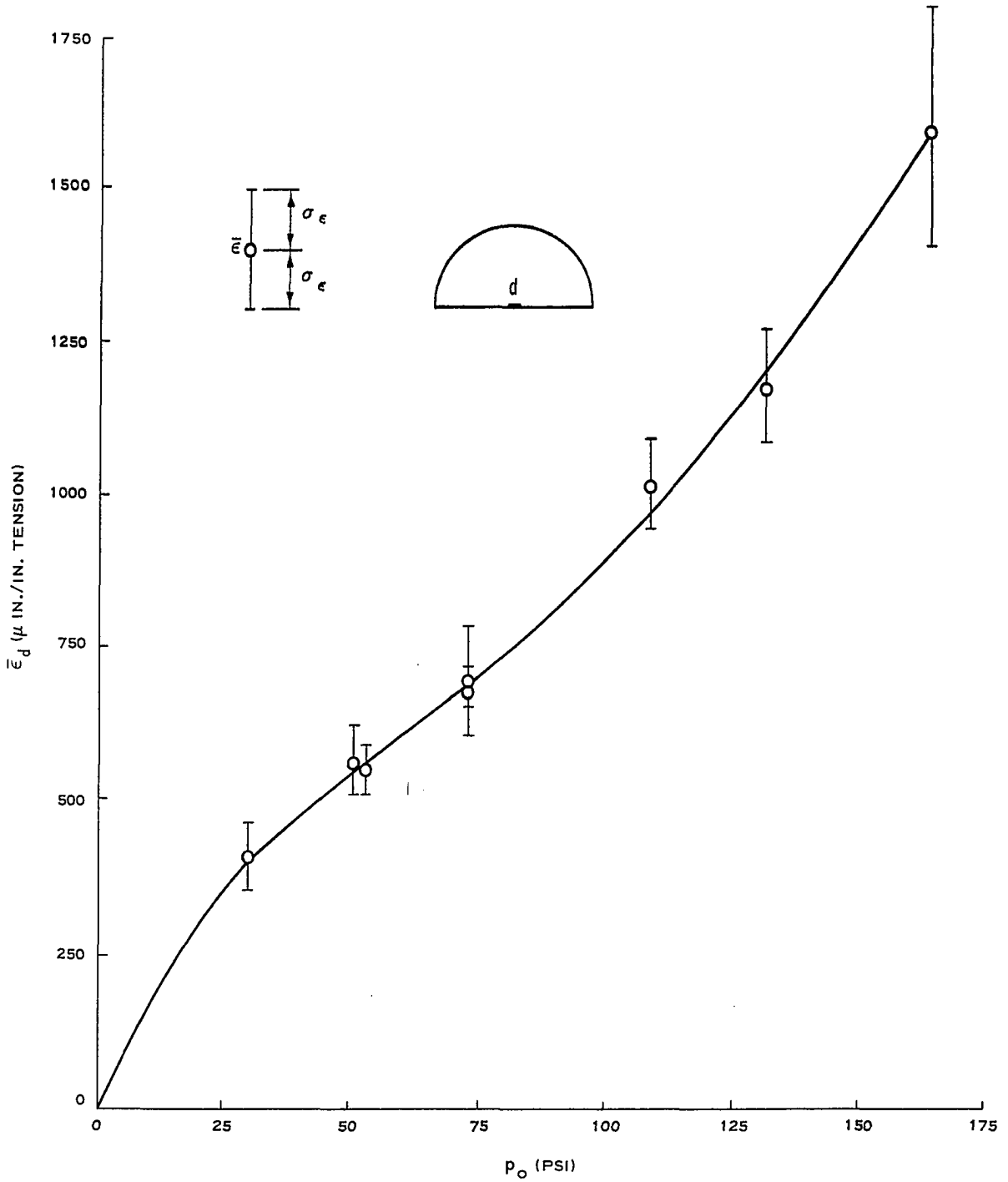

Figure 32. Average peak strain at d versus peak surface overpressure, Series I

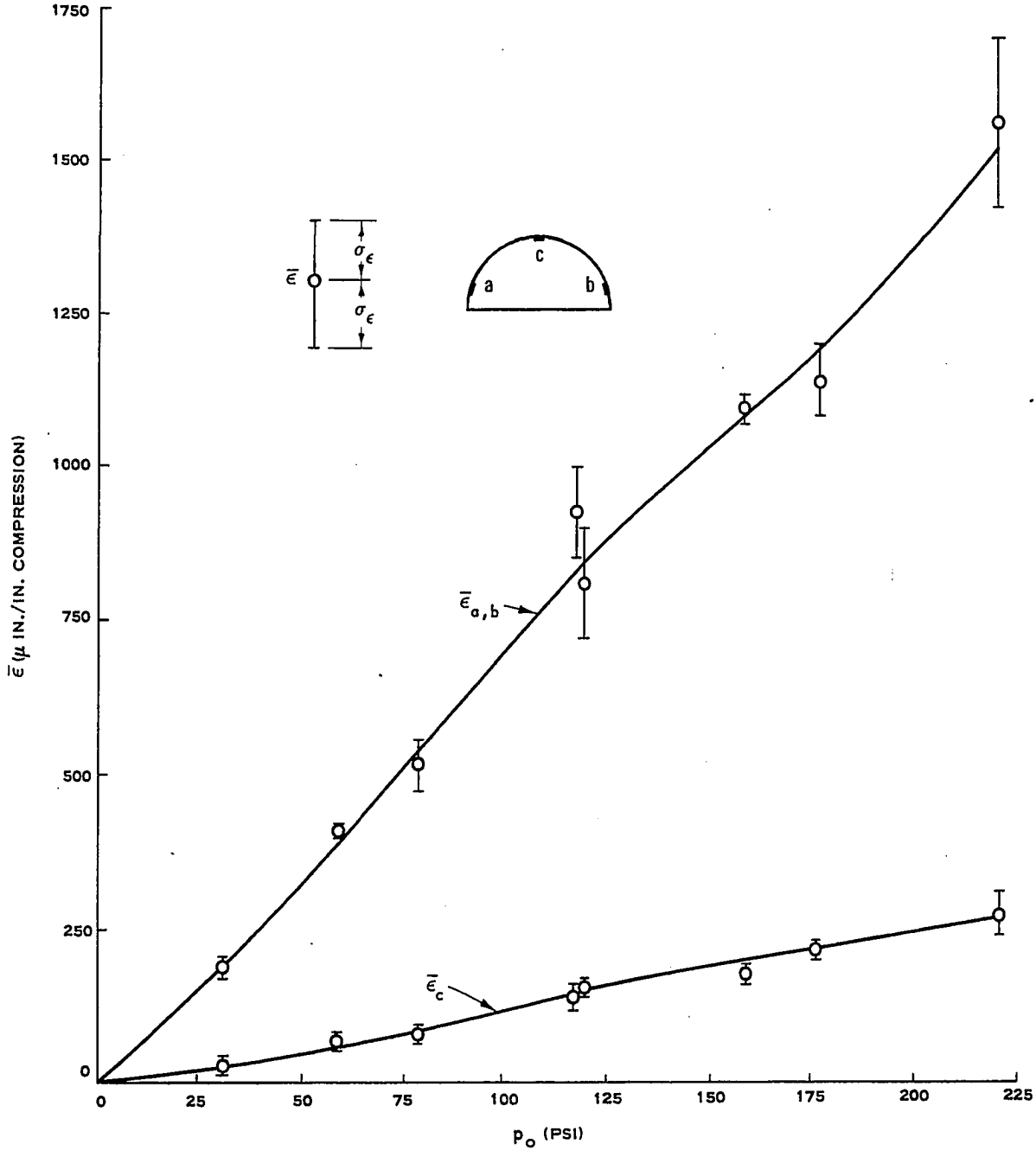

Figure 33. Average peak strain at a , b , and c versus peak surface overpressure, Series II

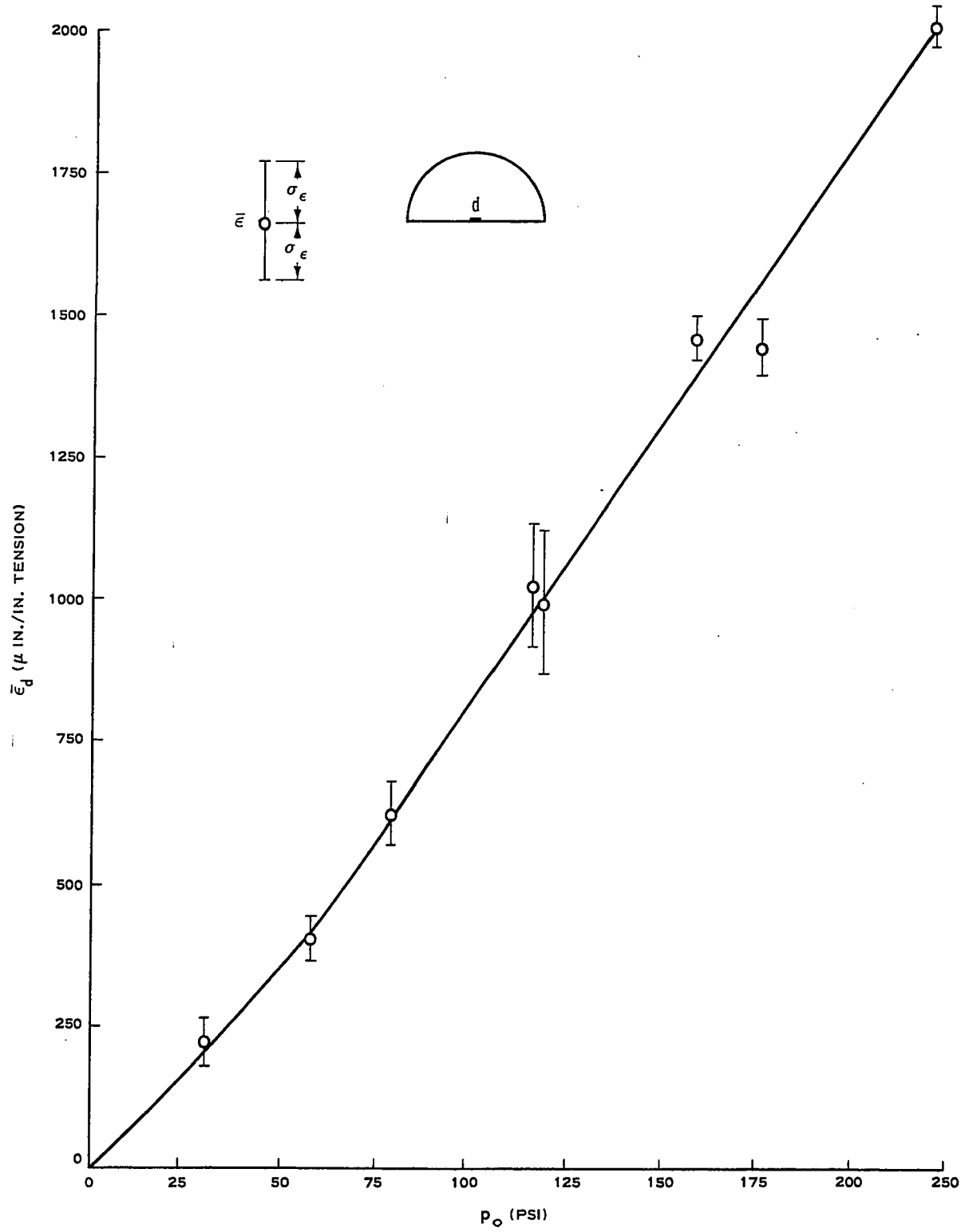

Figure 34. Average peak strain at d versus peak surface overpressure, Series II

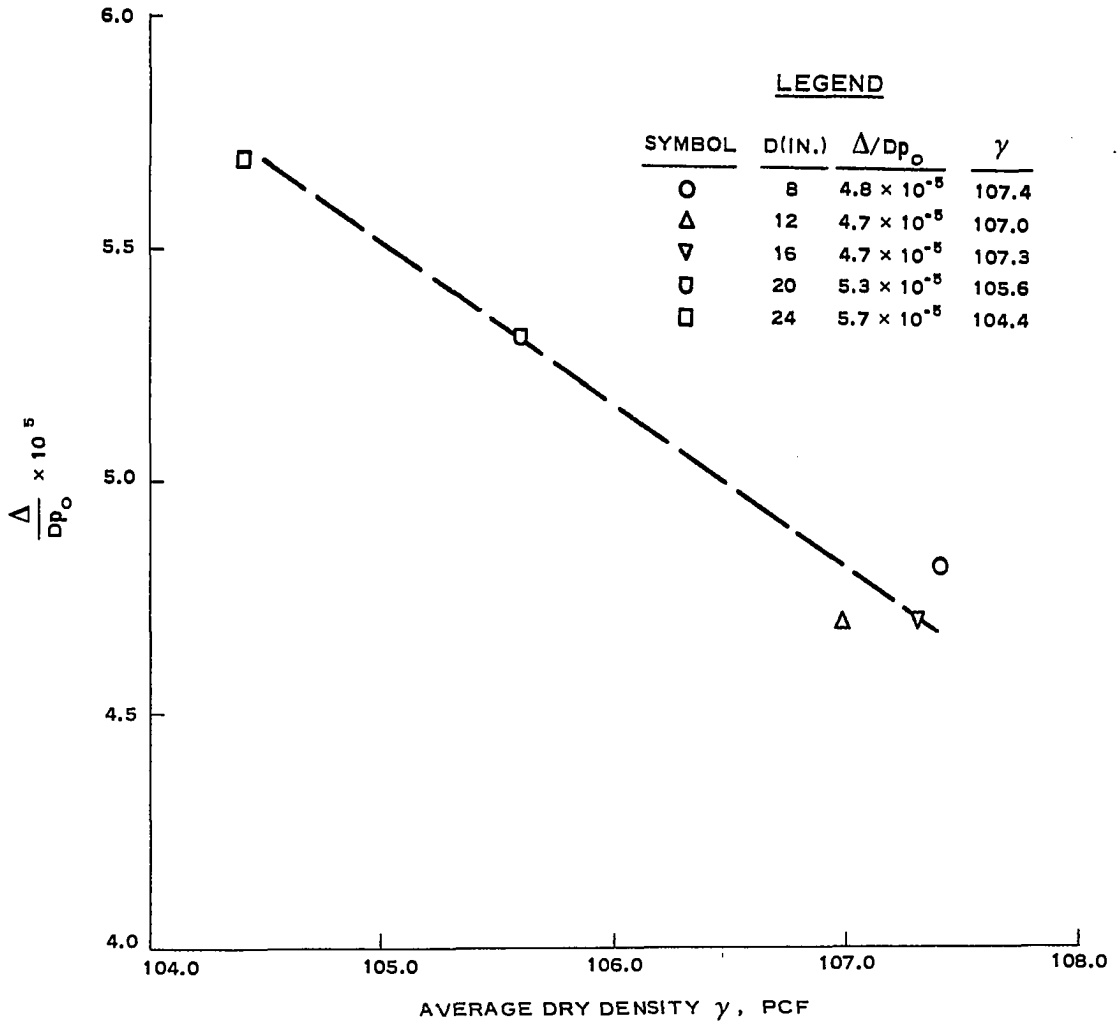

Figure 35. Scaled slope of deflection-overpressure curve versus pretest soil density, Series I

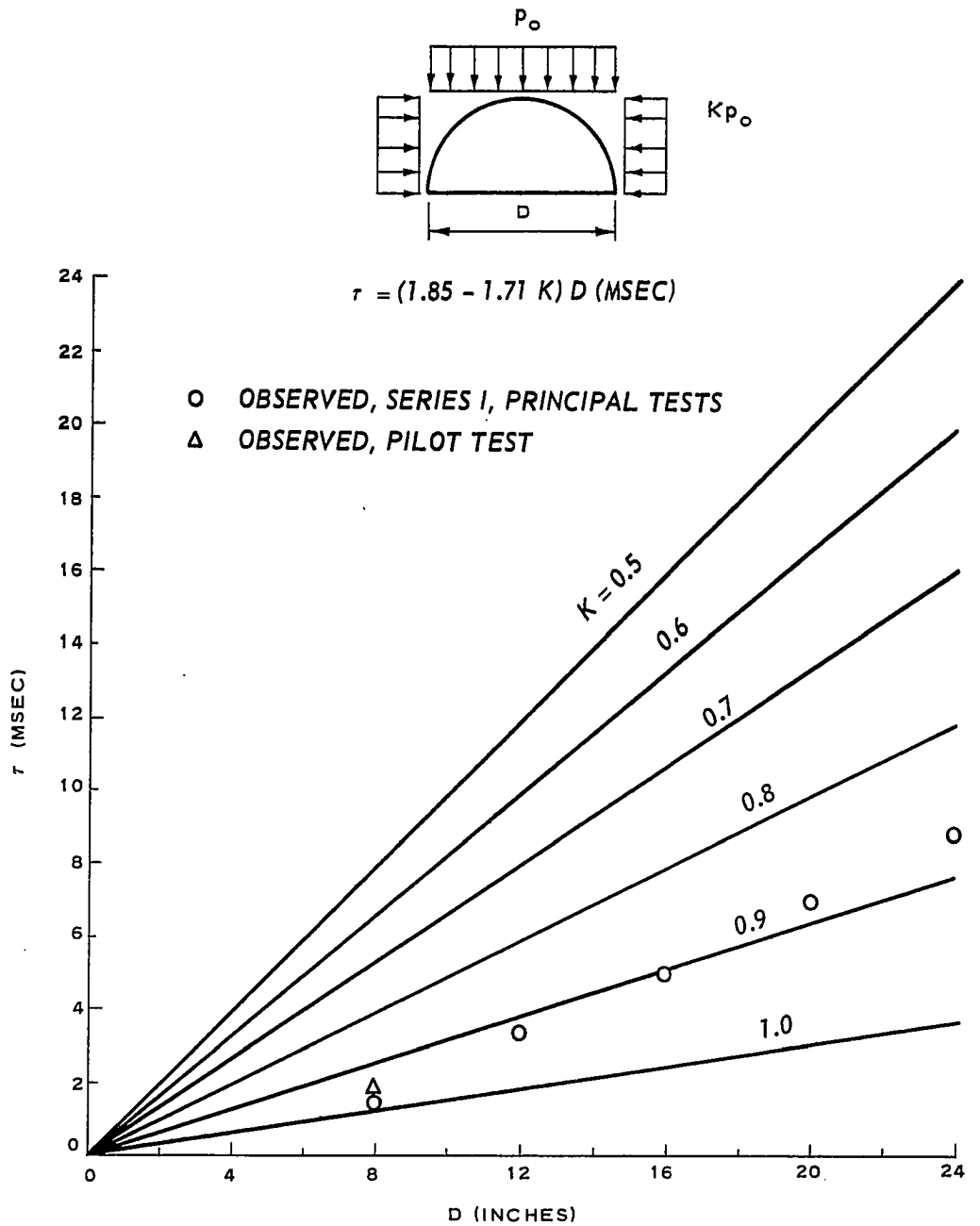

Figure 36. Natural period of vibration of buried arch under equivalent surcharge loading

APPENDIX A: NOTATION

A	Area of longitudinal section of arch roof; also dynamic amplification factor in Equation 5
b	Length of longitudinal section of arch roof; also number of basic dimensions involved in a set of variables
c	Distance from neutral axis to outer fiber in flexure formula; also seismic velocity; also cohesion
C_i	Dimensionless constant (Equation D21)
C_α	Dimensionless coefficient in a general functional relationship (17)
D	Diameter of semicircular arch
E	Modulus of elasticity
E_p	Plastic modulus for structural material
E_s	Secant modulus to stress-strain curve from a triaxial test
F	Basic dimension of force
g	Acceleration due to gravity
h	Depth below surface of medium
H	Depth of burial from surface of medium to crown of arch
I	Moment of inertia of longitudinal section of arch roof
k	Radius of gyration of longitudinal section of arch roof
K	Horizontal load factor for equivalent surcharge load (Figure D2)
L	Length of arch structure; also basic dimension of length
m	Mass of structural element per unit length
sub m	Denotes model system
m'	Mass of structural element plus mass of soil cover per unit length
M	Moment in structural element
M_s	Constrained secant modulus for soil in one-dimensional compression
M_t	Constrained tangent modulus for soil in one-dimensional compression

M_θ Moment in arch roof at angle θ

n Length scale; also number of variables involved in a functional relationship

p_o Overpressure at the surface of the medium (Figure 1)

p_s Level of stress in soil at a point (Figure 1)

P Static load on arch crown (Figure 3 and Figure C9)

R Radius of semicircular arch

s Arc length along section of arch roof, = $R\theta$ (Figure D1); also number of Pi terms required in a functional relationship

t Thickness of arch roof; also time

t_e Effective duration of overpressure

t_m Time to peak dynamic structural deflection

t_r Rise time to peak overpressure

T Axial thrust in arch roof; also basic dimension of time

T_θ Axial thrust in arch roof at angle θ

x Rectangular coordinate (Figure D1)

x' Coordinate = R-x (Figure D1)

x_i General variable involved in a functional relationship

y Rectangular coordinate (Figure D1)

α Distortion factor = $\dfrac{(\pi_i)_m}{\pi_i}$

γ Dry unit weight of soil, pcf

δ Prediction factor = $\dfrac{\pi_1}{(\pi_1)_m}$

Δ Vertical deflection of the crown of an arch with respect to the center of the floor of the structure

$\Delta V_b^{\tan c}$ Vertical deflection of point b with respect to a tangent to the structure at point c

ΔV_c Vertical deflection of point c

ϵ Unit strain at a point in structure

$\bar{\epsilon}$ Average value of peak dynamic strain, all structures

ϵ_θ Unit strain at angle θ

θ Angular coordinate of a point on the arch roof (Figure D1)

λ Any representative geometric length

π A dimensionless, independent product of variables, or Pi term

ρ Mass density of structural material

ρ_s Mass density of soil medium

σ Stress at a point in structure

σ_y Yield strength of structural material

σ_ϵ Standard deviation in peak dynamic strain

σ_θ Stress at angle θ

τ Natural period of vibration of structure buried in soil

τ' Natural period of vibration of unburied structure

τ_c Natural period of vibration of arch in compressive mode

τ_f Natural period of vibration of equivalent beam in flexural mode

ϕ Angle of internal friction for soil

APPENDIX B: DESCRIPTION OF TEST FACILITIES

A. Structures

1. Selection of geometry and material

For the purpose of experimentally verifying the model theory developed, a specified geometry and material for the model structure are not essential. Any geometrical section, circular, rectangular or otherwise, which could be fabricated would serve. A semicircular arch with an integral floor plate was selected for this study for the following reasons:

1. The arch was considered to be a typical configuration for a realistic buried structure.

2. Information on design and analysis of dynamically loaded buried arches is available in the literature. This information was of value in properly selecting structural dimensions and designing tests.

3. Fabrication was relatively simple.

4. Other analytical studies and experimental investigations, including full-scale field tests, were concerned with arch sections. Data generated from tests on arches in this study would be of potential value to other investigators.

5. Installation of the arch with an integral floor plate in the dry sand medium would be relatively simple.

The size of the structures was chosen in accord with the size of the test chamber of the loading device and practical considerations of instrumentation. Arch diameters of 8, 12, 16, 20 and 24 inches were selected. It would be desirable to test structures with as large a value of length scale as possible, and it may be possible in the future to

construct scale models of the structures used with diameters larger than 24 inches and smaller than 8 inches. However, the objective of the present investigation could be accomplished for the maximum n of three which was provided.

Aluminum was selected as the structural material after consideration of other possible materials such as cement mortar or "microconcrete," plaster of Paris, other castable materials and steel. The reasons for selection of aluminum were:

1. Aluminum is relatively easy to fabricate.

2. Strain gaging of aluminum presents no difficulty as compared with microconcrete or other castable materials.

3. The elastic modulus for aluminum is linear as compared to most castable materials.

4. Numerous repeated loadings on the structures were possible, whereas the use of a castable material would introduce the possibility of hysteresis or brittle fracture which might preclude repeated use.

5. Steel was considered too stiff for the magnitudes of structural response desired.

It was hoped that a test section could be selected which exhibited a two-dimensional response, or as close thereto as possible. An arch length of two diameters was selected as an appropriate dimension, with plans to instrument a section at midlength and provisions to minimize restraint of the arch roof at its ends.

Calculations based on existing theory and experimental data indicated that an aluminum roof diameter-to-thickness ratio (D/t) of 80 would give elastic response and measurable deflections for surface overpressures in

the 100- to 300-psi range and burial depths of one to three diameters. This resulted in a relatively stiff structure, whose response would be qualitatively more comparable to that of a reinforced concrete prototype such as the Plumbbob 3.1 arches (9) than to that of a flexible prototype such as a corrugated metal arch. The experimental advantage of the stiffer structure was primarily its resistance to deformations during installation, since it is known that initial deformations of flexible buried arches significantly influence their dynamic response.

However, an important limitation on the applicability of the test results was imposed by the structural stiffness. The high ratio between the structural stiffness and the stiffness of real soils indicated that variations in the properties of different soil media might not greatly influence the structural response. If true, this would limit the applicability of the results of these tests to situations in which the effect on structural response of varying the soil properties is slight. As a consequence, conclusions based upon this study are necessarily limited to similitude between systems of comparable relative soil-structure stiffnesses.

2. Fabrication and assembly

The arch roof and floor pieces were fabricated by the Washington Aluminum Company, Inc., of Baltimore, Maryland. The semicircular roofs were rolled from 5086-H32 aluminum plate to specified dimensions (Figure B1). The milled floor piece was grooved for a tight fit of the roof piece at the springing line, and the joint was secured with screws. Figure B2 shows the arches as received by WES. The dimensions were

thoroughly inspected, and it was found that the roof and floor thicknesses and the horizontal diameters were within the specified tolerances. The radii of the arches were nominally accurate, but the variation in radius around a given structure exceeded specified tolerances slightly. The maximum variation in the radius around the 180° circumference of each arch is indicated in Table B1. These variations were not considered to be detrimental to the structural behavior, and were felt to be characteristic of the rolling process even with the best quality control.

Endwalls were designed to fit flush with the ends of the arch roof and floor (Figure B3). The endwall plates were fastened to the floor only near the springing line and a gap was left around the endwall sufficient to enable the roof and floor to deflect freely within the range of deflections anticipated. The two endwalls were braced longitudinally by a tie assembly.

After installation of gages, the structures were sealed for buried testing by covering the endwall gaps with Scotch "Magic Mending" tape. Small gaps around the instrumentation cable and endwall connectors were sealed with a room-temperature vulcanizing silastic compound (RTV).

3. Instrumentation

The dependent variables selected for prediction were strain and deflection. For the purpose of verifying the model theory, the specific locations at which strain and deflection are recorded are not essential. It was necessary to ascertain only that the five scaled structures responded in the same mode, and that the locations at which strain and deflection were monitored corresponded geometrically between structures.

Tests were conducted on a pilot model (Appendix C) to aid in determining the most advantageous locations for monitoring strain and deflection. It would have been desirable to utilize a large number of strain gages on the structures to enable an extensive determination of moments and thrusts throughout the arches. However, practical limitations on the number of channels of instrumentation available indicated a maximum of five strain gages on each arch.

As a result of the pilot tests, it was determined that suitable locations for strain gaging the interior of the structures would be radially at 15° above the horizontal, at the crown, and on the floor center line (Figure B4). The 15° locations were selected as points at which relatively high strains would be observed, thus minimizing instrumentation error. Locating these gages any closer to the springing line might have allowed localized springing line joint irregularities to influence the observed strains. It was felt that by locating two gages symmetrically across the structures, any asymmetrical arch response would be detected. The crown and floor locations were selected as appropriate due to the structural symmetry. Strain gages were also installed longitudinally at the crown on each arch to gain an indication of longitudinal bending caused by nonplaneness of the wave and by soil arching over the ends of the structures.

The deflection between the crown and the floor was monitored along a vertical radius (Figure B4). This location was the simplest at which to install the linear variable differential transformer (LVDT) used and was considered to be representative of the arch deflection response.

The strain gages used were Micro-Measurements, Inc., Type EA-13 foil

gages, epoxy-backed and temperature-compensated for use with aluminum. It was desirable to scale the gage lengths according to the length scale of the structures. The actual gage lengths used for the 8-, 12-, 16-, 20- and 24-inch-diameter arches were 0.125, 0.187, 0.250, 0.250 and 0.375 inches, respectively, the required 0.313-inch gage length not being available for the 20-inch arch. The strain gages were bonded to the structure with Eastman 910 epoxy using standard techniques. A complete four-arm bridge was completed inside the arch. The active gage comprised one arm, and the other three arms consisted of foil strain gages, from the same manufacturer's lot number, which were bonded to a 1/2-inch-thick bar of aluminum. This procedure of bridge completion provided excellent temperature compensation and circuit balancing characteristics. The bar with the 15 dummy gages for each arch was slipped over one rod of the endwall tie assembly and silastic RTV was used for shock-isolating the bar from the rod. It was confidently expected that strain in the dummy gages due to distortion of the bar would be negligible, and subsequent tests bore this out.

The signals from the strain gage bridges were carried from the structure by Alpha 1327 wire, a standard multiconductor communication cable composed of pairs of unshielded stranded wire (seven #30 strands per wire). Multiconductor connectors (Amphenol AN 3057-28) were used in this cable at a distance of several feet from the structure to facilitate installation and removal of the structure from the test chamber.

The LVDT's used to measure deflections were G. L. Collins Corporation Model SS-102 d-c linear displacement transducers with a range of $\pm$0.10 inch (Figure B5). The 6-volt d-c input required was supplied by a common

wet cell battery for all five gages. The Collins gage input and output signals were carried by Belden YR7869 4-conductor shielded cable. The gage body was installed in a mounting assembly fixed to the arch floor, and the core of the gage was spring-loaded to ride against a small glass chip bonded to the inside of the crown.

The structures were also instrumented for acceleration. It was felt that knowledge of structural accelerations might prove useful in relating the response of the five scaled structures. Additionally, upon development of a reliable procedure for doubly integrating acceleration records to produce deflection-time curves, it would eventually be possible to compare gross structural movement between the five structures. This data would potentially support a modeling procedure for this response. The transducers used were Columbia Research Laboratories, Inc., Model 504-S3 accelerometers (Figure B5). These piezoelectric transducers have a range of 0.03 to 20,000 g's and weigh 12 grams. Two of the structures had one accelerometer mounted at one side of the floor at midlength, and three structures had two accelerometers mounted on the floor symmetrically opposed (Figure B4). For these three structures, it would be possible to determine to some degree the extent to which the structure "rocked" laterally rather than was displaced vertically.

Figure B6 shows the inside of the 16-inch arch with all gages in place.

The 8-inch principal model arch was buried in the SBLG and dynamically tested under similar conditions and by the same procedure used in the pilot tests (Appendix C). Two shots on this structure verified that

all gages functioned properly and established confidence in the instrumentation.

B. Large Blast Load Generator (LBLG)

The LBLG is a laboratory test facility for generating blast loads with characteristics similar to those which result from nuclear weapon detonations. It is capable of generating a peak dynamic overpressure in excess of 400 psi. A detailed description of the LBLG has been reported (14, 26) and this section will briefly describe the salient features of the facility.

The two basic components of the LBLG are the central firing station and the test chamber (Figures B7 and B8). The central firing station is a massive, posttensioned, prestressed concrete reaction structure designed to resist the large dynamic loads generated in the test chamber. The test chamber is a cylindrical steel bin 23 feet in diameter which contains the test specimen. A depth of 10 feet is available for the test medium. In the top of the test chamber are located 15 firing tubes which contain the explosive charge used to generate the blast loading. A baffle system directly beneath the firing tubes serves to break up the discrete shock waves from each firing tube in order to obtain a uniform pressure distribution across the surface of the medium. The ring surrounding the firing tubes contains 28 exhaust valves which can be programmed to open at specified times for the purpose of controlling the decay characteristics of the pressure pulse.

In preparing for a shot, the test structures, medium and appropriate instrumentation are placed in the test chamber. The proper quantity of

explosive is selected to produce the desired air overpressure and is loaded in the firing tubes. The ring containing the firing tubes is placed atop the baffles and test specimen. The lid for the test chamber fits into a peripheral slot in the top ring in a telescopic fashion. The platen supporting the test chamber is drawn into the central firing station on rails and the rails are lowered, allowing the bottom of the platen to rest on the central firing station floor. Nitrogen gas is forced under pressure into the peripheral slot between the top ring and the lid, forcing the telescoping lid upward so that the flat top of the test chamber is in intimate contact with the roof of the central firing station. Final instrumentation connections and checks are made, and the charge is detonated electrically by means of a standard engineer cap and primacord leader.

Prior to the tests reported herein, the LBLG had been fired 28 times. These earlier shots comprised calibration tests and also provided valuable data regarding the surface pressure distribution and free-field phenomena. The test program reported herein constituted the first firings upon actual structures installed in the LBLG.

C. Test Medium

1. Description of sand

The soil medium for the test program was a clean, uniform fine sand, known locally as Cook's Bayou No. 1 sand. Extensive soil laboratory tests have been conducted on this sand (25), and some of its properties will be briefly described. For all laboratory tests and LBLG tests the sand was thoroughly dried.

Cook's Bayou No. 1 sand is classified as SP in the Unified Soil Classification System. Figure B9 shows the gradation curve. Its specific gravity is 2.65 and photomicrographs indicate that particle shapes vary from rounded to angular, with subrounded shapes predominating. Maximum and minimum laboratory dry densities of 110.8 and 93.3 pcf were obtained using WES compaction techniques (25). Direct shear tests indicated angles of internal friction (ϕ) from 35.0 to 42.5 degrees for dry densities of 97.0 to 110.5 pcf. For the average density of 107.0 pcf attained in the specimens tested in this study, ϕ = 37.0 degrees.

Static, stress-controlled, one-dimensional compression tests were performed on specimens at four densities in a fixed-ring consolidometer. The stress-strain curves obtained are plotted in Figures B10 and B11. Tangent moduli were determined from the slope of the tangent to the stress-strain curve at various levels of stress, and Figure B12 shows the variation in constrained tangent modulus with stress. At initial densities ranging from 97.0 to 110.4 pcf, the tangent moduli ranged from 4000 to 14,000 psi at a vertical stress of 6.9 psi, and from 46,000 to 126,000 psi at a vertical stress of 445 psi.

The data presented indicate only the static strength and compression properties of the sand used. Based on recent research in which a similar clean, dry sand was used, it is not expected that corresponding dynamic strength and compression properties of Cook's Bayou No. 1 sand will be significantly different from the static data reported (25). However, it is planned to conduct future dynamic triaxial tests on this sand with equipment presently available at WES. Dynamic one-dimensional compression tests will also be conducted with apparatus currently being developed.

2. Installation

It was shown in the identification of pertinent variables in Section III that the density of the sand alone is the controlling factor for the properties of the medium. The design conditions required that the density be the same for all structures. Installation of the sand was performed with the objective of attaining a uniform sand density throughout the LBLG test medium.

Preliminary tests of showering and vibrating compaction techniques indicated that an in-place dry density of 107.0 to 107.5 pcf could be consistently obtained by both methods. Sand was showered with the equipment shown in Figure C5 from a drop height of 24 to 30 inches, and was vibrated in 6-inch lifts with five passes of a Vibro-Plus Type 500 vibrator, mounted on a 16- by 36-inch curved steel plate, operating at 3600 rpm. The portion of the test specimen below the elevation of the structures was installed by the less time-consuming vibration technique. Each structure was placed on a level screeded surface (Figure B13), and the remainder of the specimen was built up by showering sand around and over the structure.

Density samples were taken at selected locations during each installation. Additionally, cone penetration tests were used to correlate the uniformity of density throughout the specimen. The actual in-place density of the medium varied between 104.4 and 108.0 pcf throughout. The in-place dry density of the sand in the vicinity of the structures for the two test installations is given in Table B2. It is noted that the control of density between structures for Series I was not as good as had been hoped for; the density around the 20- and 24-inch arches

was somewhat lower than that in the vicinity of the other structures.

It was necessary to prevent the dynamic air overpressure from entering the sand and causing bulking of the sand due to dynamic pore air pressure. A membrane consisting of a 6-mil polyethylene sheet was placed across the entire LBLG test chamber at an elevation 2 inches below the final sand surface. It was believed that below this membrane the dynamic soil stress would be primarily effective or intergranular stress. Since the 2 inches of sand above the membrane was expected to be considerably bulked and blown about when the firing tubes were detonated, as indicated from previous LBLG shots, the elevation of the membrane was taken to be the surface elevation for the purpose of determining depth of burial of the structures. Thus, a burial depth denoted $H/D = 1.0$ indicates that the distance from the membrane to the crown of the arch was equal to the arch diameter, and the 2 inches of sand covering the membrane was neglected.

A previous series of LBLG tests had indicated that the distribution of overpressure on the surface of the test medium may not be uniform, but may vary with a profile as shown in Figure B14. The extent to which this pressure variation is maintained at depths in the test medium has not been established, and the surface profile postulated in Figure B14 was based on rather limited data. However, in order to assure, insofar as possible, that each structure was subjected to the same level of overpressure, the pressure distribution shown was assumed to be valid and the structures were oriented within the LBLG test chamber so that the instrumented cross section at midlength of each arch would coincide with the 75%-of-peak-pressure contour. The arches were also spaced laterally so that the maximum available undisturbed plan area could be provided around each structure. Account

was taken for possible sidewall friction effects due to the walls of the test chamber. The resulting plan view of the arches for Series I and II is shown in Figure B15. It was felt that this arrangement provided an undisturbed space around each structure of such extent that the boundaries of each structure-soil system, as would affect the response of the instrumented section at midlength, could be considered infinite.

3. Instrumentation

The gas overpressure in the top of the test chamber was recorded by means of pressure transducers located in gage ports in the wall of the firing chamber. It was believed that the peak pressure recorded by these gages during the first 10 milliseconds of the shot was representative of the nominal peak overpressure acting on the surface of the test medium. Two types of gages were used at various times, the Dynisco Model PT-110, 0-1000 psi, orifice-type, bonded strain gage pressure transducer (Figure B5), and the Norwood Model 211A, 0-1000 psi, diaphragm-type, bonded strain gage pressure transducer. Two such pressure gages were used during Series I and six during Series II.

Two buried soil pressure cells were located in the vicinity of each arch as shown in Figure B16. These gages were placed so as to enable determination of the relative uniformity of pressure across the instrumented section of each arch, and to enable comparison between the nominal levels of stress existing in the vicinity of each of the five structures.

In order to measure the magnitude and distribution of surface overpressure, ten pressure gages were placed just under the membrane, at locations directly above the buried pressure cells. It was hoped that

data from these surface gages would enable determination of the nominal overpressure above each structure and provide a means of comparing the surface pressures from one structure to another.

Two additional soil stress cells were buried at depths of 4.83 and 9.33 feet below the membrane on the vertical center line of the test chamber, primarily to obtain shock wave arrival times so that wave velocity could be computed.

The transducer used for the surface pressure and soil stress measurements was a piezoelectric cell developed by the Road Research Laboratory in England (28). This gage has become known as the Road Research Cell (RRC) and is a 3-inch-diameter, 0.65-inch-thick cell employing a quartz crystal (Figure B5). It is a very rugged, highly sensitive element and was designed to detect soil pressures produced by moving wheel loads. Experience with the RRC at WES has indicated that its useful range when buried in dry, dense sand is in excess of 500 psi with a resolving time of better than 100 microseconds. Numerous tests in the LBLG utilizing the RRC have indicated that the detection of the absolute magnitude of soil pressure is very difficult, primarily since calibration of the gage for a known stress input in the soil is impossible. In the development of the gage in England, a constant overregistration of 10% was observed, regardless of the properties of the surrounding soil (28). Results of WES tests have not confirmed this value, and it is believed that a somewhat higher overregistration factor is indicated for resolution of absolute pressures in tests such as those conducted in this study. However, the RRC was thought to be of

potential value in determining relative soil stress between locations, based on a hydrostatic calibration.

D. Data Recording

1. Instrumentation

A total of 63 channels of instrumentation were employed, comprising 25 channels of strain, 5 of deflection, 8 of acceleration, 12 of surface overpressure, 12 of soil stress and 1 to record zero time. Selected channels of strain, deflection, acceleration and pressure were recorded on both recording oscillographs and magnetic tape, so that approximately 90 channels of data were recorded on each shot. The paper records from the oscillographs were used for detailed analysis of the early dynamic response. The tape records were utilized for playback to obtain condensed or expanded response-time curves and for future use in analyzing acceleration records.

Figure B17 is a schematic diagram showing the instrumentation arrangement. Minor changes in this procedure were necessitated at times. Strain, deflection and air overpressure signals were amplified on either Alinco Model Sam 1 amplifiers or Dana Model 2000 d-c amplifiers in conjunction with B&F Instruments, Inc., Model 6-200B4 strain conditioning equipment. These channels were recorded on Consolidated Electrodynamics Corporation (CEC) Type 5-119 galvanometer oscillographs with paper speeds of 100 or 160 inches per second, and on magnetic tape. The piezoelectric transducer signals for acceleration, surface pressure and soil stress were recorded through WES-made cathode followers and Kistler Model 656S6 charge amplifiers on a William Miller Instruments, Inc., Type CR-1A

recording oscillograph with a paper speed of 400 inches per second, and on magnetic tape. The tape units used were Sangamo Model 452R and 472RB magnetic tape recorders. Figure B18 shows the instrumentation equipment.

2. Procedure

After the first shot, it was possible to estimate rather closely the peak response which each gage would experience on the next subsequent shot. Thus the gain for each channel could be set to provide an optimum amplitude for recording. Immediately prior to each shot, calibration steps of known value for all channels were recorded. Initially, calibration steps were also recorded immediately postshot, but it was evident that there were no detectable changes from the preshot calibrations.

In general, about seven hours were required to prepare the instrumentation for each shot. A five-minute countdown to shot time was provided. At shot time minus 10 seconds the automatic timing device on the LBLG controller unit was initiated, which electronically started the recorders at shot time minus one second and then fired the LBLG charge. About 1000 milliseconds of record were obtained on the paper records, and about 2500 milliseconds of magnetic tape record were obtained.

In any data recording operation of this type and magnitude, data channels are sometimes lost during recording due to a number of reasons. Occasional equipment failure and human error are unavoidable. For the tests reported herein, satisfactory records were obtained for 552 out of a total of 602 primary data channels, or 92%.

Table B1. Variations in radii

Nominal arch diameter (inches)	True radius and maximum deviations
8	$4.000^{+0.033}_{-0.018}$
12	$6.000^{+0.044}_{-0.000}$
16	$8.000^{+0.046}_{-0.030}$
20	$10.000^{+0.019}_{-0.054}$
24	$12.000^{+0.041}_{-0.018}$

Table B2. Pretest densities in vicinity of structures

Arch D (inches)	Pre-Series I		Pre-Series II	
	Dry density[a] (pcf)	Rel. density (%)	Dry density[a] (pcf)	Rel. density (%)
8	107.4	83.0	107.6	84.0
12	107.0	81.0	106.6	79.0
16	107.3	82.5	107.2	82.0
20	105.6	74.0	107.8	85.0
24	104.4	67.5	107.8	85.0

[a]Average of two samples.

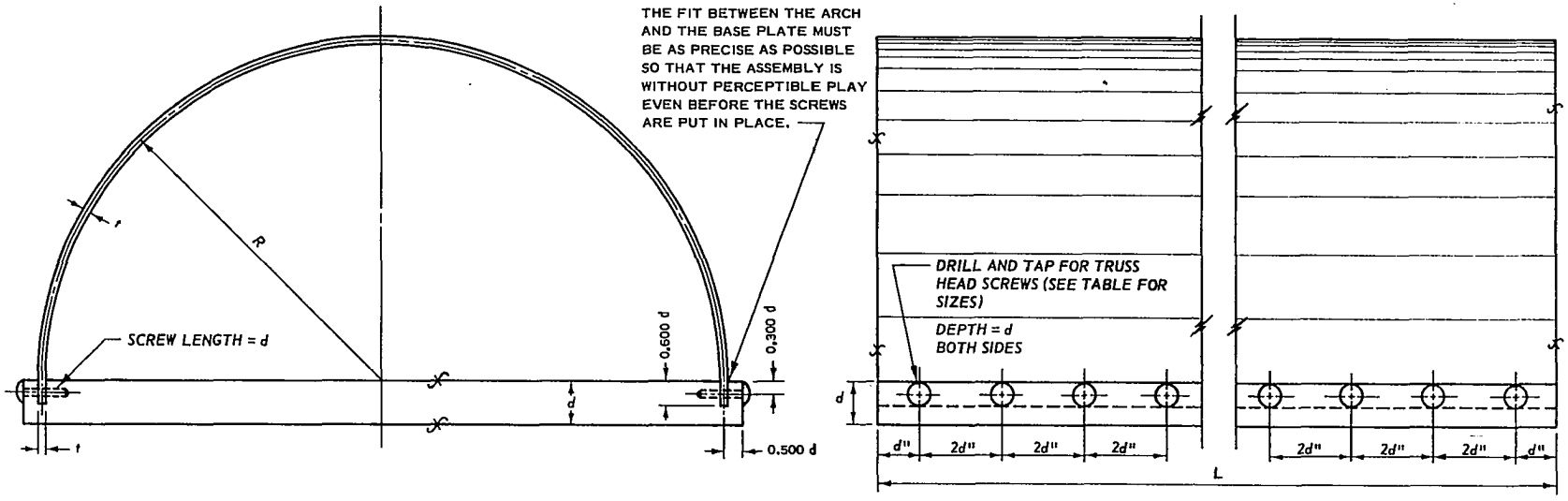

TYPICAL MODEL ARCH

ARCH DIMENSIONS IN INCHES

ARCH NO.	1	2	3	4	5
R	4.000 ± 0.010	6.000 ± 0.015	8.000 ± 0.020	10.000 ± 0.025	12.000 ± 0.030
t	0.100 ± 0.002	0.150 ± 0.003	0.200 ± 0.004	0.250 ± 0.005	0.300 ± 0.006
d	0.500 ± 0.020	0.750 ± 0.030	1.000 ± 0.040	1.250 ± 0.050	1.500 ± 0.060
0.600 d	0.300	0.450	0.600	0.750	0.900
0.500 d	0.250	0.375	0.500	0.625	0.750
0.300 d	0.150	0.225	0.300	0.375	0.450
L	16.000	24.000	32.000	40.000	48.000
SCREW SIZE	#4-40	#8-32	#12-24	1/4"-20	5/16"-18

REQUIRED: 1 EACH SIZE

MATERIAL: ALUMINUM

YIELD STRENGTH: 20,000 PSI MINIMUM
30,000 PSI MAXIMUM

MODULUS OF ELASTICITY MUST BE UNIFORM WITHIN ± 2 PERCENT BETWEEN SPECIMENS.

FINISH: SMOOTH ENOUGH TO PERMIT APPLICATION OF STRAIN GAGES.

HARDNESS, CORROSION RESISTANCE, AND TEMPERATURE CHARACTERISTICS NOT CRITICAL.

Figure B1. Working drawings for model arches

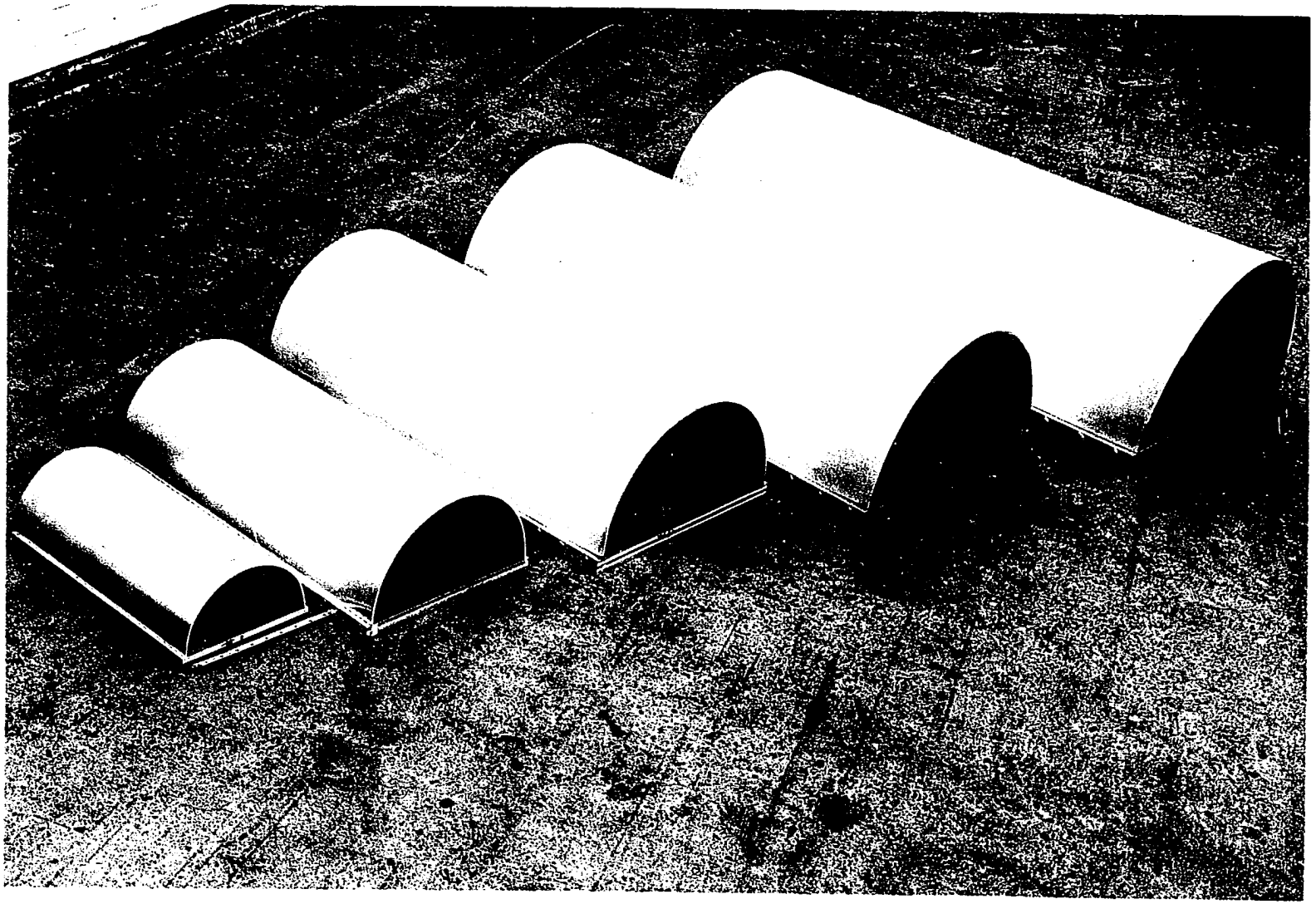

Figure B2. Arch structures without endwalls and instrumentation

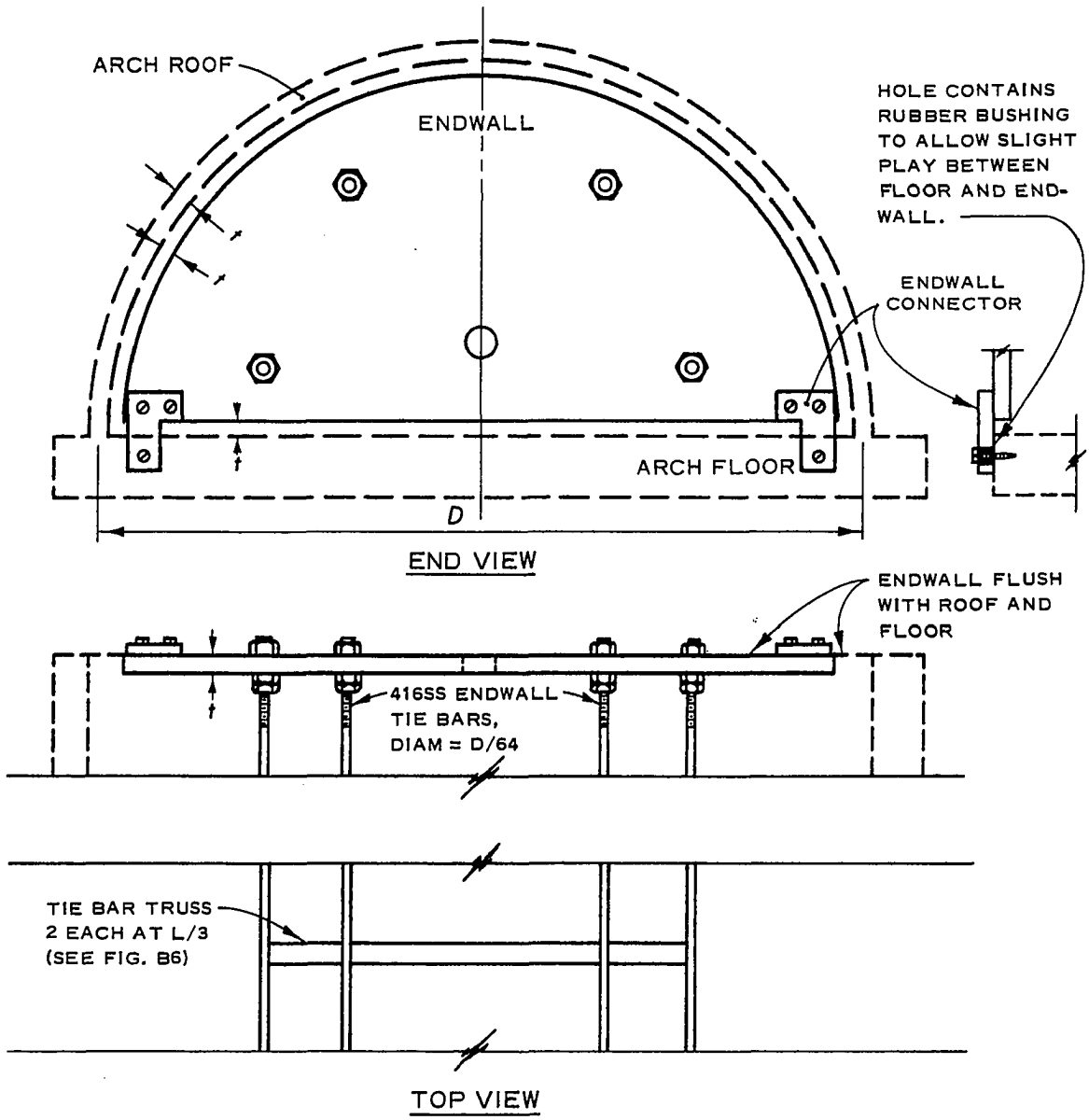

Figure B3. Endwall and tie assembly

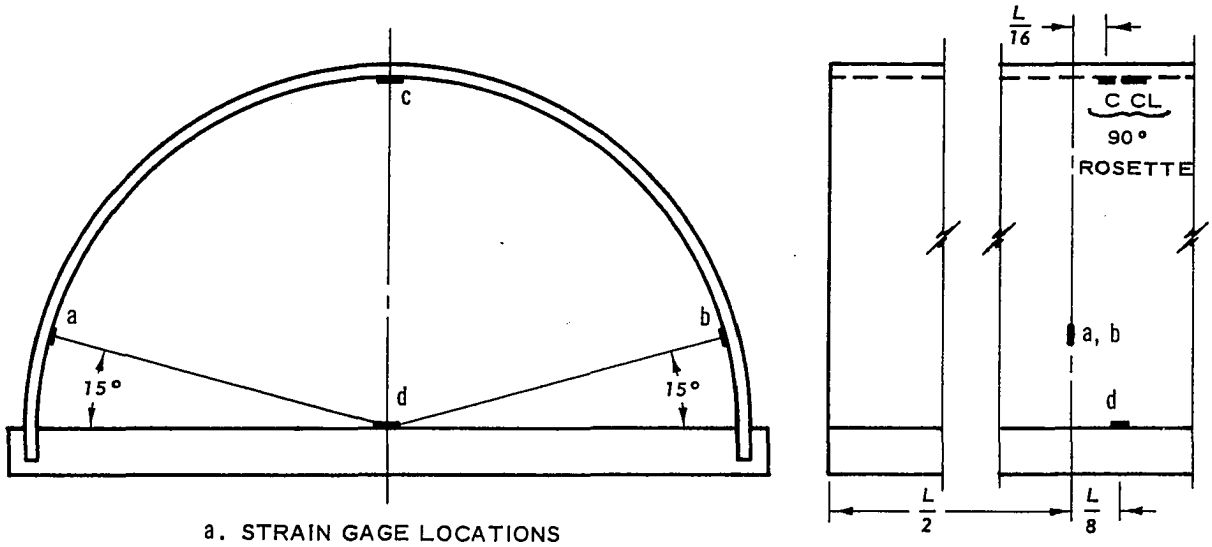

a. STRAIN GAGE LOCATIONS

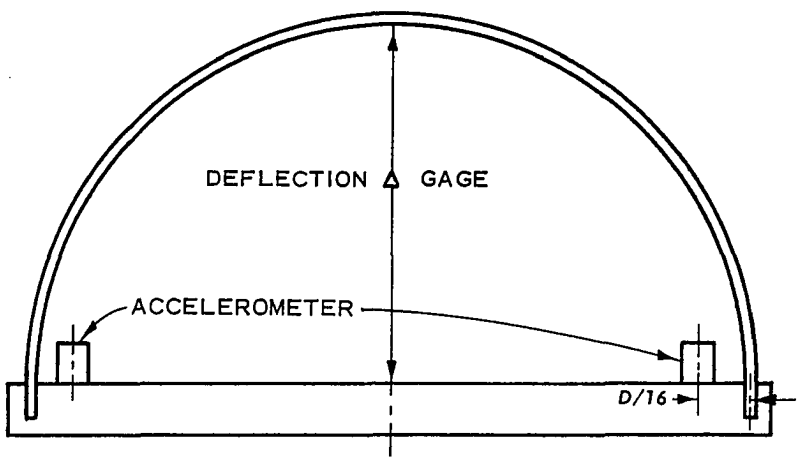

b. DEFLECTION GAGE AND ACCELEROMETER LOCATIONS (AT MIDLENGTH)

Figure B4. Strain, deflection and accelerometer gage locations

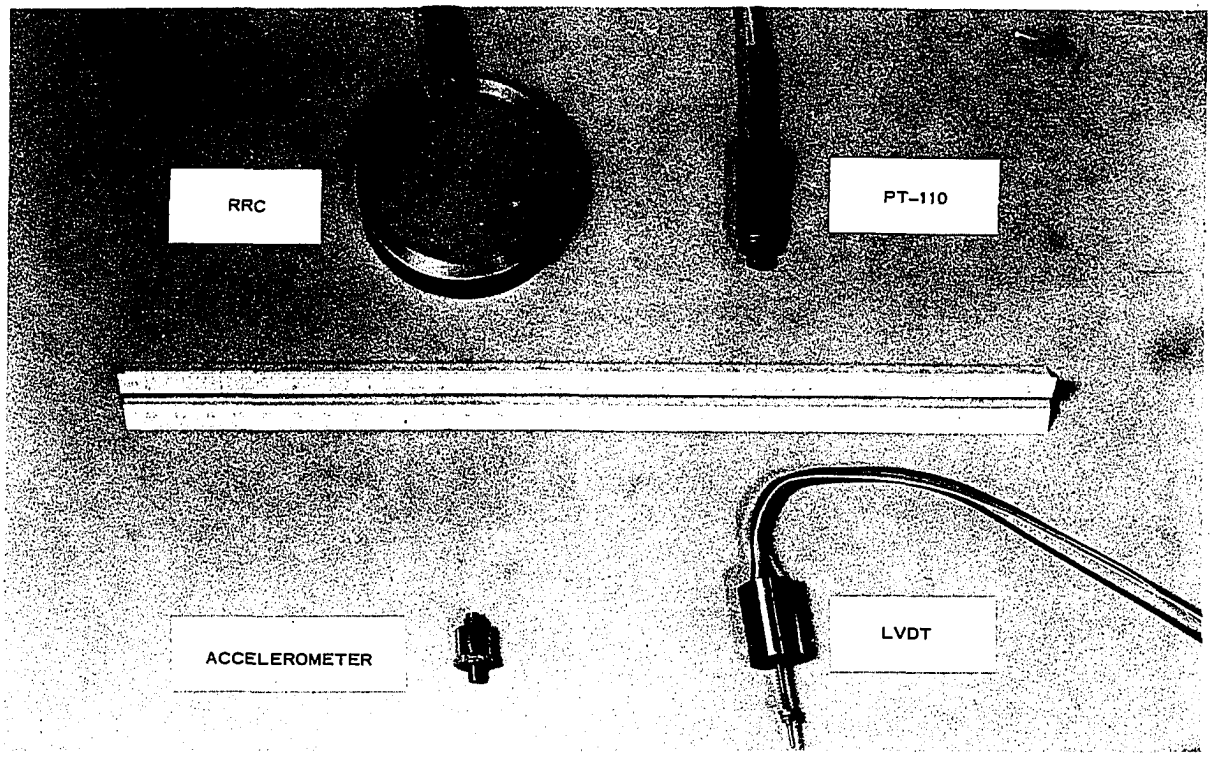

Figure B5. Transducers used in structures and medium

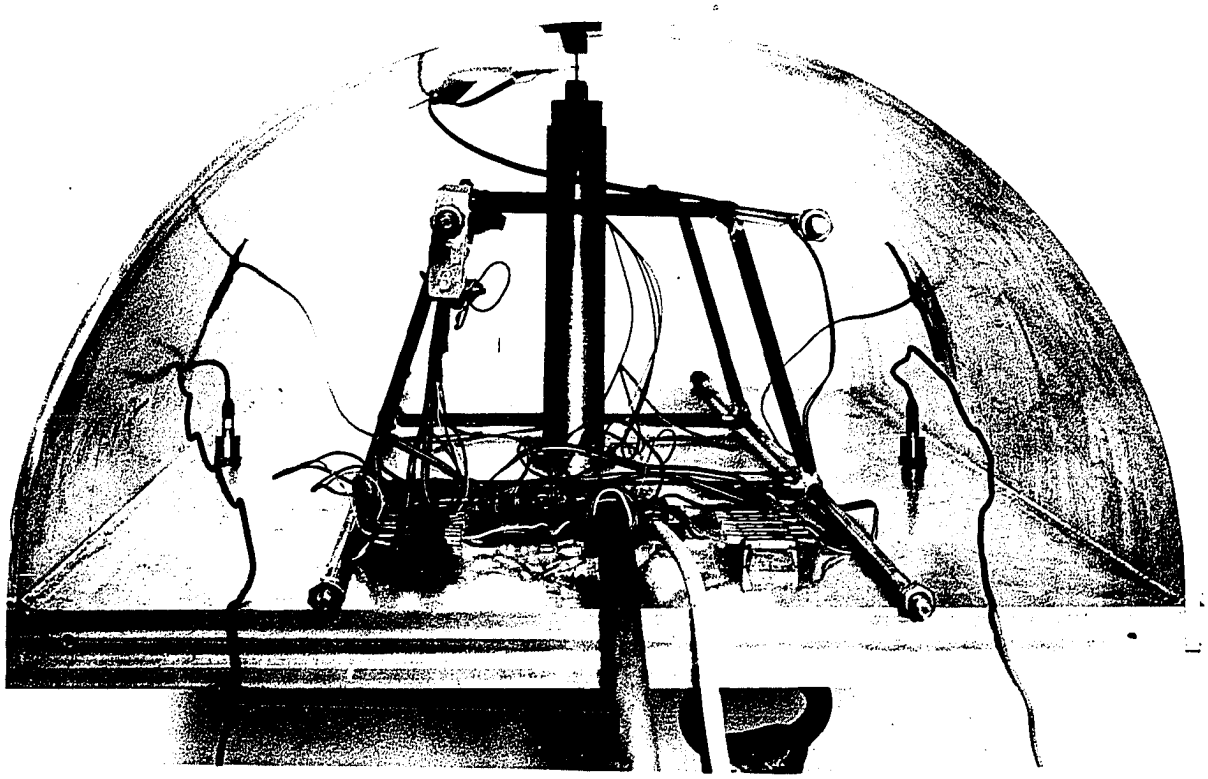

Figure B6. Fully instrumented 16-inch arch

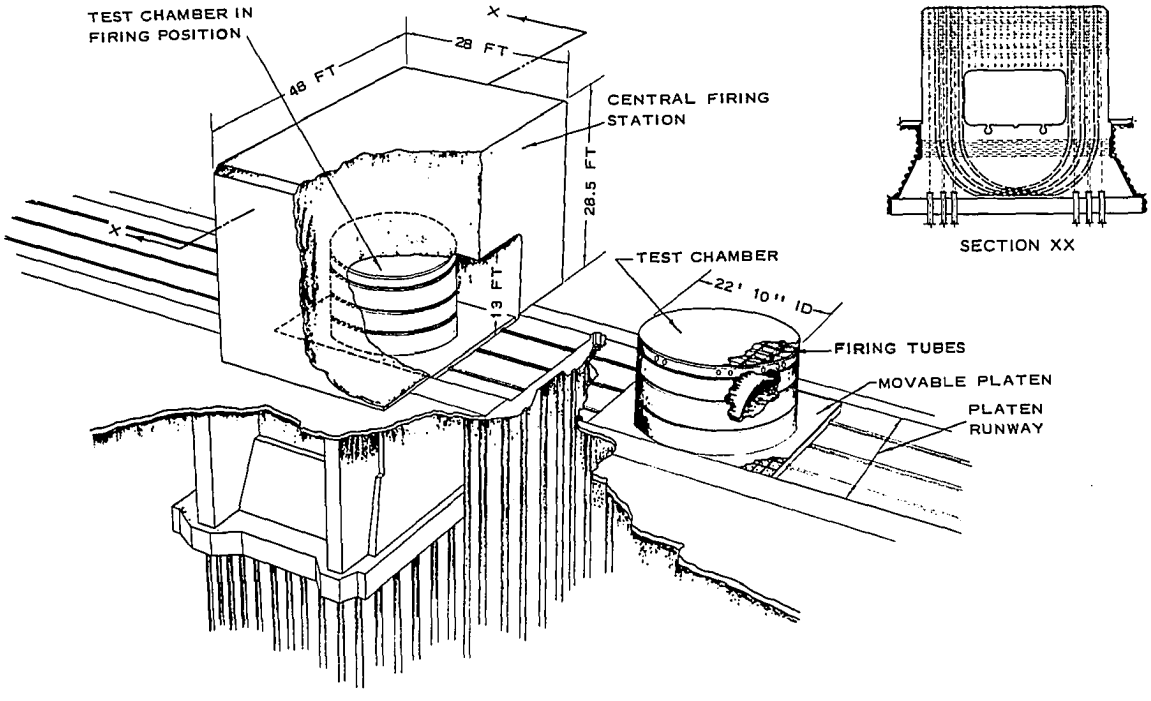

Figure B7. Large Blast Load Generator

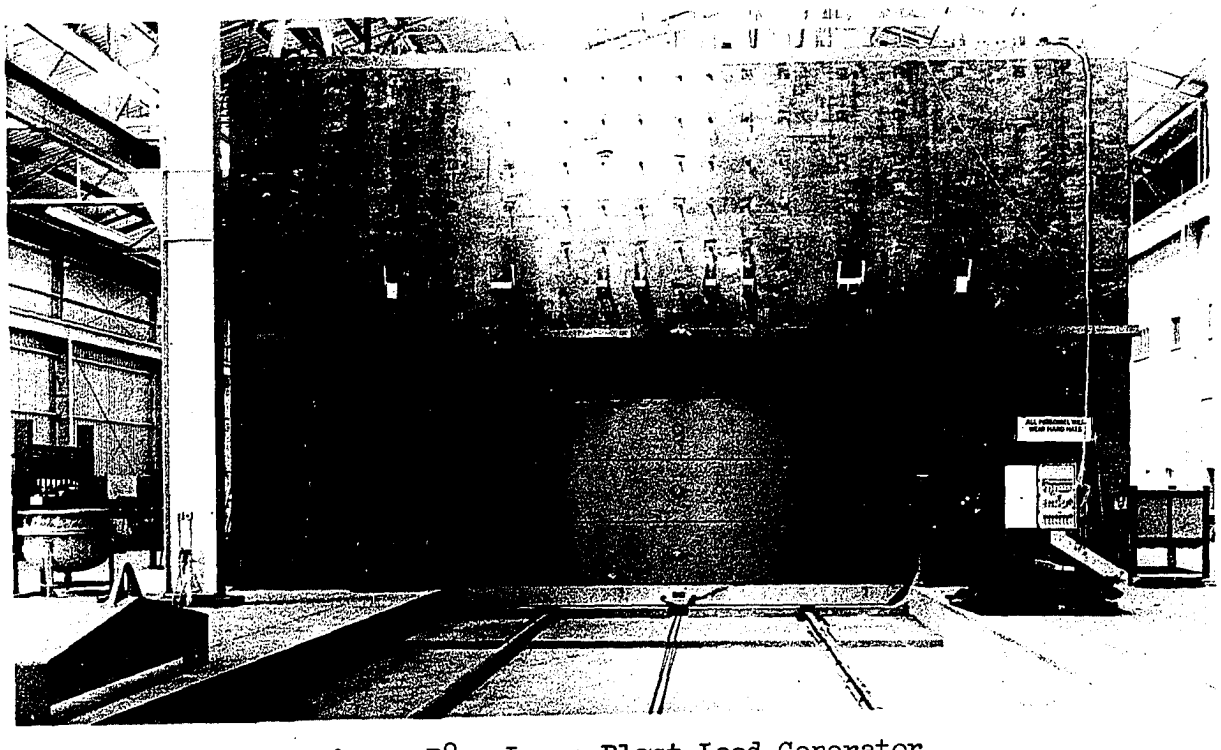

Figure B8. Large Blast Load Generator

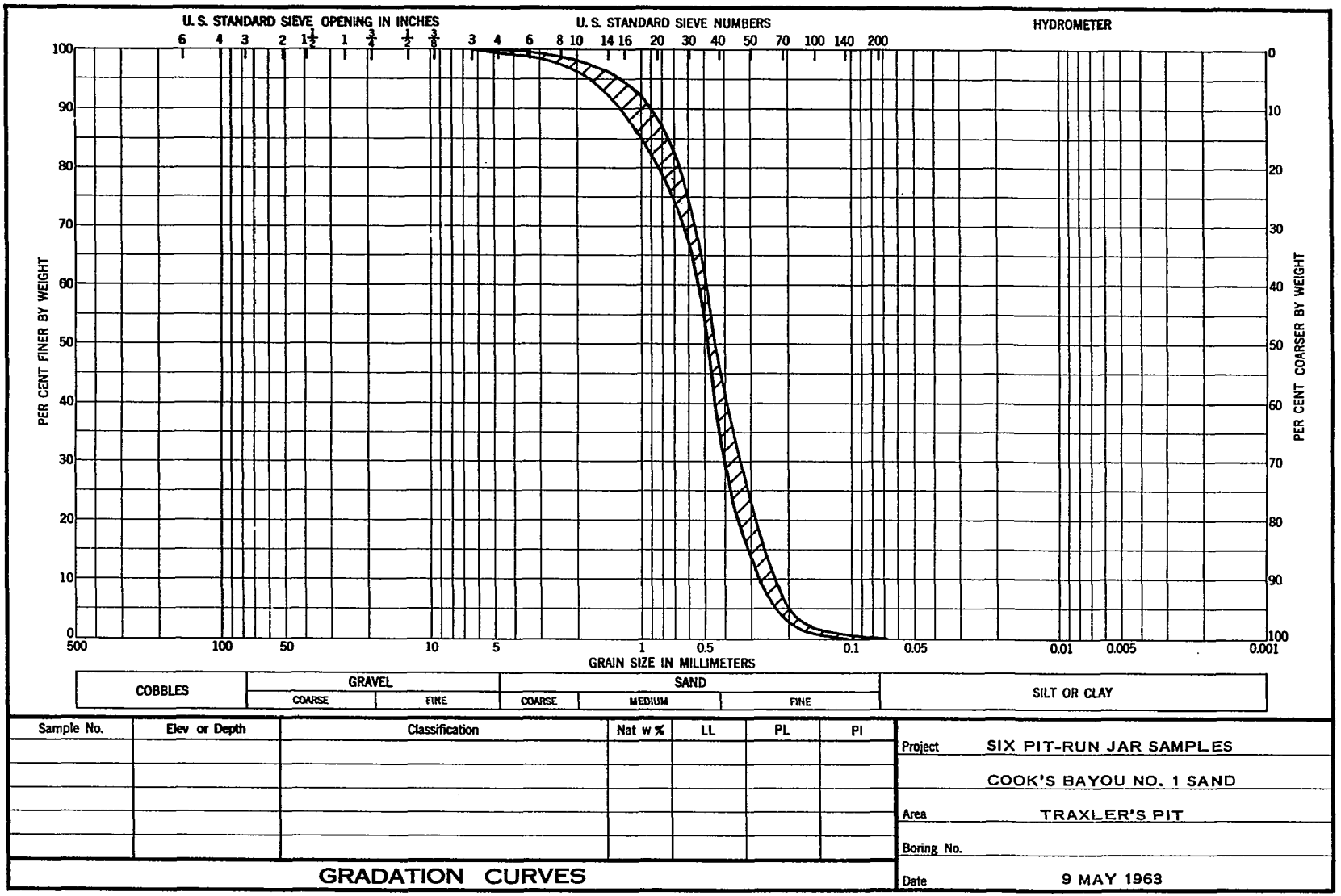

Sample No.	Elev or Depth	Classification	Nat w %	LL	PL	PI

GRADATION CURVES

Project: SIX PIT-RUN JAR SAMPLES
COOK'S BAYOU NO. 1 SAND
Area: TRAXLER'S PIT
Boring No.
Date: 9 MAY 1963

Figure B9. Grain-size distribution

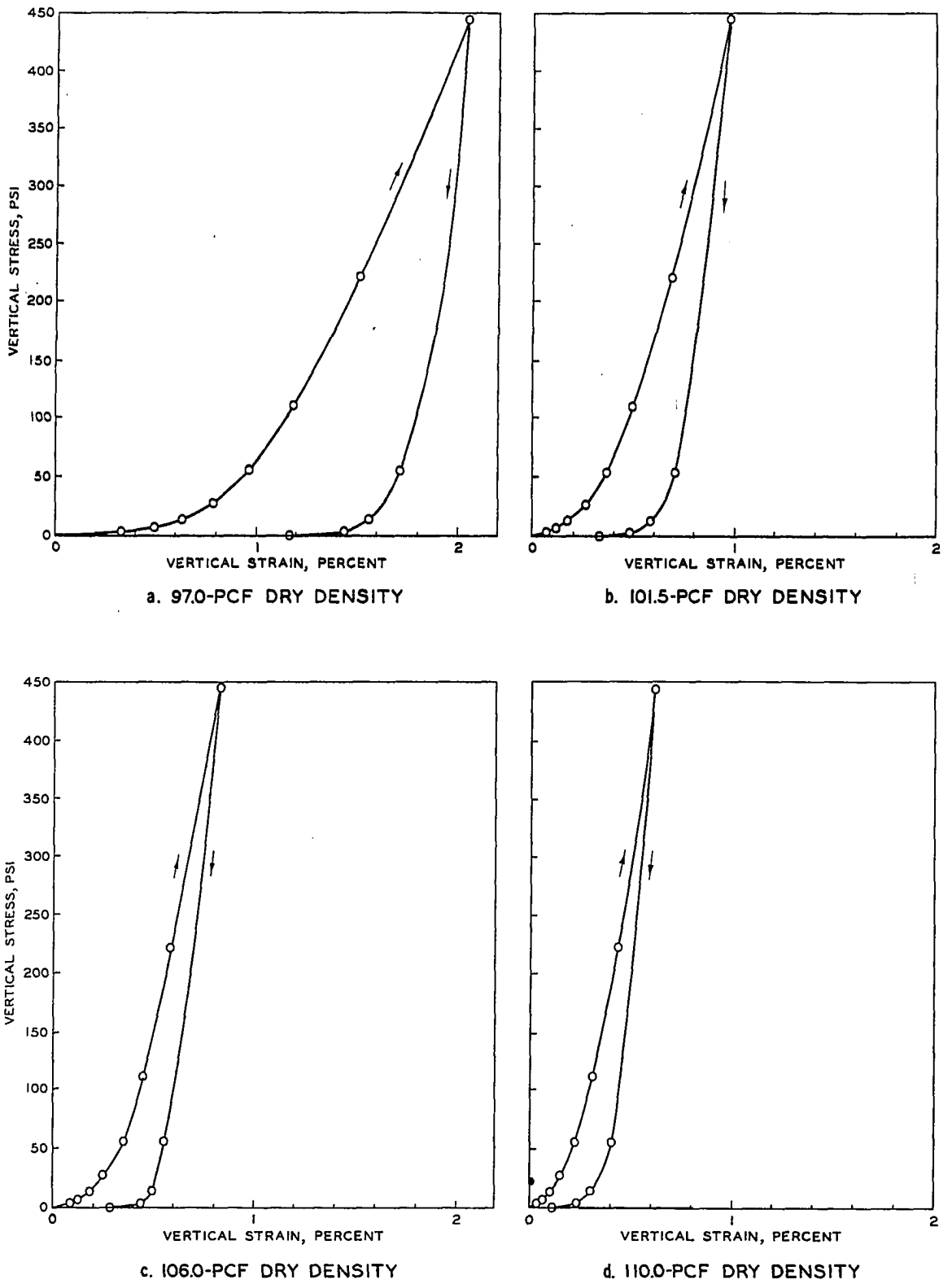

Figure B10. One-dimensional compression stress-strain curves for Cook's Bayou No. 1 sand

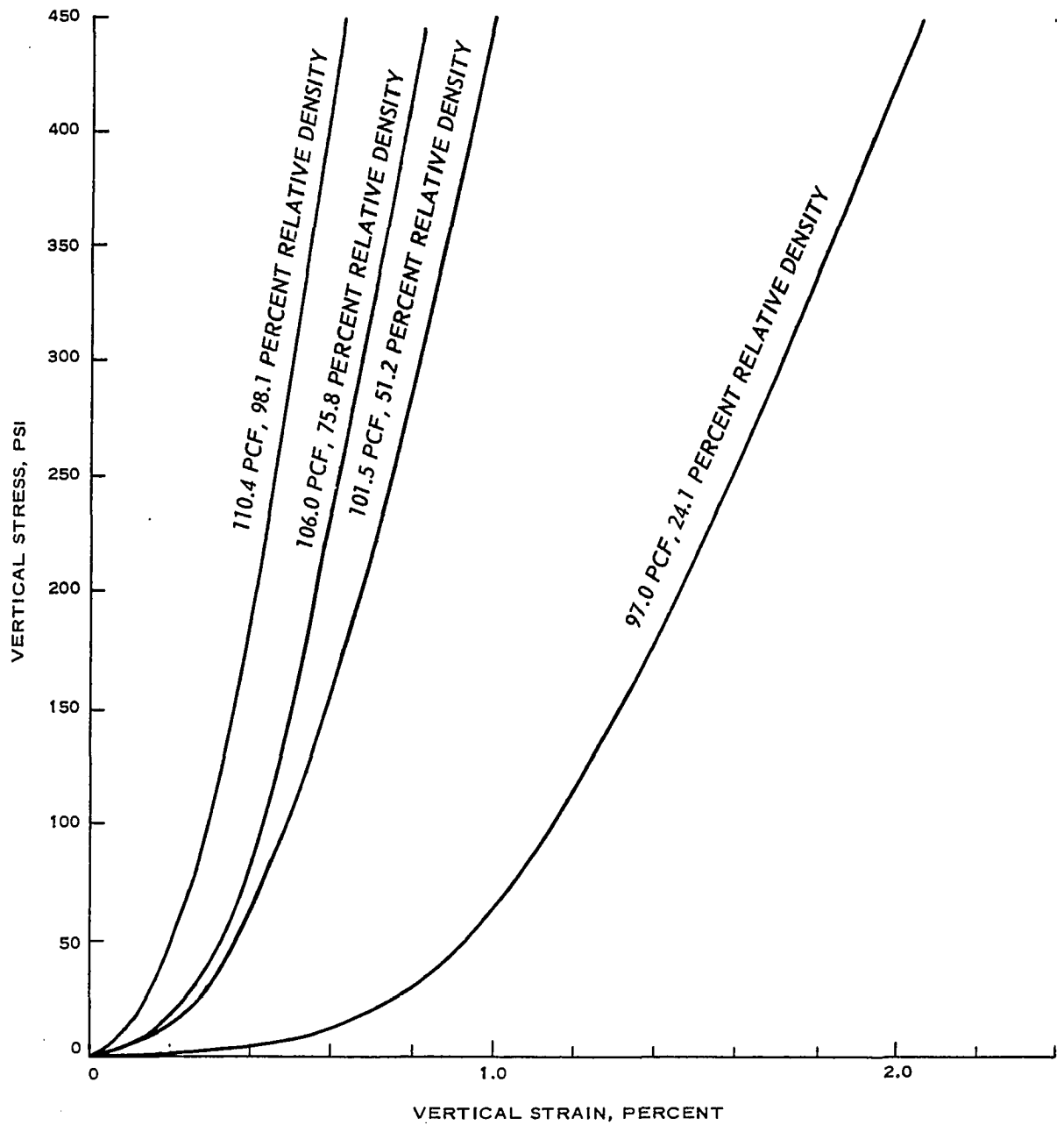

Figure B11. Comparison of one-dimensional compression stress-strain curves

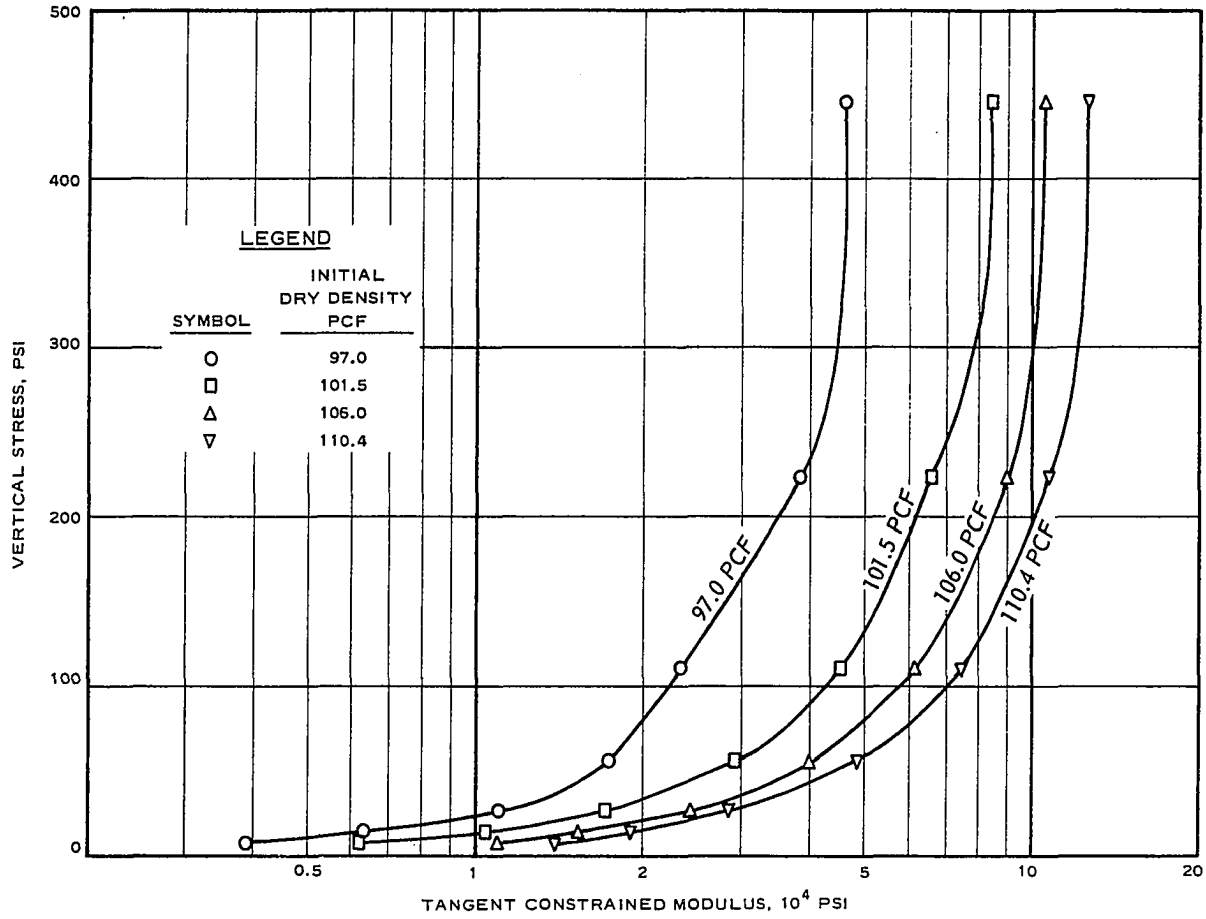

Figure B12. Tangent constrained modulus versus vertical stress, one-dimensional compression

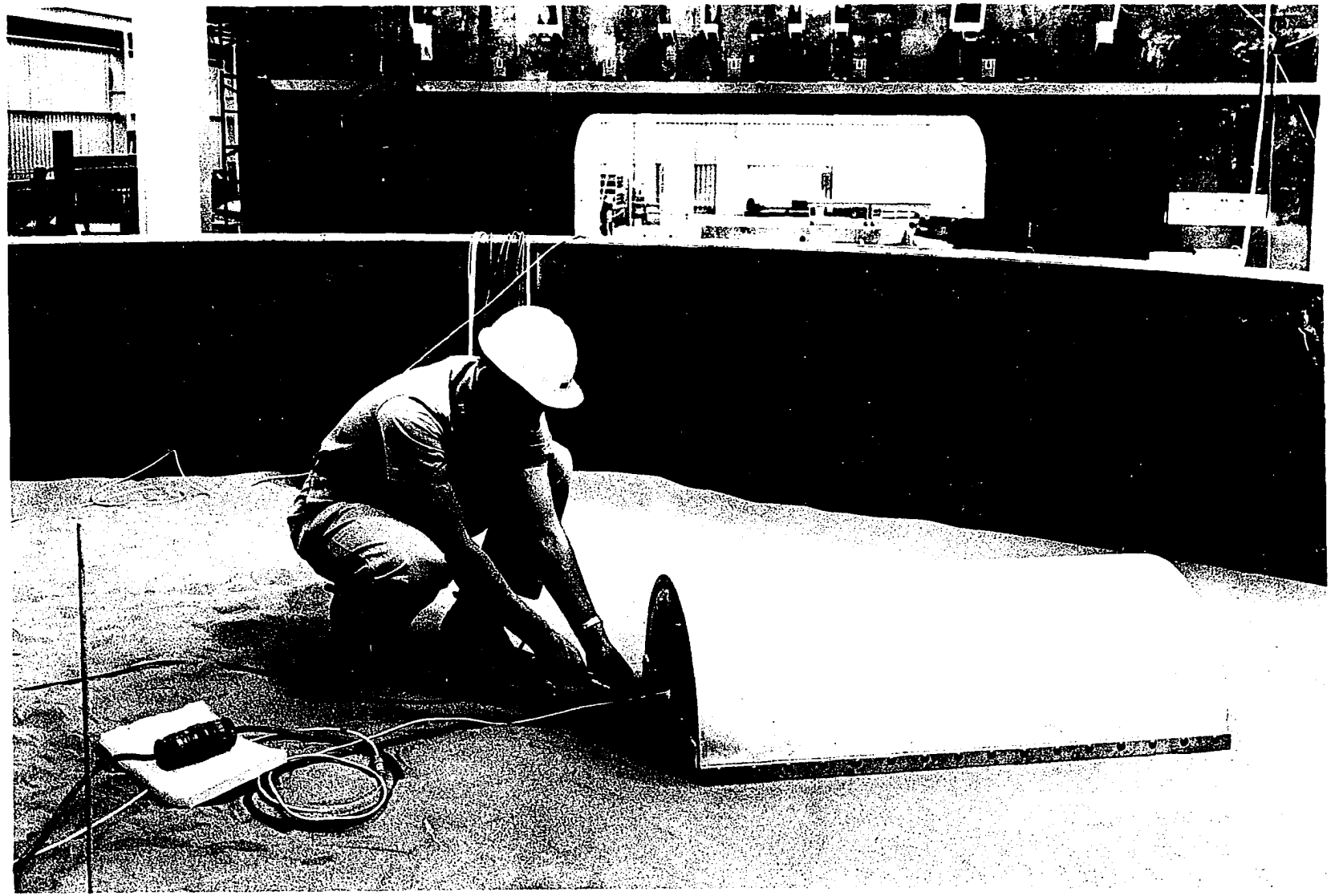

Figure B13. 24-inch arch in LBLG test chamber

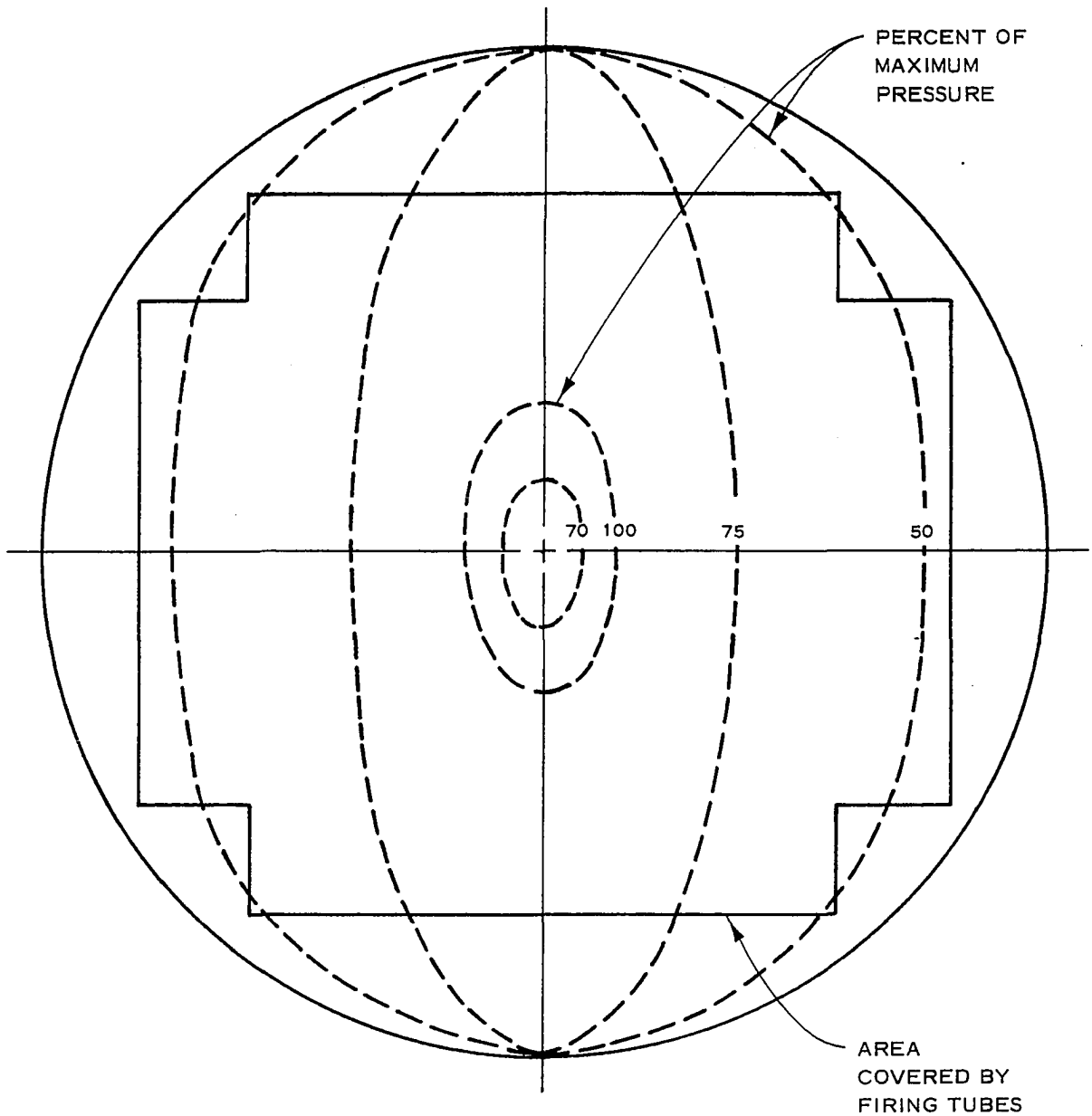

Figure B14. Peak surface pressure profile, LBLG

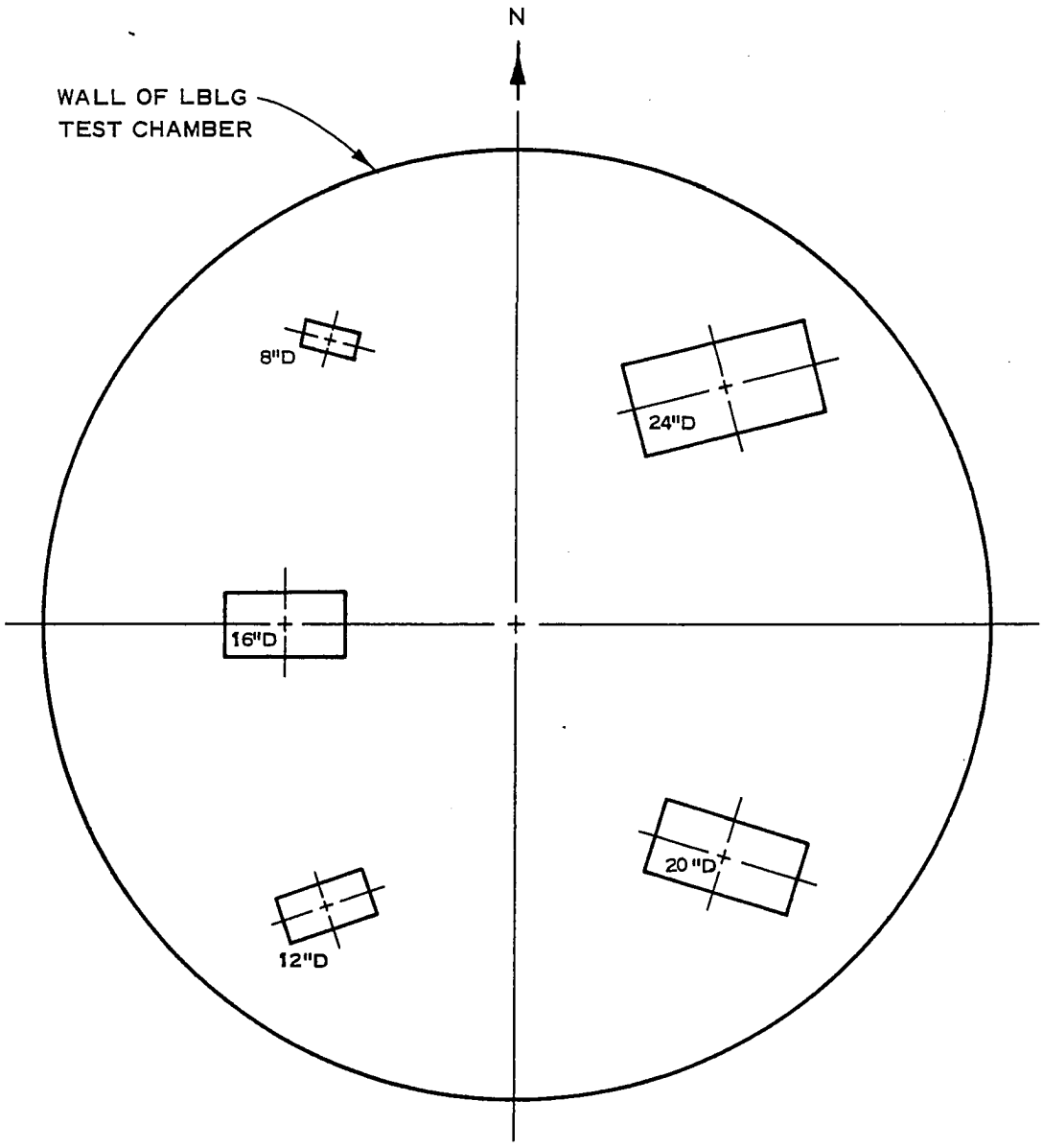

Figure B15. Plan view of arches in LBLG test chamber, Series I and II

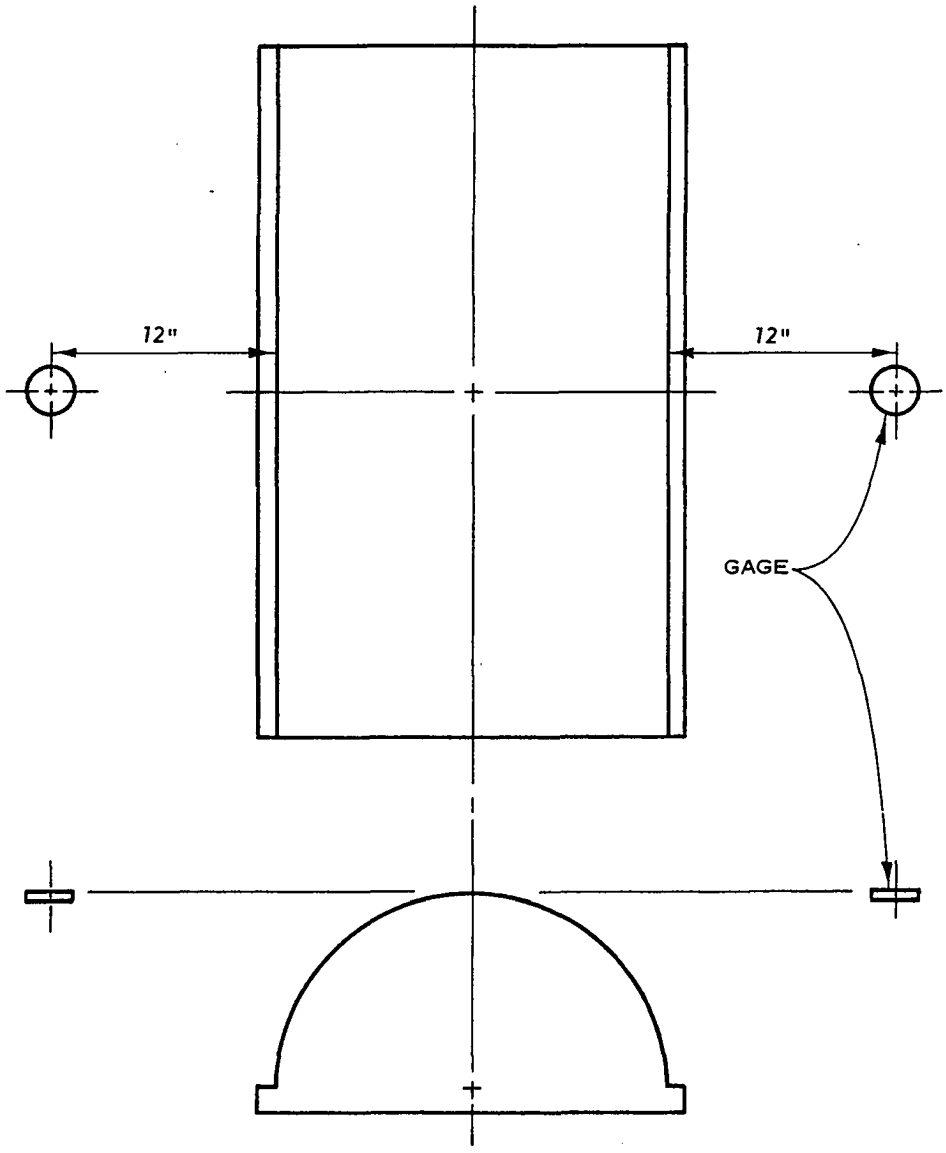

Figure B16. Location of buried soil pressure gages in vicinity of each structure

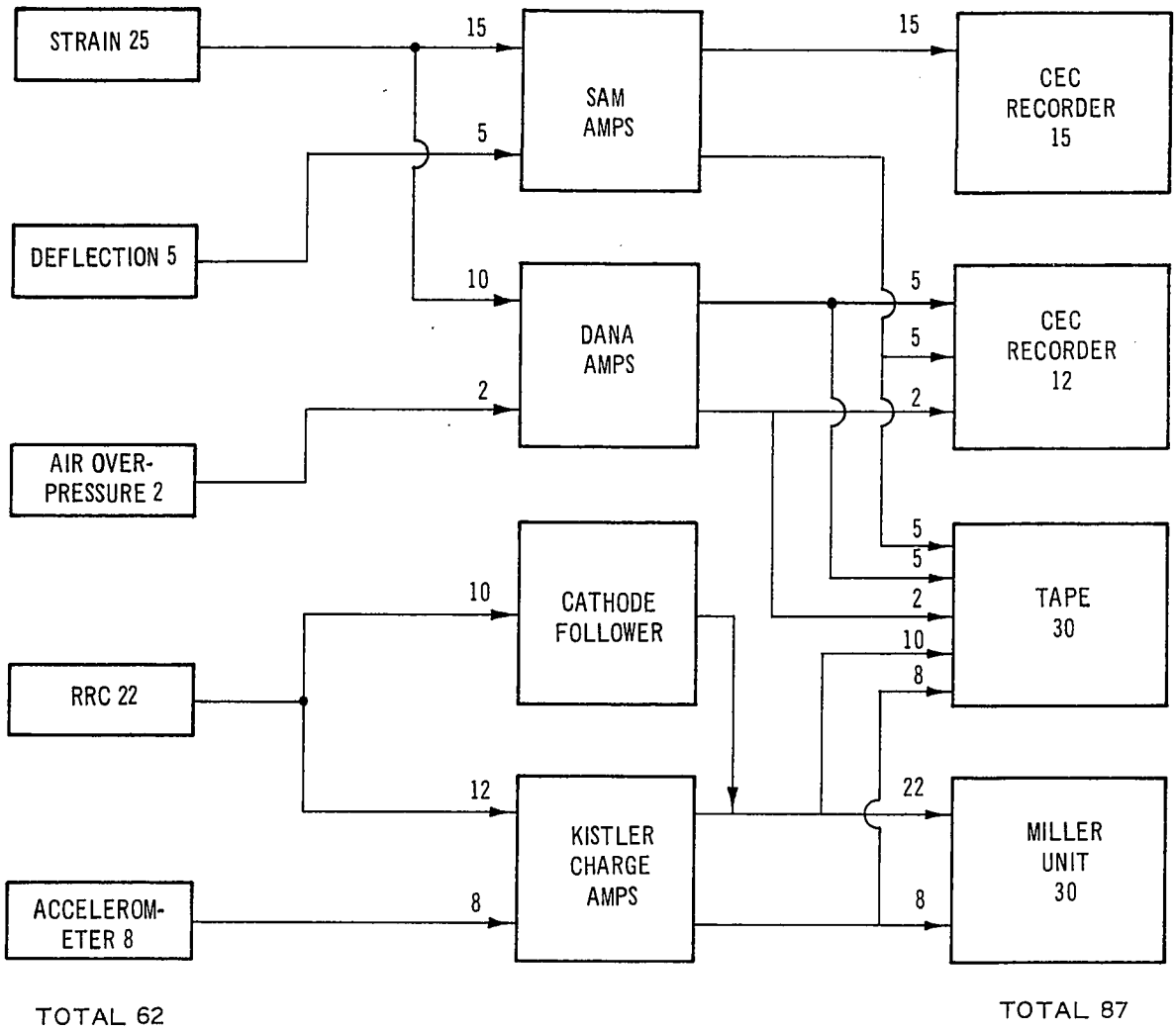

Figure B17. Schematic of typical instrumentation

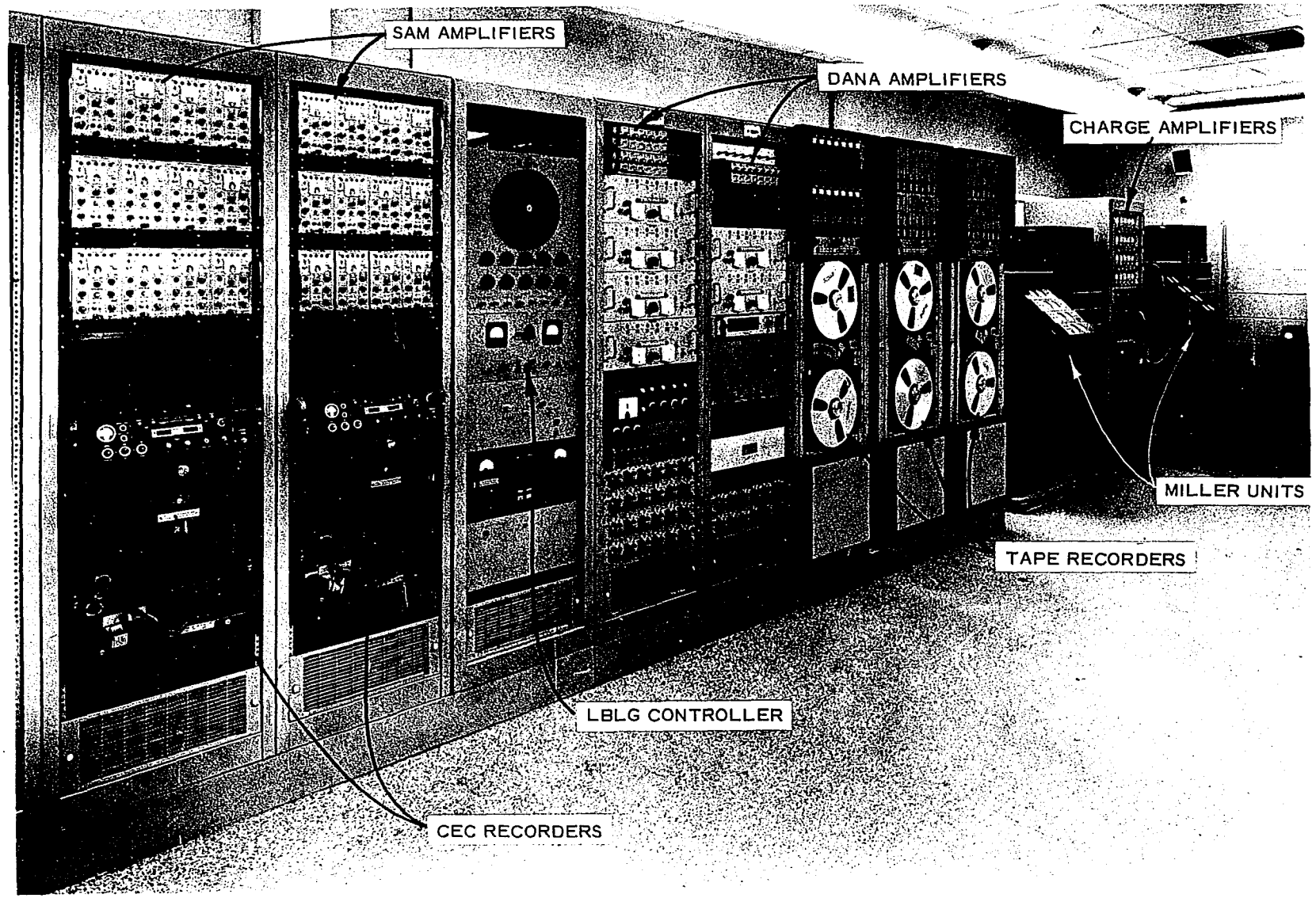

Figure B18. Instrumentation equipment

APPENDIX C: PILOT TEST PROGRAM

A. Purpose

It was deemed necessary to undertake a limited pilot test program prior to actually conducting LBLG tests on the five principal models. The primary objectives of the pilot test program were:

1. To confirm that the design of the arch structure was practical.

2. To determine the feasibility of repeated dynamic loadings on the same specimen.

3. To determine the extent to which test results could be duplicated.

4. To gain experience in installation techniques and instrumentation procedures.

5. To investigate the mode and magnitude of structural response in strain and deflection for the purpose of designing the instrumentation for the principal model structures.

It was felt that these objectives could be accomplished with a limited effort consisting of several static and dynamic tests conducted in the Small Blast Load Generator (SBLG) on a pilot model arch structure.

B. Structures and Instrumentation

Two series of tests were conducted, Pilot Series I and Pilot Series II. The basic structure was an 8-inch-diameter, 8-inch-long aluminum (6061-T6) arch with a roof thickness of 0.100 inch (D/t = 80). For Series I, the floor was a 1/4-inch-thick aluminum plate with a simple

springing line joint (Figure C1). The Series II model had a 1/2-inch-thick aluminum plate floor with a grooved springing line joint, similar to the joint subsequently employed for the principal models. The same roof piece and instrumentation were used for both series. Strain gages denoted a through f were mounted tangentially on the inside of the arch at its midlength (Figure C2). A longitudinal strain gage, cℓ , was mounted at the crown to detect lengthwise bending. A Collins deflection gage was mounted between the roof and floor at the center of the arch, and two accelerometers were fixed to the floor. Figure C3 shows the fully instrumented Series I pilot model. Endwalls for the pilot model were identical with those subsequently used for the principal models and described in Appendix B.

It should be added that it would have been desirable to have installed strain gages on the outside of the pilot structure, "back-to-back" with those used on the inside, for the purpose of determining moment and thrust at these sections. However, in the interests of time, economy and simplicity of installation and instrumentation, it was decided to forego this additional effort since it was not essential to the objectives of the pilot test program.

C. Small Blast Load Generator (SBLG)

The SBLG is a test facility which is capable of generating static loads up to 500 psi and dynamic overpressures up to 250 psi. Three foundation configurations are available, two with a rigid bottom and one "infinite" (9-foot-deep) hole (Figure C4). The test chamber is 4 feet in diameter and variable in depth, with stacked rings available for

providing depths of up to 8 feet above the floor.

When dry sand is used as a test medium, it is normally placed by the showering technique which is currently employed at a number of laboratories. The equipment used with the SBLG consists of a large hopper with 14 flexible hoses which allow the sand to be showered through a 1/2-inch-mesh screen into the SBLG (Figure C5). By adjusting the direction of flow of each flexible hose, a uniformly plane specimen can be built up in the SBLG as the entire hopper assembly is rotated at about 25 turns per minute. Experience has shown that dense, dry sand specimens of very uniform density ($\pm$0.5 pcf or better) can be achieved in this manner.

D. Pilot Series I

Pilot Series I consisted of a static bench test on the structure under a uniform line load along the crown, followed by three dynamic tests on the structure buried in sand in the SBLG. As a result of the static bench test, it was decided to modify the floor plate to gain better end fixity.

The Series I SBLG tests were intended to determine the feasibility of repeated loading and to gain an idea of the structural response to be expected. It was realized that there was a possibility that the dynamically loaded structure might move within the medium due to the density mismatch, since this occurrence had been previously observed in similar tests (19). This would most likely preclude repeated loading of the same specimen. To determine structural displacement, the sand medium was layered with black grid lines at 2-inch intervals, from the base of the structure to a depth 2 inches above the crown, for a total of four grid lines. This was done by sprinkling a sand-lampblack mixture on a freshly

prepared lift, as shown in Figure C6. Upon completion of the SBLG testing, the entire specimen was soaked in water for 36 hours, at which time the saturated sand could be cleanly sliced in a vertical plane to reveal a section of the grid lines and the position of the structure.

In addition to the grid lines, a means of monitoring the position of the buried structure between loadings was provided. Fine, stiff piano wire "antennae" were fixed to the four corners of the arch floor (Figure C6). These antennae extended vertically to protrude about 1 inch above the surface of the medium. By measuring the protruding length between tests, it was possible to detect any appreciable vertical shift in structure position and/or densification of the medium.

The Series I structure was buried to a depth of 7-3/4 inches above the crown in dense, dry Cook's Bayou sand. The installation consisted of showering sand into the SBLG to a depth of 2 feet, placing the structure in the center of the level surface and continuing to shower sand to a total specimen depth of 3 feet. The flow of sand from the flexible nozzles was directed so that a minimum amount fell directly onto the arch. In this manner, the specimen was built up in continuously plane horizontal layers. Frequent monitoring of the sand surface indicated that the surface was plane to within $\pm 1/4$ inch at all times. A 1/16-inch-thick rubber membrane was placed over the final surface to prevent gas pressure from entering the soil pores, and holes were punched in the membrane to allow the antennae to protrude. Static and dynamic air overpressures in the SBLG loading bonnet were recorded by two pressure transducers located in the wall of the bonnet. After two initial static preloads of 50 psi had been applied, three dynamic shots were conducted

at a nominal peak overpressure of 65 psi.

The antennae were monitored between each shot. After the static preloads, the distance from the surface of the membrane to the arch floor had decreased by about 1/32 inch, which was at or near the limit of observational error. After the entire series, this distance had decreased by a total of about 1/16 inch. This was attributed to probable densification of the soil cover rather than residual structure displacement, and amounted to about 1/2% strain.

After the Series I tests were completed, the membrane was removed and the dry sand medium was saturated and sliced. Figures C7 and C8 show the grid lines and structure. There was no apparent residual displacement of the structure nor disturbance of the grid lines. It was concluded as a result of this observation that repeated loadings on the buried arch with a membrane covering the sand surface did not alter the geometry of the installation, and that the only significant effect upon the medium was a possible densification of the sand. Density samples were not taken during this series, but experience with similar specimens has indicated that, even after repeated loadings, the maximum increase in sand density is not likely to be more than about 1 pcf.

The response of the Series I structure to the three dynamic shots was recorded, and peak strains and deflections are shown in Table C1. The mode of response was the same for each shot, and appeared to be a symmetrical compression mode. The peak strains and deflections were duplicated reasonably well. The maximum deviation of any peak strain from the three-shot average was smaller for the higher values of peak strain, indicating that experimental error is likely to be larger for smaller values of peak

strain. As a result of Series I, it was decided to continue with a somewhat more extensive pilot test program.

E. Pilot Series II

The Series II structure differed from the Series I structure only in the springing line joint (Figure C1). The Series II structure underwent a static bench test in which its response was compared with that predicted theoretically from analysis of a fixed-end arch. The structure was loaded with a uniform line load as shown in Figure C9, with P varying from zero to 400 pounds. Strain was recorded on gages a through e, and a plot of strain versus load for each gage resulted in a straight line with slope $\frac{\epsilon}{P}$ $(\frac{\mu in./in.}{lb})$.

The theoretical tangential strain per unit load $\frac{\epsilon}{P}$ was then calculated (Appendix D). A plot of the theoretical $\frac{\epsilon}{P}$ curve appears in Figure C10, along with the experimental values for $\frac{\epsilon}{P}$ observed in two tests on the Series II pilot model for $\theta = 0^{\circ}$, 45° and 87.5° . It was concluded that the Series II pilot model comprised a reasonably good representation of a fixed-end arch for the crown loading up to $P = 400$ pounds.

The observed Collins gage deflection was 136×10^{-6} inches per pound of load P . This compared reasonably well with the theoretical value (Appendix D) of 112×10^{-6} inches per pound for a fixed-end arch. The experimental value errs on the high side, as would be expected due to lack of perfect end fixity.

For the Series II SBLG pilot tests, the structure was installed just as in Series I except that no grid lines were utilized. Two of the

antennae were retained to monitor the effect of repeated loading on depth of burial. The Series II SBLG tests consisted of 13 dynamic shots and two subsequent static loadings. Shots 1 through 6 were at a nominal peak overpressure of 65 psi; shots 7, 8 and 9 at 130 psi; shots 10 and 11 at 100 psi; and shots 12 and 13 at 65 psi. Tests 14 and 15 were static loadings to 100 psi. The peak strains and deflections observed on shots 3 through 13 are presented in Tables C2 through C5. The records from shots 1 and 2 were ruined during chemical processing and no data for these shots are available.

The degree to which structural response at a given overpressure could be duplicated between shots was determined by the maximum deviation of peak response on any shot from the average peak response for all shots at the same overpressure. The percent maximum deviation is shown in Tables C2 through C5 for each data channel. Peak tangential strains were duplicated to within about $\pm 8\%$ or better in all 23 cases where multiple data were available, and to within $\pm 4\%$ or better in 15 of 23 cases. In general, better reproducibility was obtained for the higher values of peak strain. Deflections were duplicated to within about $\pm 7\%$ or better in all four cases. It was concluded that, after the installation had been "shaken down," or consolidated, by several dynamic loads, two or three shots were adequate to produce reliable representative peak response data for a given overpressure. It was hoped that the same condition would be experienced in the LBLG tests.

The variation of peak strain with peak surface overpressure is shown in Figure C11. Peak tangential strains at b , c and d and peak longitudinal strain at $c\ell$ appeared to relate linearly to peak overpressure.

Regarding peak tangential strain at a , e and f , the downward turning response curves are probably due to a lack of perfect end fixity between the roof and floor pieces. The nonlinear effect of this joint rotation is discussed for the static bench tests on the principal models in Section IV of the main text.

Evidence of the dynamic nature of the structural response appears in Figure C12, which is a typical record of strain obtained from a dynamic shot. The sharp peaks at 4.5, 8, 12 and 16 msec are due to motion of the entire SBLG test chamber and the subsequent inertial load on the structure. These peaks were neglected in interpreting the structural response to the incident shock wave. Apparent vibration of the arch roof after 20 msec may be detected from the traces of strain gages b and d , and the same vibration but of lesser amplitude appears in traces c and e . This vibration was evident to some degree on every shot. In each case, following the early dynamic response, the frequency of vibration observed was 550 $\pm$ 5 cps, corresponding to a natural period of 1.82 msec. This value agrees rather well with that derived from the WES Equivalent Surcharge Loading Method (9) for the buried arch (Appendix D). No claim is made as to the validity of that method, however, on the basis of observations on the single installation.

The results of the two static load tests in Series II are shown in Figure C13, which represents a composite of the two static tests. The mode of response in the static tests was the same as under dynamic loading, a symmetrical compression mode. However, the static response for a given overpressure was consistently less than the dynamic response. Table C6 compares the ratio of strain per unit overpressure, $\frac{\epsilon}{p_o}$, for

the static and dynamic tests. This parameter was calculated from Figures C11 and C13 as the slope of the best straight line fit, in the 60- to 130-psi range of Figure C11 (dynamic) and in the 20- to 100-psi range of Figure C13 (static). The ratio of the dynamic $\frac{\epsilon}{p_o}$ to that under static load is termed the dynamic load factor (DLF). It is noted that this factor ranged from 1.2 to 1.7 depending on the location on the structure.

The deflection of the arch crown with respect to the floor was recorded by the Collins gage in all tests. Figure C14 indicates this deflection for the static and dynamic loadings. The probable effect of rotation in the joint between the arch roof and floor is evidenced by the downward-turning static curve, which was identical for the two tests. It is noted, however, that the peak dynamic deflections were disproportionately greater at the higher overpressures. It would be difficult to place with any confidence a physical interpretation on the form of the dynamic deflection-overpressure curve based on the limited data.

The two antennae indicating structure depth were monitored throughout the Series II tests. The total change in depth between initial installation and completion of all loading was 1/8 inch for both wires, amounting to about 1% strain. This small change after 13 dynamic and two static loadings supported the belief that repeated loadings were practical.

F. Conclusions

The pilot tests satisfied the purposes for which they were intended, and additionally provided information of value to understanding some of the phenomena which affect the response of such a structure. Specifically, the following conclusions were drawn with regard to the

stated primary objectives of the pilot tests:

1. The Series I floor and springing line joint was inadequate. The Series II configuration provided a structure which could be considered a good representation of an arch roof rigidly fastened to a floor slab.

2. Dynamic loadings on the same specimen could be repeated without concern for a drastic change in geometry or material conditions, especially after the specimen had experienced an initial loading or series of loadings.

3. Test results could be duplicated with a relatively high degree of accuracy. It was hoped that during the principal tests in the LBLG no more than two shots at a given overpressure would suffice to generate reliable data.

4. Installation of sand by showering appeared to create a relatively uniform sand density, both in the vicinity of the structure and in the free field. There appeared to be no major difficulties in instrumentation, data recording or data reduction.

5. For a depth of burial of one diameter, overpressure in the 50- to 150-psi range generated strains and deflections of a readily measurable magnitude.

Table C1. Pilot Series I structural response

(C = compression, T = tension)

	Shot 1	Shot 2	Shot 3	Ave. 3 shots	Max. % deviation from ave.
Peak bonnet overpressure→ (psi)	63	66	64	64.3	2.5
		Peak dynamic strain (μin./in.)			
Gage a	600C	610C	585C	598C	2.0
Gage b	140C	170C	180C	163C	14.1
Gage c	205C	175C	175C	185C	10.8
Gage d	180C	180C	210C	190C	10.5
Gage e	600C	630C	650C	627C	4.3
Gage f	340T	335T	280T	318T	10.0
Gage $c\ell$	15T	22T	44T	27T	62.0
Peak deflection (inches)	0.0356	0.0319	0.0258	0.0311	17.0

Table C2. Peak response, shots 3-6, Pilot Series II

(C = compression, T = tension)

Gage	Shot 3	Shot 4	Shot 5	Shot 6	Ave. 4 shots	Max. % deviation
Pressure 1 (psi)	68	68	68	68	65	4.6
Pressure 2 (psi)	62	62	62	63		
Strain a $\left(\frac{\mu in.}{in.}\ C\right)$	635	608	596	595	609	4.2
Strain b $\left(\frac{\mu in.}{in.}\ C\right)$	215	203	212	207	209	2.9
Strain c $\left(\frac{\mu in.}{in.}\ C\right)$	NR[a]	107	101	101	103	3.9
Strain d $\left(\frac{\mu in.}{in.}\ C\right)$	194	194	187	192	192	2.6
Strain e $\left(\frac{\mu in.}{in.}\ C\right)$	515	500	495	484	498	3.4
Strain f $\left(\frac{\mu in.}{in.}\ T\right)$	600	622	630	615	617	2.8
Strain $c\ell$ $\left(\frac{\mu in.}{in.}\ T\right)$	35	38	59	50	45	30.0
Deflection (inches)	.0188	.0192	.0181	.0171	.0183	6.5

[a]NR designates no record for this data channel.

Table C3. Peak response, shots 7-9, Pilot Series II

(C = compression, T = tension)

Gage	Shot 7	Shot 8	Shot 9	Ave. 3 shots	Max. % deviation
Pressure 1 (psi)	NR[a]	138	134	131	5.3
Pressure 2 (psi)	134	126	124		
Strain a $\left(\frac{\mu in.}{in.} C\right)$	952	965	990	969	2.2
Strain b $\left(\frac{\mu in.}{in.} C\right)$	420	402	427	416	3.4
Strain c $\left(\frac{\mu in.}{in.} C\right)$	207	183	183	191	8.4
Strain d $\left(\frac{\mu in.}{in.} C\right)$	379	385	375	380	1.3
Strain e $\left(\frac{\mu in.}{in.} C\right)$	904	915	903	907	0.9
Strain f $\left(\frac{\mu in.}{in.} T\right)$	920	935	980	945	3.7
Strain $c\ell$ $\left(\frac{\mu in.}{in.} T\right)$	67	77	81	75	10.6
Deflection (inches)	.0546	.0492	.0498	.0512	6.6

[a]NR designates no record for this data channel.

Table C4. Peak response, shots 10 and 11, Pilot Series II

(C = compression, T = tension)

Gage	Shot 10	Shot 11	Ave. 2 shots	% deviation
Pressure 1 (psi)	107	107	102	6.9
Pressure 2 (psi)	95	99		
Strain a $\left(\frac{\mu in.}{in.} C\right)$	935	838	886	5.5
Strain b $\left(\frac{\mu in.}{in.} C\right)$	343	295	319	7.5
Strain c $\left(\frac{\mu in.}{in.} C\right)$	132	NR[a]	132	--
Strain d $\left(\frac{\mu in.}{in.} C\right)$	318	274	296	7.4
Strain e $\left(\frac{\mu in.}{in.} C\right)$	804	685	744	8.1
Strain f $\left(\frac{\mu in.}{in.} T\right)$	897	823	860	4.3
Strain $c\ell$ $\left(\frac{\mu in.}{in.} T\right)$	60	54	57	5.3
Deflection (inches)	.0300	.0288	.0294	2.0

[a]NR designates no record for this data channel.

Table C5. Peak response, shots 12 and 13, Pilot Series II

(C = compression, T = tension)

Gage	Shot 12	Shot 13	Ave. 2 shots	% deviation
Pressure 1 (psi)	65	64	62	4.8
Pressure 2 (psi)	60	59		
Strain a $\left(\frac{\mu in.}{in.} C\right)$	666	653	660	1.0
Strain b $\left(\frac{\mu in.}{in.} C\right)$	213	221	217	1.8
Strain c $\left(\frac{\mu in.}{in.} C\right)$	86	94	90	4.4
Strain d $\left(\frac{\mu in.}{in.} C\right)$	192	201	196	2.3
Strain e $\left(\frac{\mu in.}{in.} C\right)$	525	528	526	0.3
Strain f $\left(\frac{\mu in.}{in.} T\right)$	755	740	748	1.1
Strain cℓ $\left(\frac{\mu in.}{in.} T\right)$	41	39	40	2.5
Deflection (inches)	.0224	.0194	.0209	7.2

Table C6. Static versus dynamic strain response

(C = compression, T = tension)

Gage	$\epsilon/p_o \left(\frac{\mu in./in.}{psi}\right)$ Static	Dynamic	DLF
c ($\theta = 0^o$)	1.0C	1.5C	1.5
b ($\theta = 45^o$)	2.2C	3.2C	1.4
d	1.8C	2.9C	1.6
a ($\theta = 87.5^o$)	4.7C	6.2C	1.3
e	5.4C	6.4C	1.2
f (floor)	3.3T	5.7T	1.7

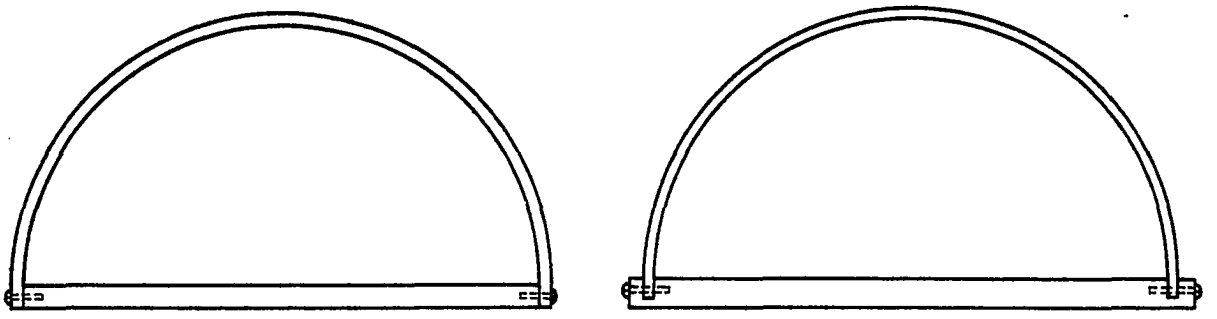

Figure C1. Pilot model configurations

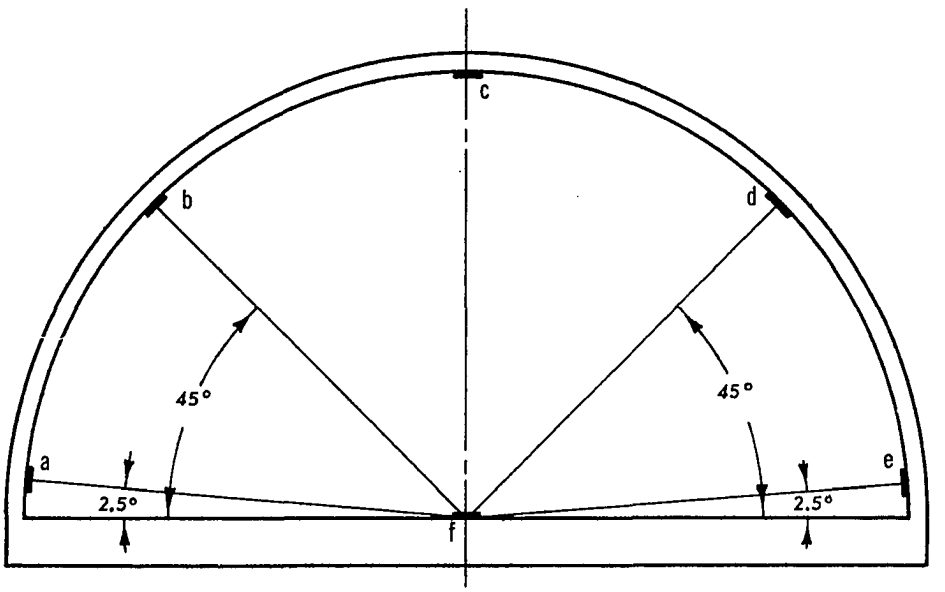

Figure C2. Pilot model strain gage array; section at midlength

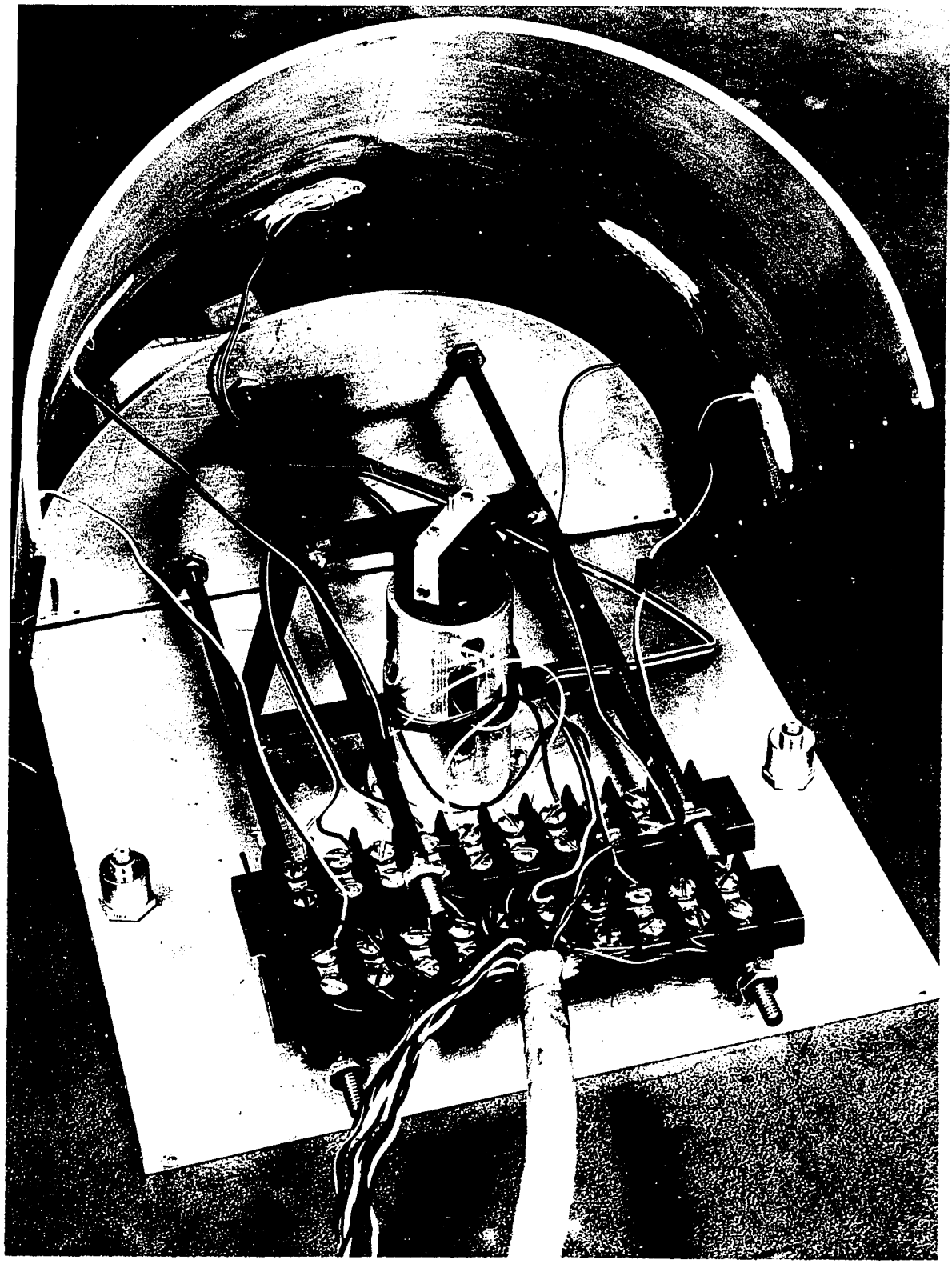

Figure C3. Instrumented Series I pilot model arch

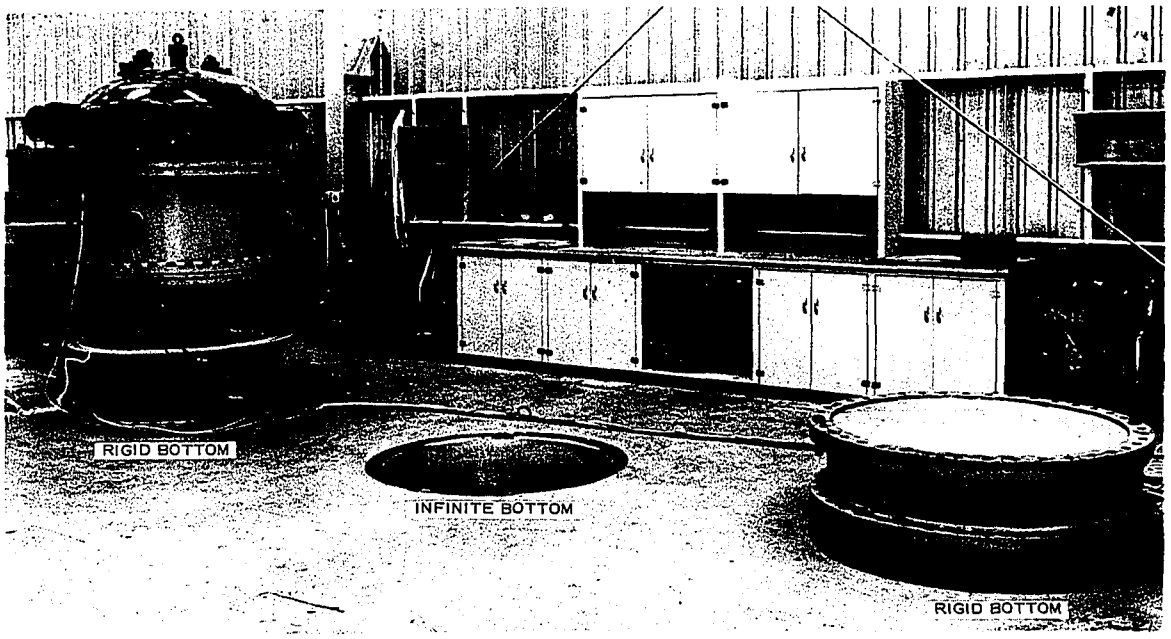

Figure C4. Small blast load generator

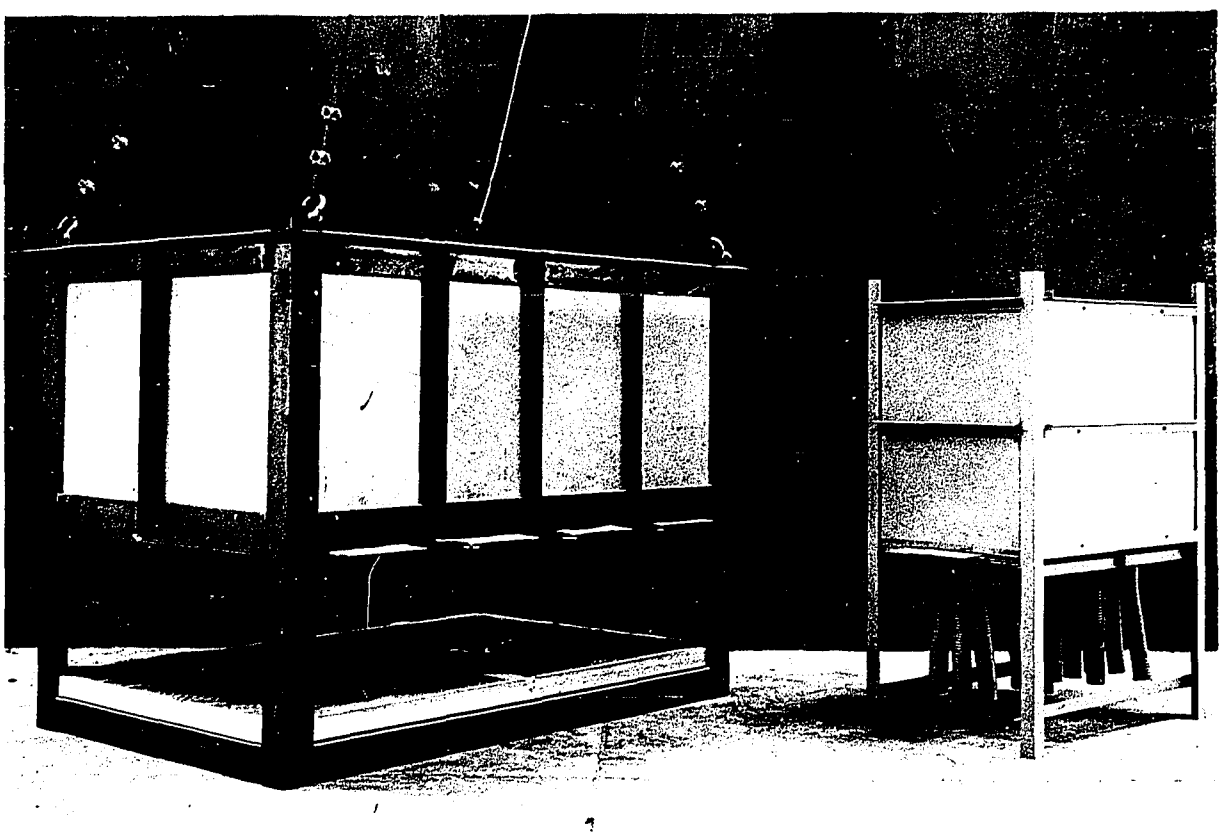

Figure C5. Sand sprinkling equipment for large blast load generator (left) and small blast load generator (right)

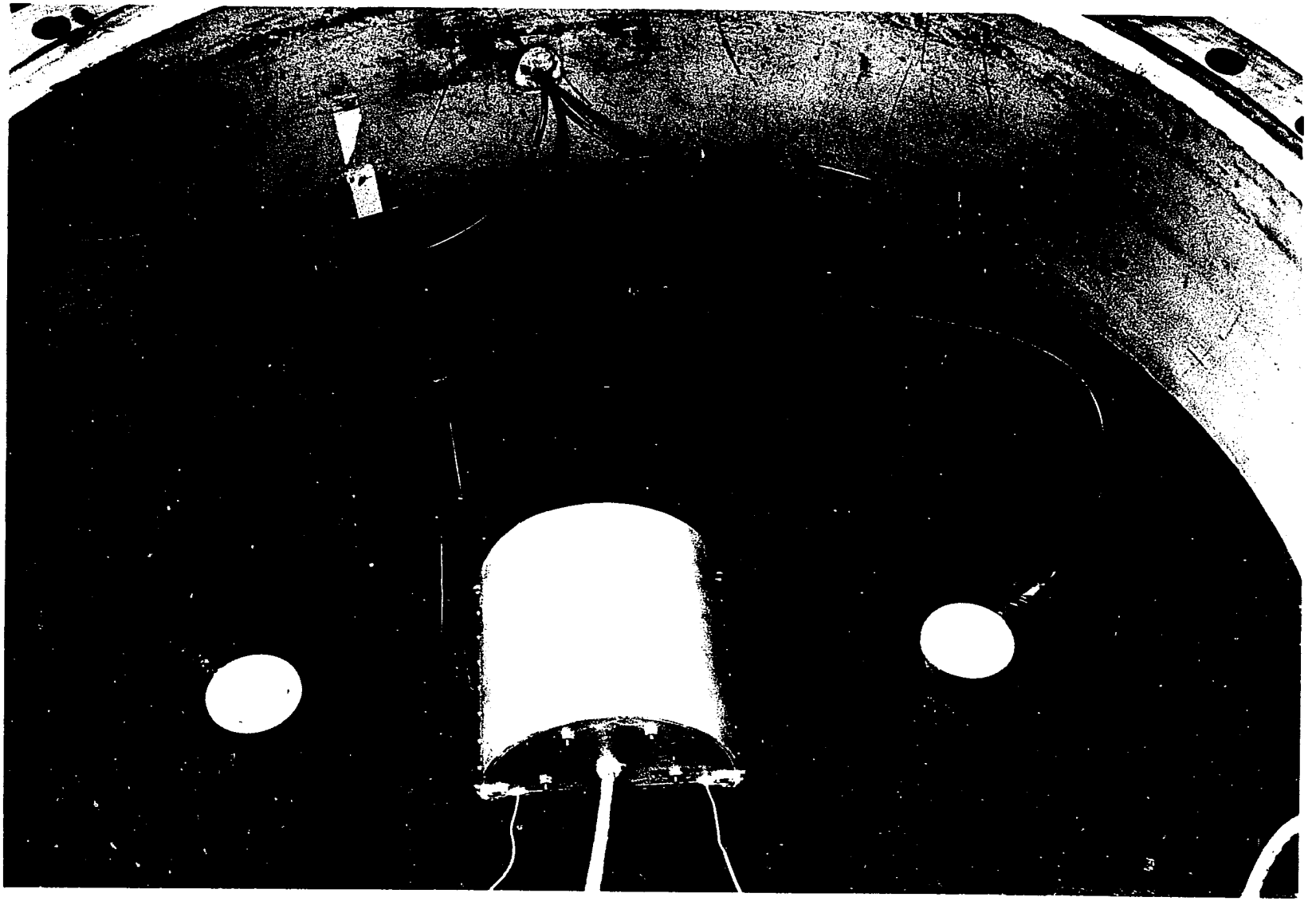

Figure C6. Pilot arch on blackened layer grid line

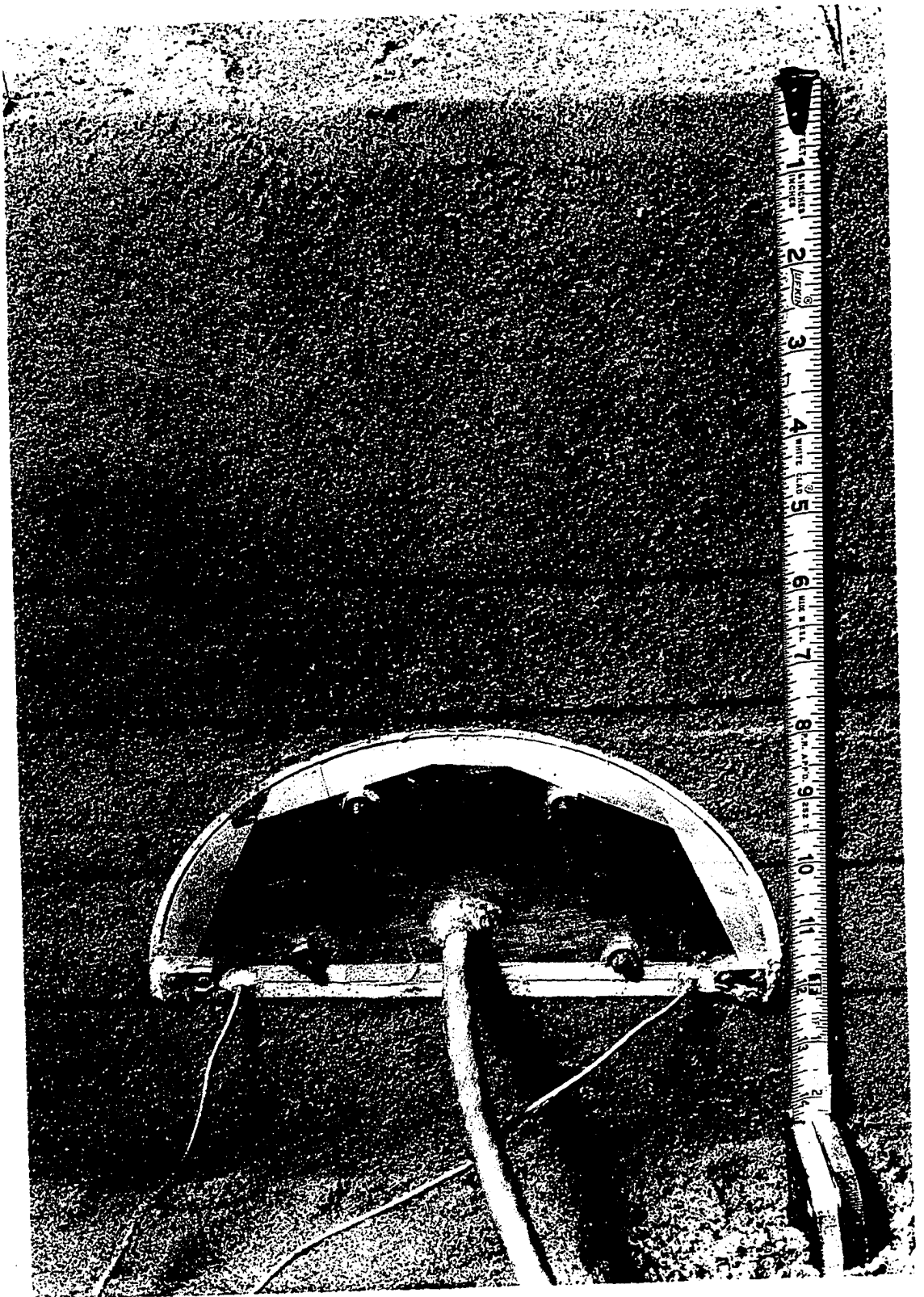

Figure C7. Pilot arch after Series I tests showing grid lines

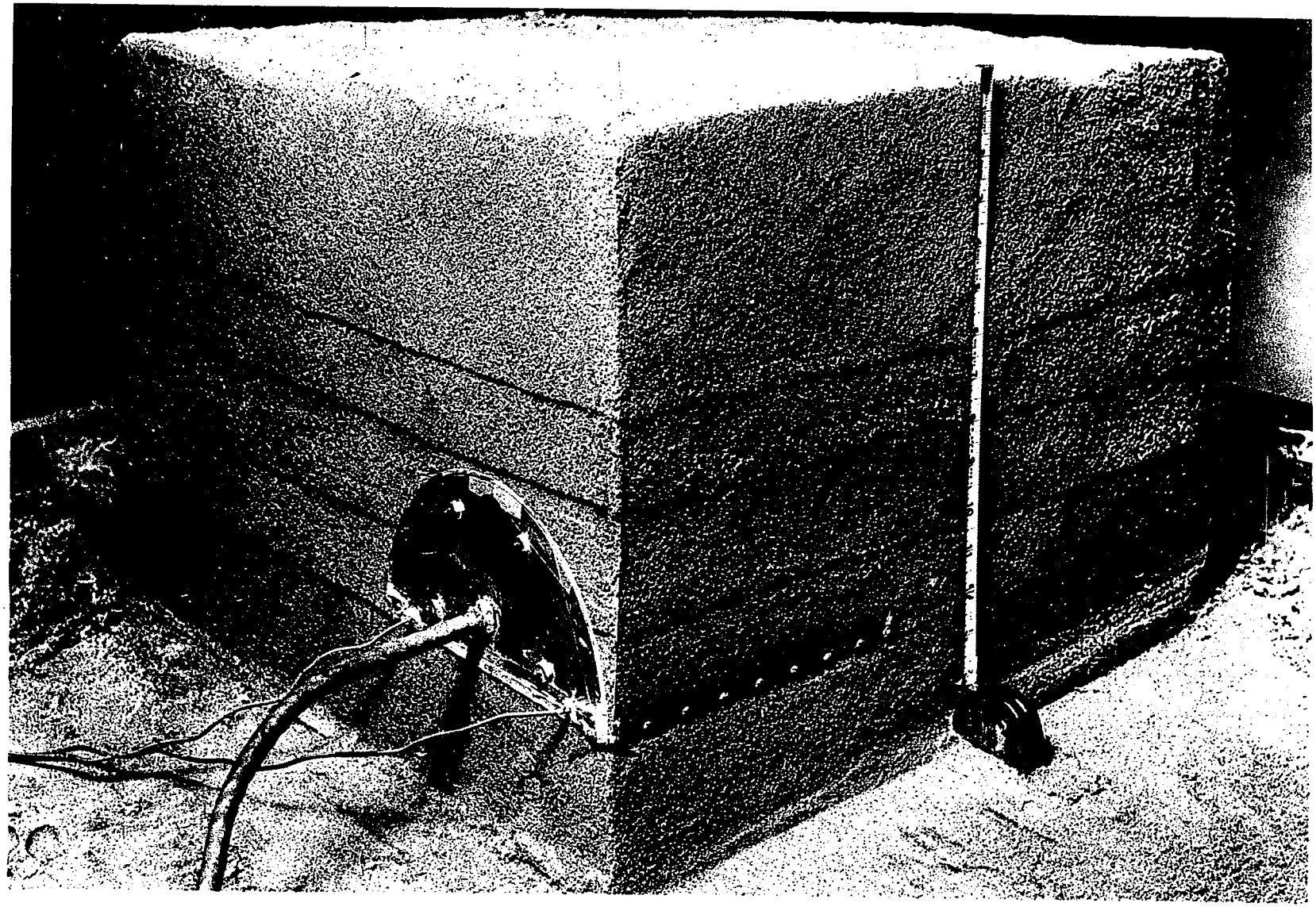

Figure C8. Pilot arch after Series I tests showing grid lines

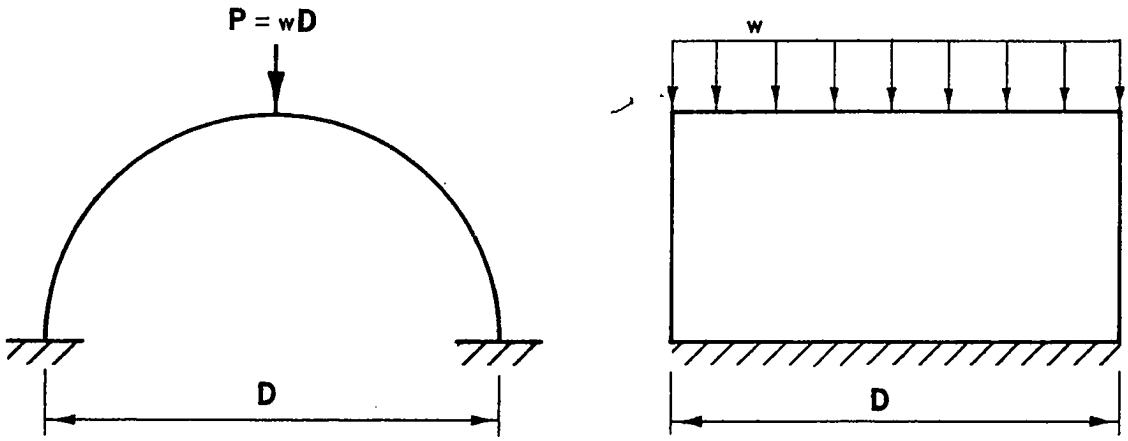

Figure C9. Static bench test loading, Pilot Series II

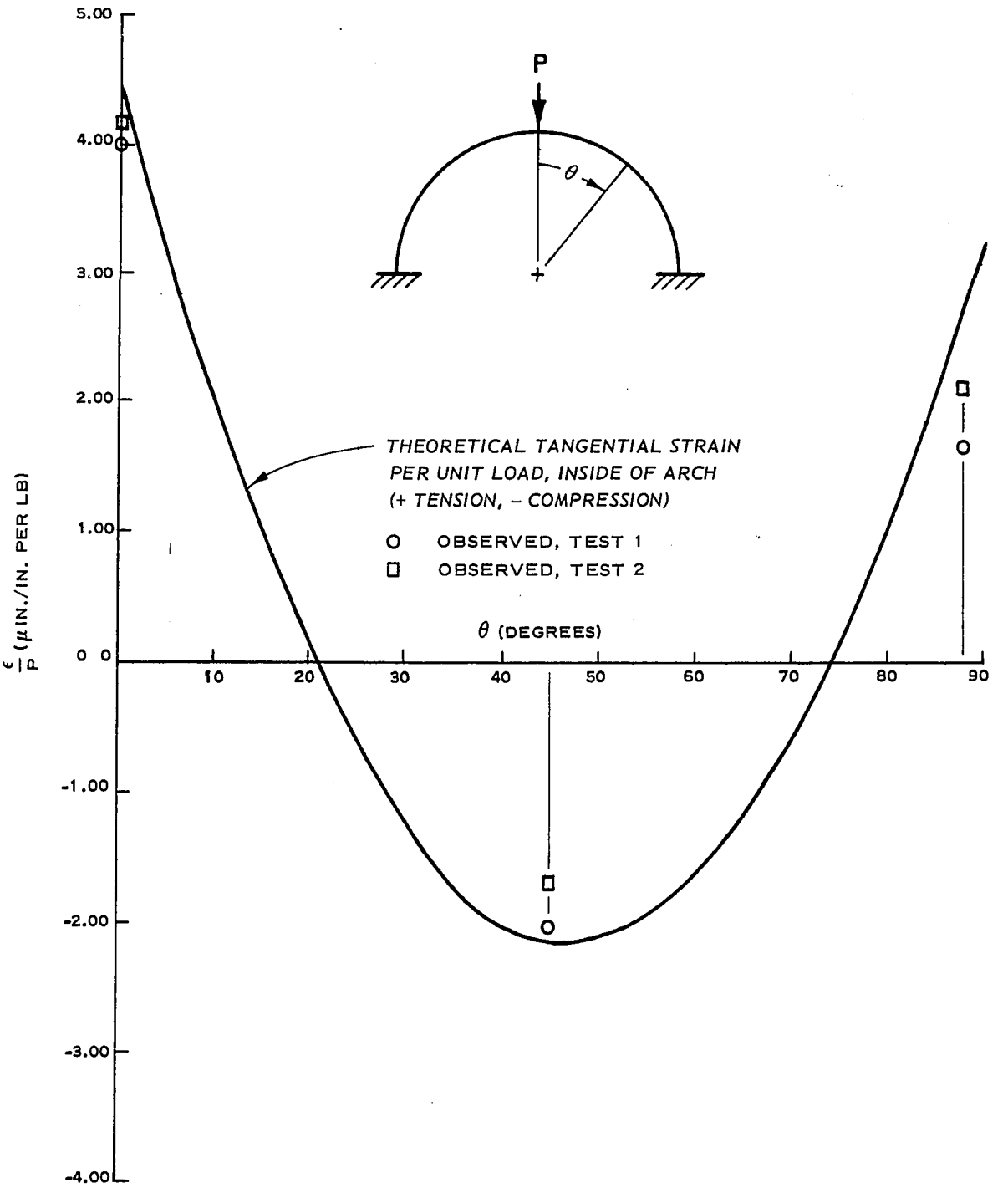

Figure C10. Strain per unit load versus θ, Series II pilot model arch

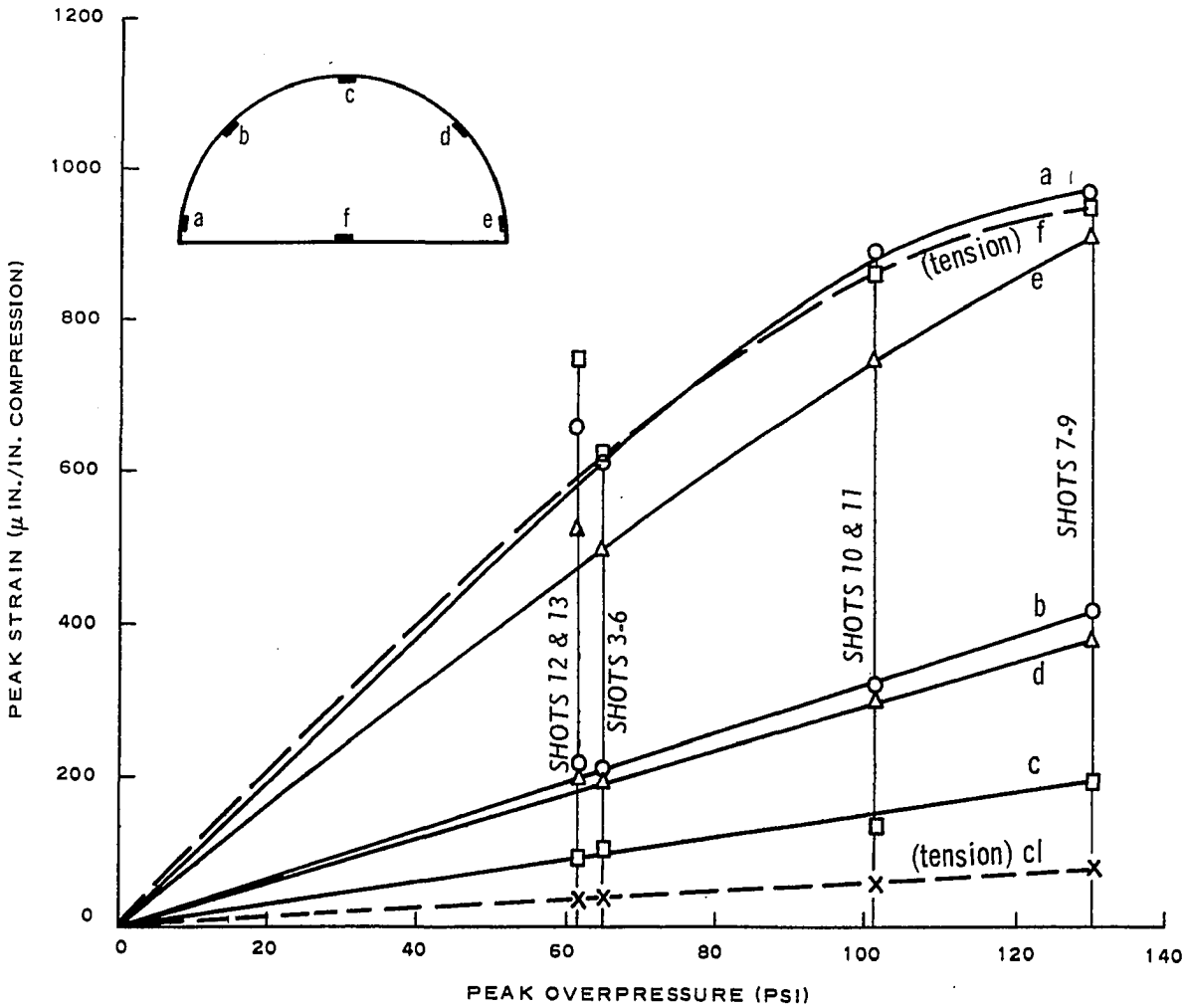

Figure C11. Peak strain versus peak surface overpressure, Pilot Series II

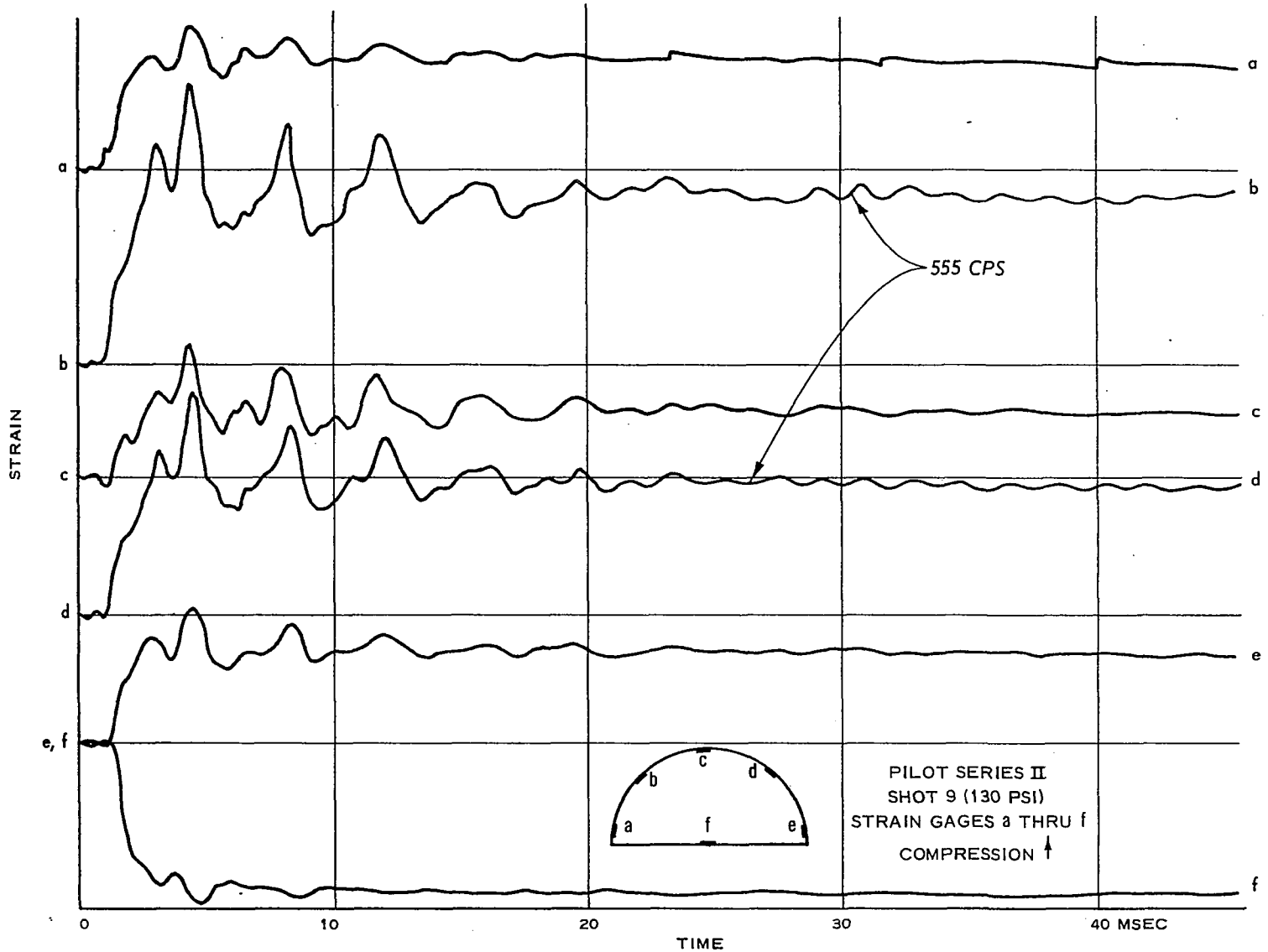

Figure C12. Typical dynamic records, pilot tests

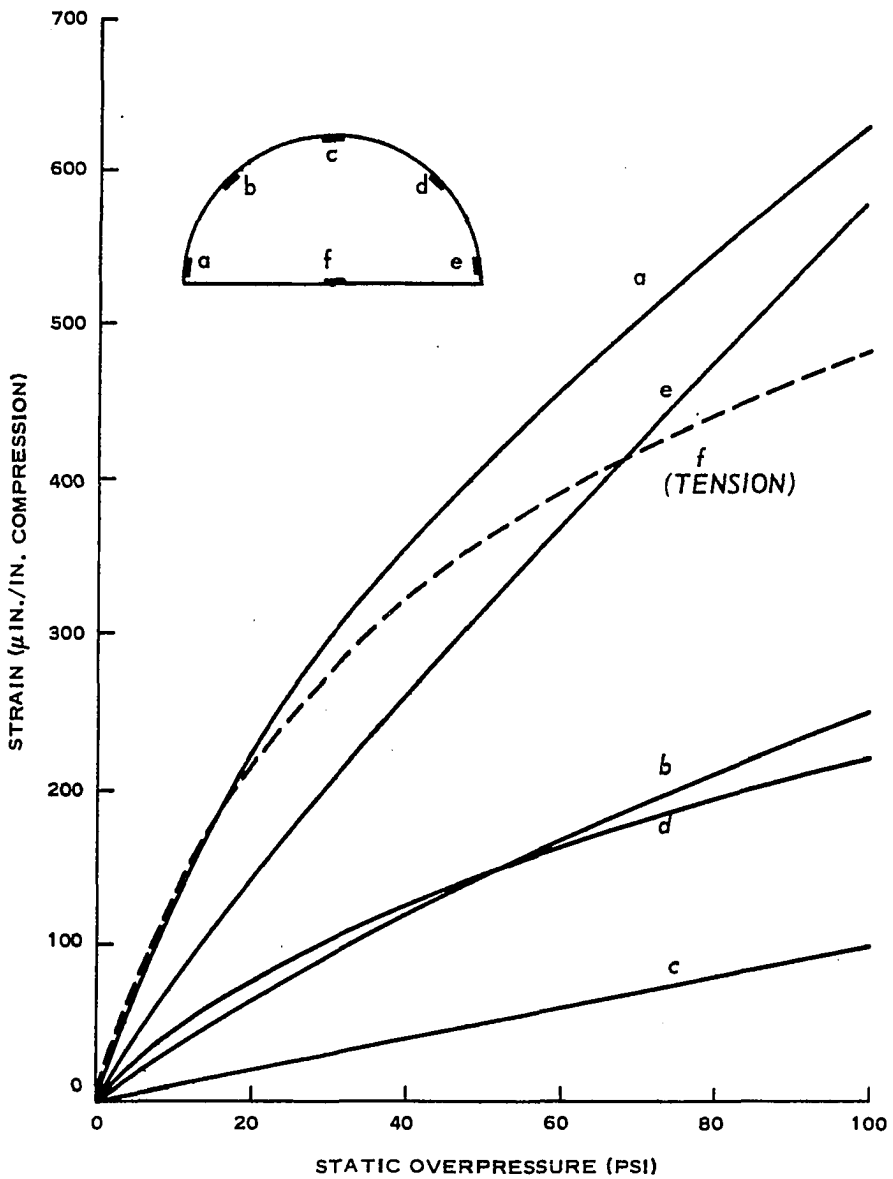

Figure C13. Strain versus static overpressure, Pilot Series II

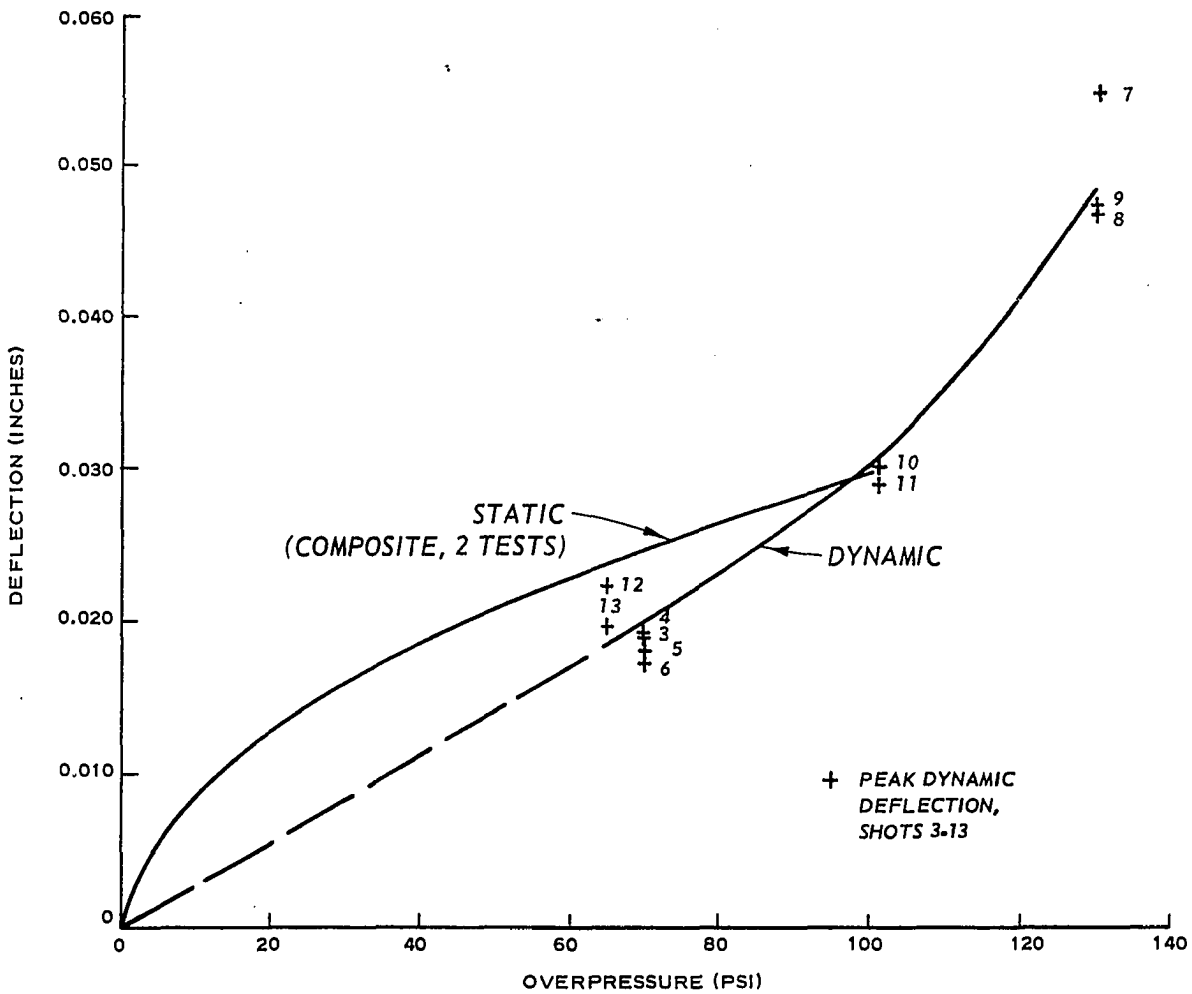

Figure C14. Static and dynamic deflection versus overpressure

APPENDIX D: DERIVATIONS

A. Fixed-End Arch Strains and Deflections

For purposes of providing a theoretical comparison for the values of strain and deflection which were observed in the pilot model and principal model static, bench loading tests, it was necessary to assume and analyze an idealized structure for these conditions. A fixed-end arch was assumed, since the arch roof was the particular segment of interest, and since the floor was 5 times as thick, thus 125 times as stiff, as the roof. The fixed-end arch with a concentrated crown load is shown in Figure D1. In order to calculate strains and deflections, the general expressions for moment and thrust in the arch roof were required. These were determined by analyzing the structure in Figure D1 using the elastic center method (24), resulting in

$$M_\theta = PR\left[\left(\frac{\pi - 2}{\pi^2 - 8}\right) - \left(\frac{4 - \pi}{\pi^2 - 8}\right)\cos\theta - \frac{1}{2}\sin\theta\right] \qquad (D1)$$

and

$$T_\theta = P\left[\left(\frac{4 - \pi}{\pi^2 - 8}\right)\cos\theta + \frac{1}{2}\sin\theta\right] . \qquad (D2)$$

In order to determine the strain inside the arch roof corresponding to these forces, straight beam flexure theory was employed. For $R/t = 40$, negligible error due to arch curvature will be introduced.

$$\sigma = \frac{T}{A} \pm \frac{Mc}{I} . \qquad (D3)$$

In Equation D3, compressive thrust and strains are positive, as are moments causing tension on the inner and compression on the outer surfaces of the

arch roof. Then the strain on the inside of the roof at any point is

$$\epsilon_\theta = \frac{\sigma_\theta}{E} = \frac{T_\theta}{AE} - \frac{M_\theta c}{EI} . \qquad (D4)$$

Equations D1, D2 and D4 were used to determine the curves which appear in Figures 8, 10 and C10.

To approximate theoretically the deflection recorded by the Collins gage during the bench tests, Figure D1 was again used to represent the structural conditions. Then the desired vertical deflection of the crown with respect to the fixed floor is ΔV_c . Noting that this deflection is the same as $\Delta V_b^{\tan c}$, then by moment area theorem,

$$\Delta V_c \equiv \Delta V_b^{\tan c} = \int_c^b \frac{Mx'ds}{EI} \qquad (D5)$$

$$= \int_0^{\frac{\pi}{2}} \frac{M_\theta R\,(1 - \sin\theta)\,Rd\theta}{EI} . \qquad (D6)$$

Substituting Equation D1 into Equation D6, and carrying out the integration result in

$$\Delta V_c = \left(\frac{\pi^3 - 20\pi + 32}{8\pi^2 - 64} \right) \frac{PR^3}{EI} \qquad (D7)$$

$$= 0.01167 \frac{PR^3}{EI} . \qquad (D8)$$

For an aluminum section of length b inches, for $R/t = 40$,

$$\frac{R^3}{EI} = \frac{12\,(R/t)^3}{Eb} = \frac{12\,(40)^3}{(10 \times 10^6)\,b} = \frac{768 \times 10^{-4}}{b} \left(\frac{\text{in.}}{\text{lb}} \right) . \qquad (D9)$$

Combining Equations D8 and D9, for P in pounds and b in inches,

$$\Delta V_c = (896 \times 10^{-6}) \frac{P}{b} \text{ (inches)} . \qquad (D10)$$

Equation D10 was used for comparison with observed deflections in the pilot model and principal model bench tests.

B. Relation Between Natural Period of Vibration and Length Scale

The natural period of vibration of any structural element is known to depend upon its geometry and the elastic modulus and mass density of its material. For a buried structure, additional independent variables are assumed to be the mass density of the soil medium and the geometry of the installation. In order to establish the relation between the natural period of vibration and the length scale for similar systems of different sizes, a dimensional analysis is performed.

The pertinent variables are tabulated below with their basic dimensions:

Symbol	Basic Dimensions	Definition
τ	T	Natural period of vibration
I	L^4	Moment of inertia of structural element
λ	L	Representative structural geometric length
E	FL^{-2}	Elastic modulus of structural material
ρ	$FL^{-4}\ T^2$	Mass density of structural material
λ_s	L	Representative geometric length for boundaries of medium
ρ_s	$FL^{-4}\ T^2$	Mass density of medium

The general relationship for τ is

$$\tau = f(\lambda\ ,\ E\ ,\ I\ ,\ \rho\ ,\ \lambda_s\ ,\ \rho_s)\ . \qquad \text{(D11)}$$

This relationship may be expressed without loss of generality (14) by

$$\tau = C_\alpha \lambda^{c_1} E^{c_2} I^{c_3} \rho^{c_4} \lambda_s^{c_5} \rho_s^{c_6} . \qquad (D12)$$

Substituting for each variable its basic dimensions, Equation D12 becomes

$$T \doteq L^{c_1} (FL^{-2})^{c_2} (L^4)^{c_3} (FL^{-4} T^2)^{c_4} L^{c_5} (FL^{-4} T^2)^{c_6} . \qquad (D13)$$

Writing an auxiliary equation for each of the three basic dimensions F , L and T from Equation D13 yields

F: $0 = c_2 + c_4 + c_6$

L: $0 = c_1 - 2c_2 + 4c_3 - 4c_4 + c_5 - 4c_6$

T: $1 = 2c_4 + 2c_6$.

From these three equations in three unknowns, c_1 , c_2 and c_4 are determined in terms of c_3 , c_5 and c_6 :

$c_1 = 1 - 4c_3 - c_5$

$c_2 = -1/2$

$c_4 = 1/2 - c_6$.

Substituting these values for the exponents in Equation D12,

$$\tau = C_\alpha \lambda^{1-c_5-4c_3} E^{-1/2} I^{c_3} \rho^{1/2-c_6} \lambda_s^{c_5} \rho_s^{c_6} , \qquad (D14)$$

and grouping variables by exponents,

$$\tau = C_\alpha \lambda \sqrt{\frac{\rho}{E}} \left(\frac{I}{\lambda^4} \right)^{c_3} \left(\frac{\lambda_s}{\lambda} \right)^{c_5} \left(\frac{\rho_s}{\rho} \right)^{c_6} . \qquad (D15)$$

Now Equation D15 is valid for any system, regardless of size. Considering two systems, one of which is denoted the model, the ratio of their natural periods is

$$\frac{\tau}{\tau_m} = \frac{C_\alpha \lambda \sqrt{\frac{\rho}{E}} \left(\frac{I}{\lambda^4}\right)^{c_3} \left(\frac{\lambda_s}{\lambda}\right)^{c_5} \left(\frac{\rho_s}{\rho}\right)^{c_6}}{C_\alpha \lambda_m \sqrt{\frac{\rho_m}{E_m}} \left(\frac{I_m}{\lambda_m^4}\right)^{c_3} \left(\frac{\lambda_{sm}}{\lambda_m}\right)^{c_5} \left(\frac{\rho_{sm}}{\rho_m}\right)^{c_6}} . \qquad \text{(D16)}$$

The values of the dimensionless C_α and the exponents are equal in the two systems. If the same structural and soil materials are used in the two systems, and if their geometric dimensions are scaled by the length scale n, then

$$\lambda = n\lambda_m$$

$$\rho = \rho_m$$

$$E = E_m$$

$$I = n^4 I_m$$

$$\lambda_s = n\lambda_{sm}$$

$$\rho_s = \rho_{sm} ,$$

and Equation D16 reduces to

$$\frac{\tau}{\tau_m} = n , \qquad \text{(D17)}$$

that is, the ratio of the natural periods of vibration equals the length scale for systems of the same material and geometric similarity.

C. Calculation of Natural Period of Vibration

The natural period of vibration of the buried arch was calculated by means of the equivalent surcharge loading assumption originated at WES (9). It is assumed that

$$\tau' = \tau_f - K(\tau_f - \tau_c) , \tag{D18}$$

where

τ' = natural period of buried arch without correcting for mass of earth cover

τ_f = natural period in flexural mode of equivalent beam of length one-third the developed length of the arch

τ_c = natural period of vibration of arch in compressive mode

K = horizontal load factor for equivalent surcharge load (Figure D2)

The natural period τ of the buried arch, accounting for the mass of earth cover (9, 16), is then calculated from

$$\tau = \tau' \sqrt{\frac{m'}{m}} . \tag{D19}$$

The period τ_f is calculated for an equivalent beam (9) of length $L = 1/3\pi R$, depth t and width b. This gives

$$\tau_f = \frac{2}{\pi}\sqrt{\frac{mL^4}{EI}} = \frac{2}{\pi}\sqrt{\frac{\rho b t L^4}{E\left(\frac{1}{12}bt^3\right)}} = 2.42\sqrt{\frac{\rho}{E}}\left(\frac{R}{t}\right)R .$$

The parameter $\sqrt{\rho/E}$ is the inverse of the seismic velocity which, for aluminum, is 196,000 in./sec. For $R/t = 40$ and R in inches,

$$\tau_f = (2.42)\left(\frac{1}{196{,}000}\right)(40)\,R = 0.493 \times 10^{-3}\,R \text{ (seconds)} . \tag{D20}$$

The period τ_c is calculated (7) from

$$\tau_c = \frac{2\pi D^2}{C_i}\sqrt{\frac{m}{EI}} \tag{D21}$$

where C_i is a dimensionless constant which depends on the mode of

vibration and condition of end fixity. For a fixed-end arch in the compressive mode (7),

$$C_i = 4\sqrt{\frac{2}{3}\left(\frac{R}{k}\right)^2} \qquad \text{(D22)}$$

where $k = \sqrt{I/bt}$ is the radius of gyration of a section of the arch roof. Then, from Equation D21,

$$\tau_c = \frac{2\pi D^2}{4\sqrt{\frac{2}{3}\left(\frac{R}{k}\right)}}\sqrt{\frac{m}{EI}} = 2\pi\sqrt{1.5}\,R\sqrt{\frac{mk^2}{EI}}$$

$$= 7.62R\sqrt{\frac{\rho bt}{E}\cdot\frac{I/bt}{I}} = 7.62\sqrt{\frac{\rho}{E}}\,R\ .$$

Thus, for R given in inches,

$$\tau_c = \frac{7.62}{196{,}000}R = 0.0390\times10^{-3}\,R\ \text{(seconds)}\ . \qquad \text{(D23)}$$

Substituting Equations D20 and D23 in Equation D18,

$$\tau' = (0.493 - 0.454K)\,R\ \text{(milliseconds)}\ . \qquad \text{(D24)}$$

The natural period is modified for the mass of the earth cover by Equation D19. With a depth of burial of one diameter and assuming the unit weight of the soil to be 110 pcf, from Figure D3,

$$\frac{m'}{m} = \frac{(1.107D)\,(110) + (D/80)\,(175)}{(D/80)\,(175)} = 56.7$$

then from Equation D19,

$$\tau = \sqrt{56.7}\,\tau' = 7.53\tau'$$

and from Equation D24,

$$\tau = (3.71 - 3.41K)\,R\ \text{(milliseconds)}\ . \qquad \text{(D25)}$$

Equation D25 is plotted in Figure 36.

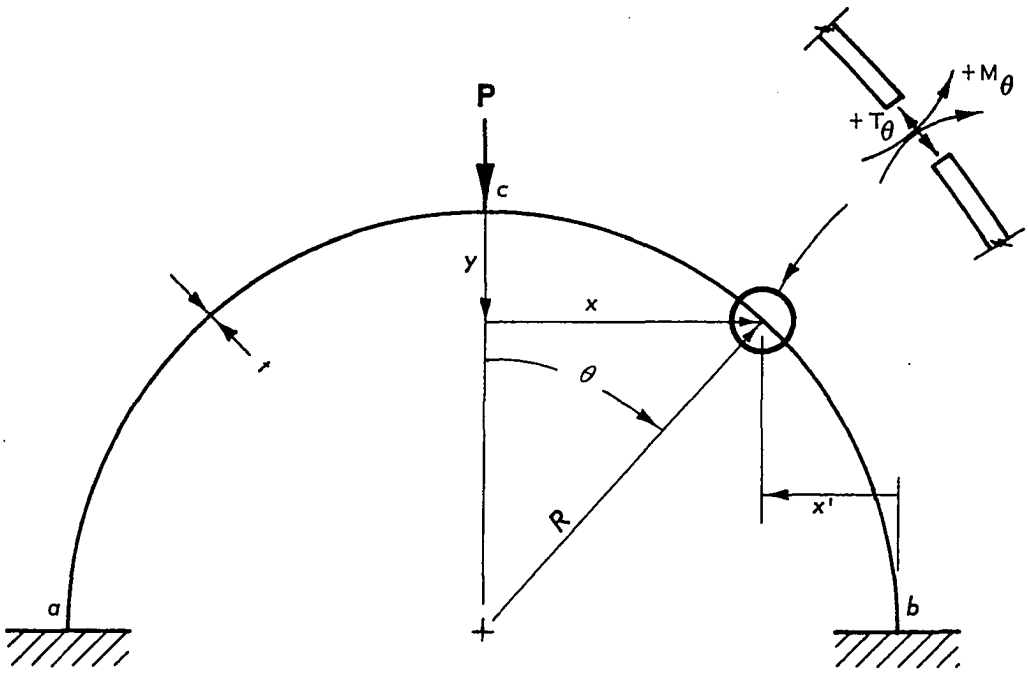

Figure D1. Fixed-end arch with concentrated crown load

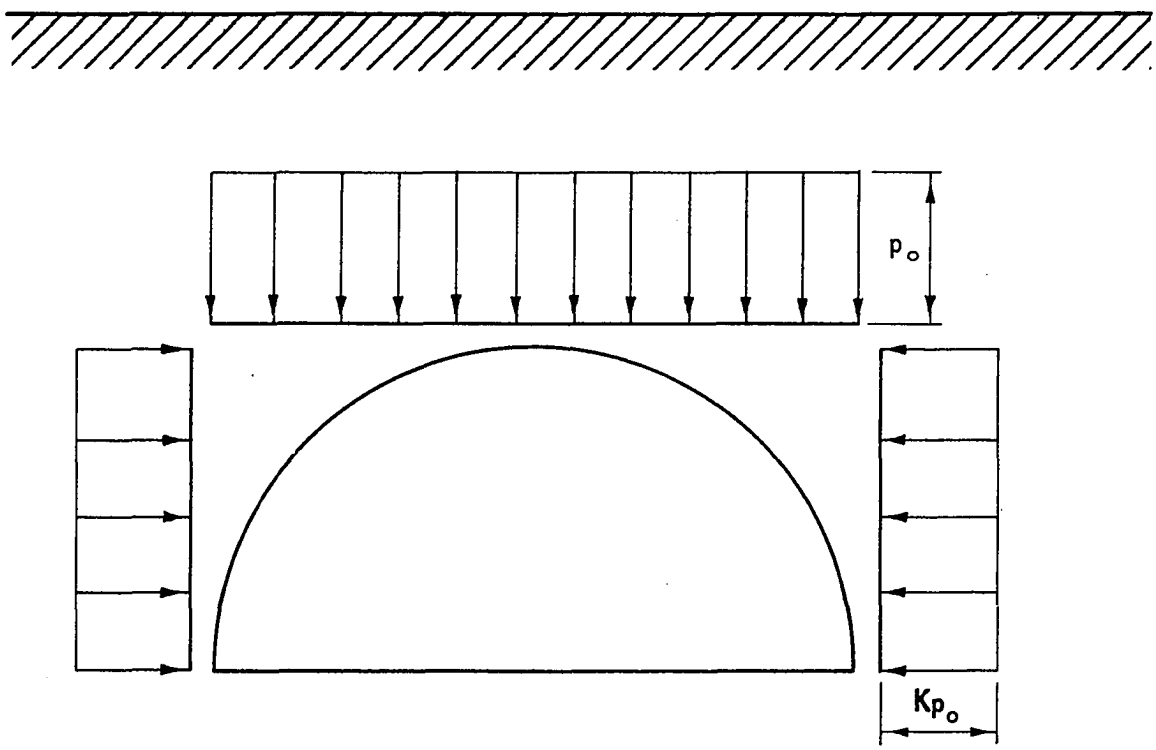

Figure D2. Equivalent surcharge loading

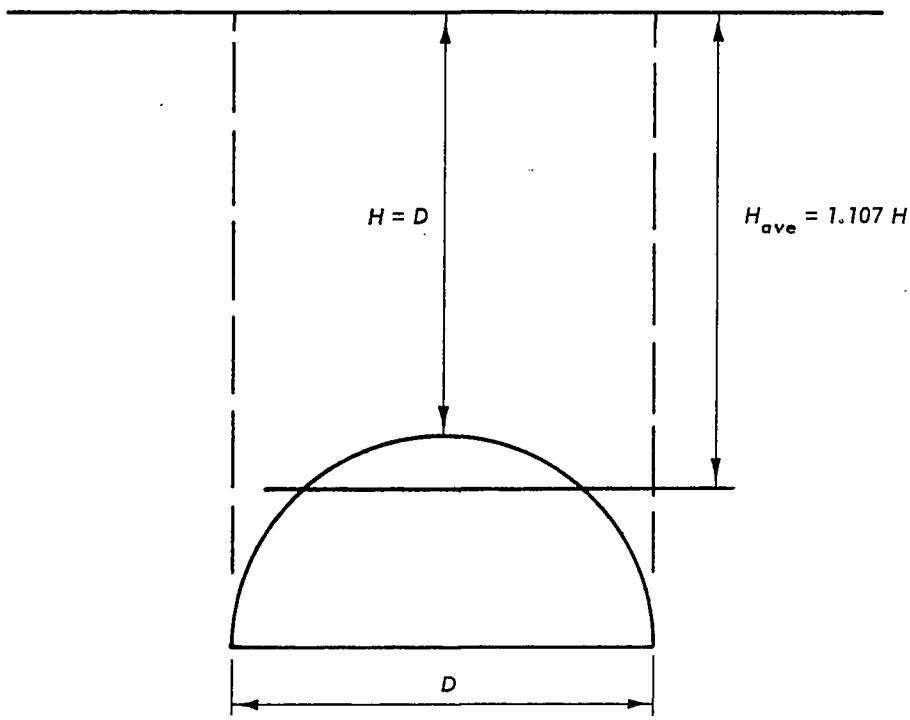

Figure D3. Structure with earth cover